

INTEGRATION OF IN SITU AND LABORATORY VELOCITY MEASUREMENTS:
ANALYSIS AND CALIBRATION FOR ROCK FORMATION CHARACTERIZATION

by

RANDI JO LEE ISHAM

B.S., Kansas State University, 2010

A THESIS

submitted in partial fulfillment of the requirements for the degree

MASTER OF SCIENCE

Department of Geology
College of Arts and Sciences

KANSAS STATE UNIVERSITY
Manhattan, Kansas

2012

Approved by:

Major Professor
Dr. Abdelmoneam Raef

Copyright

RANDI JO LEE ISHAM

2012

Abstract

In this study, laboratory measurements of ultrasonic frequency P- and S-wave velocities were collected and analyzed from two sets of cores. The first set is from a near surface study in southeastern Kansas, and the second set was from the deep subsurface and obtained from a newly drilled well (Wellington KGS 1-32) in Sumner County, KS. Ultrasonic velocities acquired from the second set of cores were then compared with in situ sonic and dipole sonic frequencies of P- and S-waves from well logs. Well log data, core data, and ultrasonic velocity measurements were integrated for Gassmann fluid replacement modeling. The understanding of the velocity and elastic moduli variations at ultrasonic frequencies, along with the comparison of well log velocities can potentially provide improved understanding to establish a beneficial calibration relationship. It could also allow for estimation of shear wave velocities for wells lacking dipole sonic log data. The ability to utilize cost-effective ultrasonic measurements of velocities and elastic moduli in the laboratory, for fluid replacement modeling (Gassmann) in CO₂-sequestration, as well as, enhanced oil recovery (EOR) projects, would be a significant advance. Potential alternative use of ultrasonic velocities for determining the effects of fluid replacement using Gassmann modeling, when log data is lacking, is an ongoing effort. In this study, the fluid replacement modeling is executed based on sonic and dipole sonic P- and S-wave velocities and compared with results from theoretical modeling. The significance of this work lies in the potential of establishing a calibration relationship for the representative lithofacies of the carbon geosequestration target zone of the Wellington KGS 1-32 well in Sumner County, and enabling the use of ultrasonic measurements of body wave velocities and elastic

moduli in Gassmann fluid replacement modeling. This work, when integrated with continuing effort in mapping lithofacies of the Arbuckle and Mississippian groups, would potentially be of great importance to fluid flow simulation efforts and time-lapse seismic monitoring. This study will utilize Gassmann modeling and a range of measurements and data, which include: well logs and ultrasonic laboratory P- and S-wave measurements and core analysis data.

Table of Contents

List of Figures.....	vii
List of Tables	xiii
Acknowledgements	xiv
Chapter 1 - Introduction.....	1
Research Significance	3
Chapter 2 - Core Locality and Stratigraphy.....	5
Arbuckle Group	12
Eminence Dolomite.....	14
Gasconade Dolomite.....	14
Roubidoux Dolomite.....	15
Jefferson City Dolomite and Cotter Dolomite	15
Mississippian Group.....	17
Kinderhookian Stage	18
Chouteau Limestone.....	18
Sedalia Dolomite	18
Gilmore City Limestone.....	18
Osagian Stage.....	18
St. Joe Limestone Member	18
Reeds Spring Formation	19
Burlington – Keokuk Limestone.....	19
Meramecian Series	19
Cowley Facies	19
Warsaw Limestone	19
Salem Limestone	20
St. Louis Limestone	20
Genevieve Limestone	20
Chapter 3 - Methodology.....	25

Ult 100 Ultrasonic System	25
Ultrasonic P-wave and S-wave velocities	32
Automatic Determination of Velocities	32
Manual Determination of Velocities	38
Final Velocities and Elastic Moduli Results	41
Testing Procedures	42
KDOT Cores	42
KGS Cores	43
Gassmann Modeling	44
Chapter 4 - Data and Results	49
Core Information	49
KDOT Core	49
B8S2	49
KGS Cores	63
4-26	63
14-4	71
25-3	78
Amplitude Variations and Attenuation	86
Comparison of In Situ and Laboratory Velocities	89
Gassmann Modeling	95
Chapter 5 - Conclusions	106
References	107
Appendix A - Core Samples	110
Appendix B - Waveform Graphs and Data	124
Appendix C - Gassmann Modeling Data	144

List of Figures

Figure 2.1 Map of Kansas indicating core locations. KDOT cores are highlighted with blue stars. KGS cores are highlighted with a red star. Image modified from http://www.yellowmaps.com/maps/img/_preview/US/blank-county/Kansas_co_lines.jpg	5
Figure 2.2 Surface and subsurface distribution of Pennsylvanian aged rocks in Kansas. (Moore et al., 1951)	7
Figure 2.3 Stratigraphic column including the Auburn Shale and Winzeler Shale Member that are included in the study. Image from Zellner, 1968.....	8
Figure 2.4 Stratigraphic column including the Tacket Formation that is included in the study. Image from Zellner, 1968.	9
Figure 2.5 Stratigraphic column including the Cabaniss Formation that is included in the study. Image from Zellner, 1968.	10
Figure 2.6 Map of North America highlighting the craton. Image from http://www.mnh.si.edu/earth/text/4_1_3_1.html	12
Figure 2.7 Map of Kansas showing major Kansas subsurface structures. Image from KGS.	13
Figure 2.8 Distribution of Arbuckle rocks throughout Kansas. (Merriam, 1963).....	14
Figure 2.9 Stratigraphic column including the Arbuckle Group that is included in the study. Image from Zellner, 1968.....	16
Figure 2.10 Distribution of Mississippian aged rocks throughout Kansas. (Merriam, 1963)	17
Figure 2.11 Stratigraphic column including the Meramecian Stage of the Mississippian Group that is included in the study. Image from Zellner, 1968.....	21
Figure 2.12 Stratigraphic column including the Osagian Stage of the Mississippian Group that is included in the study. Image from Zellner, 1968.	22
Figure 2.13 Stratigraphic column including the Kinderhookian Stage of the Mississippian Group that is included in the study. Image from Zellner, 1968.....	23

Figure 2.14 Generalized Kansas stratigraphic column showing units from the Precambrian to the Paleozoic. (Carr et al., 2005).....	24
Figure 3.1 Physical setup of the lab and the GCTS System. Platens on hydraulic press are showing face-to-face setup with pressure gauge affixed to the top.	26
Figure 3.2 Picture of Ult 100 System showing the platens and aluminum core.	28
Figure 3.3 Sample B8S2 digital P waveform generated from Ult 100 system at 3000 lbf....	29
Figure 3.4 Sample B8S2 digital S waveform generated from Ult 100 system at 3000 lbf....	30
Figure 3.5 Display showing an example of FFT amplitude spectra of a signal showing bandwidth frequency used for measurements.....	31
Figure 3.6 Automatic picking display for the absolute threshold method from the C.A.T.S. Ultrasonic software. Image from GCTS User Manual.	33
Figure 3.7 Automatic picking display for the relative threshold method from the C.A.T.S. Ultrasonic software. Image from GCTS User Manual.	34
Figure 3.8 Automatic picking display for the relative of first peak method from the C.A.T.S. Ultrasonic software. Image from GCTS User Manual.	35
Figure 3.9 Automatic picking display for the first peak time method from the C.A.T.S. Ultrasonic software. Image from GCTS User Manual.	35
Figure 3.10 Automatic picking display for the tangent of first peak method from the C.A.T.S. Ultrasonic software. Image from GCTS User Manual.	36
Figure 3.11 Sample B8S2 using automatic determination picking methods for the P-wave at 500 lbf before dehydration.....	37
Figure 3.12 Sample B8S1 using automatic determination picking methods for the P-wave at 3000 lbf before dehydration.....	38
Figure 3.13 Enlarged picture of stacked P waveforms showing beginning of waveform, ellipse indicates area of first arrival.....	40
Figure 3.14 Sample B8S1 using manual determination for picking first arrival of the P-wave at 3000 lbf before dehydration.....	41
Figure 3.15 Figure 21. Picture of interactive Excel spreadsheet used for Gassmann modeling.....	48
Figure 4.1 KDOT Core B8S2, view parallel to cored axis.....	50
Figure 4.2 KDOT Core B8S2, view perpendicular to cored axis.....	50

Figure 4.3 Thin section image of KDOT Core sample B8S2. Image is at 10X magnification and in plane polarized light.....	51
Figure 4.4 Thin section image of KDOT Core sample B8S2. Image is at 10X magnification and in crossed polarized light.	51
Figure 4.5 Graph of sample B8S2, P waveform from 500 Lbf to 3000 Lbf prior to sample dehydration.....	52
Figure 4.6 Graph of sample B8S2, P waveform stacked from 500 Lbf to 3000 Lbf after sample dehydration.....	53
Figure 4.7 Graph of sample B8S2, S waveform stacked from 500 Lbf to 3000 Lbf prior to sample dehydration.....	54
Figure 4.8 Graph of sample B8S2, S waveform stacked from 500 Lbf to 3000 Lbf after sample dehydration.....	55
Figure 4.9 Graph comparing P-wave velocity (m/s) to increasing lbf for core sample B8S2 before dehydration. Data used to construct graph in Table 4.3.....	57
Figure 4.10 Graph comparing S-wave velocity (m/s) to increasing lbf for core sample B8S2 before dehydration. Data used to construct graph in Table 4.3.....	58
Figure 4.11 Graph comparing P-wave velocity (m/s) and S-wave velocity (m/s) to Lbf for core sample B8S2 before dehydration. Data used to construct graph in Table 4.3.....	59
Figure 4.12 Graph comparing P-wave velocity (m/s) to increasing lbf for core sample B8S2 after dehydration. Data used to construct graph in Table 4.4.	60
Figure 4.13 Graph comparing S-wave velocity (m/s) to increasing lbf for core sample B8S2 after dehydration. Data used to construct graph in Table 4.4.	61
Figure 4.14 Graph comparing P-wave velocity (m/s) and S-wave velocity (m/s) to Lbf for core sample B8S2 after dehydration. Data used to construct graph in Table 4.4.	62
Figure 4.15 KGS Core 4-26, view perpendicular to cored axis.	64
Figure 4.16 KGS Core 4-26, view parallel to cored axis.....	64
Figure 4.17 Thin section image of KGS Core sample 4-26. Image is at 4X magnification and in plane polarized light.....	65
Figure 4.18 Thin section image of KGS Core sample 4-26. Image is at 4X magnification and in crossed polarized light.....	66

Figure 4.19 Graph of sample 4-26, P waveform stacked from 500 Lbf to 6570 Lbf, simulating near in situ conditions.....	67
Figure 4.20 Graph of sample 4-26, S waveform stacked from 500 Lbf to 6570 Lbf, simulating near in situ conditions.....	68
Figure 4.21 Graph comparing P-wave velocity (m/s) to increasing lbf for core sample 4-26. Data used to construct graph in Table 4.6.....	69
Figure 4.22 Graph comparing S-wave velocity (m/s) to increasing lbf for core sample 4-26. Data used to construct graph in Table 4.6.....	70
Figure 4.23 Graph comparing P-wave velocity (m/s) to S-wave velocity (m/s) for core sample 4-26. Data used to construct graph in Table 4.6.....	71
Figure 4.24 KGS Core 14-4, view perpendicular to cored axis.....	72
Figure 4.25 KGS Core 14-4, view parallel to cored axis.....	72
Figure 4.26 Thin section image of KGS Core sample 14-4. Image is at 4X magnification and in plane polarized light.....	73
Figure 4.27 Thin section image of KGS Core sample 14-4. Image is at 4X magnification and in crossed polarized light.....	73
Figure 4.28 Graph of sample 14-4, P waveform stacked from 500 Lbf to 7500 Lbf, simulating near in situ conditions.....	74
Figure 4.29 Graph of sample 14-4, S waveform stacked from 500 Lbf to 7500 Lbf, simulating near in situ conditions.....	75
Figure 4.30 Graph comparing P-wave velocity (m/s) to increasing lbf for core sample 14-4. Data used to construct graph in Table 4.8.....	76
Figure 4.31 Graph comparing S-wave velocity (m/s) to increasing lbf for core sample 14-4. Data used to construct graph in Table 4.8.....	77
Figure 4.32 Graph comparing P-wave velocity (m/s) and S-wave velocity (m/s) to Lbf for core sample 14-4. Data used to construct graph in Table 4.8.....	78
Figure 4.33 KGS Core 25-3, view perpendicular to cored axis.....	79
Figure 4.34 KGS Core 25-3, view parallel to cored axis.....	79
Figure 4.35 Thin section image of KGS Core sample 25-3. Image is at 4X magnification and in plane polarized light.....	80

Figure 4.36 Thin section image of KGS Core sample 25-3. Image is at 4X magnification and in crossed polarized light.....	80
Figure 4.37 Graph of sample 25-3, P waveform stacked from 500 Lbf to 3000 Lbf.....	81
Figure 4.38 Graph of sample 25-3, S waveform stacked from 500 Lbf to 3000 Lbf.....	82
Figure 4.39 Graph comparing P-wave velocity (m/s) to increasing lbf for core sample 25-3. Data used to construct graph in Table 4.10.....	83
Figure 4.40 Graph comparing S-wave velocity (m/s) to increasing lbf for core sample 25-3. Data used to construct graph in Table 4.10.....	84
Figure 4.41 Graph comparing P-wave velocity (m/s) and S-wave velocity (m/s) to Lbf for core sample 25-3. Data used to construct graph in Table 4.10.....	85
Figure 4.42 Attenuation coefficients for the Wellington oil field site.....	87
Figure 4.43 Attenuation coefficients for sample B6S1, before and after dehydration.....	87
Figure 4.44 Attenuation coefficients for sample B6S2, before and after dehydration.....	88
Figure 4.45 Well log interval for sample 4-26 at 3717 ft (indicated by red arrow) showing gamma ray (green curve) and sonic and dipole sonic logs (black curves).....	90
Figure 4.46 Well log interval for sample 14-4 at 4247 ft (indicated by red arrow) showing gamma ray (green curve) and sonic and dipole sonic logs (black curves).....	91
Figure 4.47 Well log interval for sample 25-3 at 4626 ft (indicated by red arrow) showing gamma ray (green curve) and sonic and dipole sonic logs (black curves).....	92
Figure 4.48 Comparison of P-wave velocities at sonic and ultrasonic frequencies obtained from well logs and laboratory measurements (see Tables 4.11 and 4.12).	93
Figure 4.49 Comparison of S-wave velocities at sonic and ultrasonic frequencies obtained from well logs and laboratory measurements (see Tables 4.11 and 4.12).	93
Figure 4.50 Comparison of Poisson's Ratio at sonic and ultrasonic frequencies.....	94
Figure 4.51 Graph of theoretical values of sub-critical CO ₂ in limestone, comparing velocity of P-waves (m/s) to increasing saturation levels CO ₂ . Data used to create graph is found in Appendix C.	97
Figure 4.52 Graph of theoretical values of super-critical CO ₂ in limestone, comparing velocity of P-waves (m/s) to increasing saturation levels CO ₂ . Data used to create graph is found in Appendix C.	98

Figure 4.53 Graph of theoretical values of sub-critical CO₂ in sandstone, comparing velocity of P-waves (m/s) to increasing saturation levels CO₂. Data used to create graph is found in Appendix C. 99

Figure 4.54 Graph of theoretical values of super-critical CO₂ in sandstone, comparing velocity of P-waves (m/s) to increasing saturation levels CO₂. Data used to create graph is found in Appendix C. 100

Figure 4.55 Map showing three different porosity classes for the top of the Mississippian in the Wellington field. Class 1, indicated in dark green, is porosity values greater than 12%. Class 2, indicated in sea foam green, is porosity values from 8 to 12%. Class 3, indicated in yellow, is porosity values less than 8%. The red areas on the map represent ambiguous areas. Well of interest is Wellington KGS 1-32. Image from Ohl, D. R., and Raef, A. B. (under review, 2012). 101

Figure 4.56 Map showing three different porosity classes for the top of the Arbuckle in the Wellington field. Class 1, indicated in dark green, is porosity values greater than 12%. Class 2, indicated in sea foam green, is porosity values from 8 to 12%. Class 3, indicated in yellow, is porosity values less than 8%. The red areas on the map represent ambiguous areas. Well of interest is Wellington KGS 1-32. Image from Ohl, D. R., and Raef, A. B. (under review, 2012). 102

Figure 4.57 Graph showing the change in velocities of P-waves in relation to CO₂ saturations for sample 4-26. Classes correlated with Figure 4.55. Data used to create graph is found in Appendix C. 103

Figure 4.58 Graph showing the change in velocities of P-waves in relation to CO₂ saturations for sample 14-4. Classes correlated with Figure 4.56. Data used to create graph is found in Appendix C. 104

List of Tables

Table 4.1 Physical properties of sample B8S2 prior to dehydration.....	50
Table 4.2 Physical properties of sample B8S2 after dehydration.....	50
Table 4.3 Velocity of P- and S-waves and elastic moduli of sample B8S2 before dehydration.	56
Table 4.4 Velocity of P- and S-waves and elastic moduli of sample B8S2 after dehydration.	56
Table 4.5 Physical properties of sample 4-26.....	64
Table 4.6 Velocity of P- and S-waves and elastic moduli of sample 4-26.	69
Table 4.7 Physical properties of sample 14-4.....	72
Table 4.8 Velocity of P- and S-waves and elastic moduli of sample 14-4.	76
Table 4.9 Physical properties of sample 25-3.....	79
Table 4.10 Velocity of P- and S-waves and elastic moduli of sample 25-3.....	83
Table 4.11 P- and S-wave velocities from well logs at sonic frequencies.....	89
Table 4.12 P- and S-wave velocities from laboratory data at ultrasonic frequencies.....	89

Acknowledgements

I would like to give a special thanks to Dr. Abdelmoneam Raef, my supervising advisor, for taking me on as a graduate student and also his integral role in my research. Without his help, this study could not have been completed. My committee members, Dr. Matt Totten and Dr. Keith Miller have also had a great influence on the outcome of my work. I am very grateful for their time and effort put into helping with the progression of this research. I would like to thank Kansas Geological Survey and Department of Energy for granting access to cores from the Wellington project, and Keith Miller and the Kansas Department of Transportation for access to the near surface cores. Also, I want to especially thank Derek Ohl, Robinson Barker, Zac Hasten, Charlotte Philip and all of the graduate students for all they have done over the years. It was through the successful collaboration of all these efforts, that my research was possible. Last but not least, I am forever appreciative of my family and friends for all of their encouragement and support.

Chapter 1 - Introduction

There has been significant effort placed on enhancement of reservoir characterization and optimization in geosciences. Despite the substantial advancements and gained understanding in this field, there are still a number of uncertainties. Any progress in the ability to more adequately characterize and better understand a hydrocarbon reservoir can mean substantial growth in hydrocarbon recovery or better flow-simulation modeling in CO₂ geosequestration endeavors. To this end, improved reservoir characterization has been the main objective of many studies. These studies have taken a number of approaches and focus on how to go about characterization. In one study, rock physics models were created to validate well log information for formation evaluation (Besheli, 1998). Reduction of the greenhouse gas CO₂ and enhanced oil recovery have been some of the primary driving forces in these efforts. Recent studies have put forth ample resources and effort into carbon geosequestration research (Lackner, 2003). This process involves taking CO₂ from large point-emission sources and injecting it into the subsurface for long-term storage. The first commercial trial of carbon sequestration was in Sleipner oil and gas field in the North Sea (Herzog, 2001). Reservoirs, especially saline aquifers (long-term geological storage) and depleted oil fields (enhanced oil recovery), are prime locations for this potential injection. The addition of CO₂ can alter the reservoir characteristics in a number of ways, such as fluid properties, porosity, etc. Some of the subsurface fluid replacement effects can be approximated by the use of Gassmann fluid replacement modeling. This method has been effective when working within the necessary

assumptions, as further discussed in Chapter 3, associated with the modeling technique (Smith, 2003). However, there remain a number of uncertainties and limitations when utilizing velocity analysis for reservoir characterization.

There are a number of uncertainties and unresolved issues with rock physics, but with the advances over the last five decades, it has become a key part of most studies focused on reservoir characterization (Wang, 2001; Sayers and Chopra, 2009). “Rock physics addresses the relationships between measurements of elastic properties made from the surface, well and lab equipment, and intrinsic properties of the rocks, such as mineralogy, porosity and pore shapes; pore fluids; pore pressures, permeability; viscosity, stresses and overall architecture such as laminations and fractures” (Sayers and Chopra, 2009). One of the primary outcomes of rock physics is to increase comprehension of the reservoir’s physical properties. Rock properties, fluid properties and environments are the primary influences on seismic properties. Understanding pressures associated with the reservoir is important for drilling purposes and also for seismic applications including lithology discrimination, 4-D and amplitude variation offset (AVO) (Wang, 2001; King 2009; Besheli 1998).

Two distinct pressures exist in a reservoir: confining or overburden pressure (P_o) that is generated from the overlying rock strata, and pore or fluid pressure (P_p) that is exerted by the fluid mass. P_d is the net overburden or differential pressure control on seismic properties and can be calculated from the difference between the confining pressure and pore pressure. Rocks with more compliant pore space will exhibit a greater effect from the influence of fluids than those with stiff pores (Wang, 2001). For

enhancement of seismic interpretation, a rock physics model can be made in order to establish a calibration relationship between core and log measurements (Besheli, 1998).

Using similar methods to this work, other research has been conducted focusing on the ultrasonic domain. When testing cores at increasing pressures, most cores tend to have an initial rapid increase in velocity followed by a more gradual increase. This pattern is most likely due to the closure of compliant microcracks within the rock (Song, 1965).

Gassmann's fluid replacement modeling can be used to predict velocities after fluid substitution has taken place. This can be done by using velocities saturated with the initial pore fluid (or gas), extracting the bulk and shear modulus, then using Gassmann's relations to recreate velocities with the bulk modulus of the rock with pore space occupied by the substituting fluid (Mavko et al., 2009). Fluid replacement modeling can be very beneficial in reservoir monitoring 4D time-lapse seismic, carbon geosequestration and enhanced oil recovery.

Research Significance

Integration of geophysical data at seismic and laboratory ultrasonic frequencies can pose some noteworthy concerns (Grochau et al., 2009). This study focuses on the understanding of laboratory measurements on cores at ultrasonic frequencies and their integration with sonic and dipole sonic frequencies from well logs to better understand their relationships. The laboratory measurements will generate an analog waveform that is converted to a digital display. Velocities of P- and S-waves at ultrasonic frequencies can be derived from first arrival of these waveforms. From these velocities, bulk modulus, Young's

Modulus, Shear (Rigidity) Modulus and Poisson's Ratio can be calculated. The properties are derived from cores using the GCTS ULT-100 system.

There are many ambiguities and unknowns still present in the aspect of geophysics and rock physics. This study concentrates on the effect of frequency dependency on variations in velocity measurements, amplitude and velocity variations with increasing effective stress, and fluid replacement modeling. Translating the understanding of geophysical data collected at seismic frequency into higher frequencies is a current drawback (Grochau et al., 2009). Ultrasonic and sonic frequencies have not been properly understood in this domain.

Fluid replacement modeling conducted in this study could benefit future seismic time-lapse monitoring and verification programs for CO₂ sequestration. Currently, there are a number of limitations associated with Gassmann fluid replacement modeling, so any broadening of the application could have a significant impact on seismic time-lapse monitoring.

Chapter 2 - Core Locality and Stratigraphy

This study includes the analysis of two sets of cores. The first set of cores is from the near surface, and was collected as a part of previous research from various counties in southeastern Kansas (Linn, Greenwood, Elk, and Crawford County). The other set is from the Mississippian System and Arbuckle Group reservoir, and collected from the KGS site in Sumner County, Kansas from the Wellington oil field. Cores used in this study were taken from the Wellington KGS 1-32 well. This well has a total depth of 5240 feet, and the cores were taken from 3717.9, 4247, and 4626.9 feet. The county locations are shown in Figure 2.1.

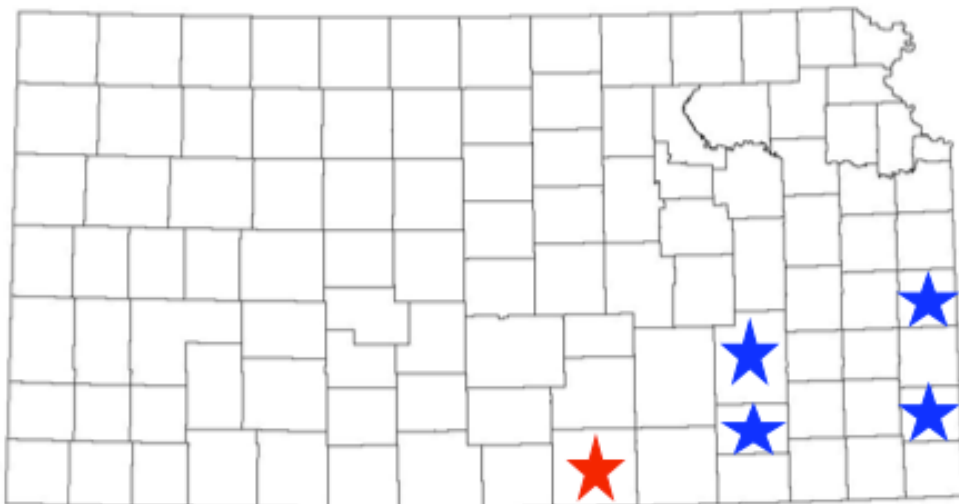


Figure 2.1 Map of Kansas indicating core locations. KDOT cores are highlighted with blue stars. KGS cores are highlighted with a red star. Image modified from http://www.yellowmaps.com/maps/img/_preview/US/blank-county/Kansas_co_lines.jpg

The first set of cores was acquired from a previous study conducted by Kansas Department of Transportation in collaboration with Dr. Keith Miller from Kansas State University. These cores are Pennsylvanian aged near surface rocks from southeastern Kansas. They are primarily comprised of fine-grained siliciclastics. The second set of cores, provided by the Department of Energy and Kansas Geological Survey, are from the Arbuckle Group and Mississippian System in Sumner County, Kansas.

In southeastern Kansas, rocks of Pennsylvanian age outcrop, as seen in Figure 2.2, and are readily available for near surface studies. The cores included in this research range from Middle to Upper Pennsylvanian Series. Cabaniss Formation of the Cherokee Group, Tackett Formation, Auburn Shale, and Winzeler Shale Member are all represented in the cores from KDOT, as seen in Figures 2.3, 2.4, and 2.5. However, it is noted that in the subsurface, the Cherokee Group can typically not be separated into distinct formations. Stratigraphic data acquired from the KGS.

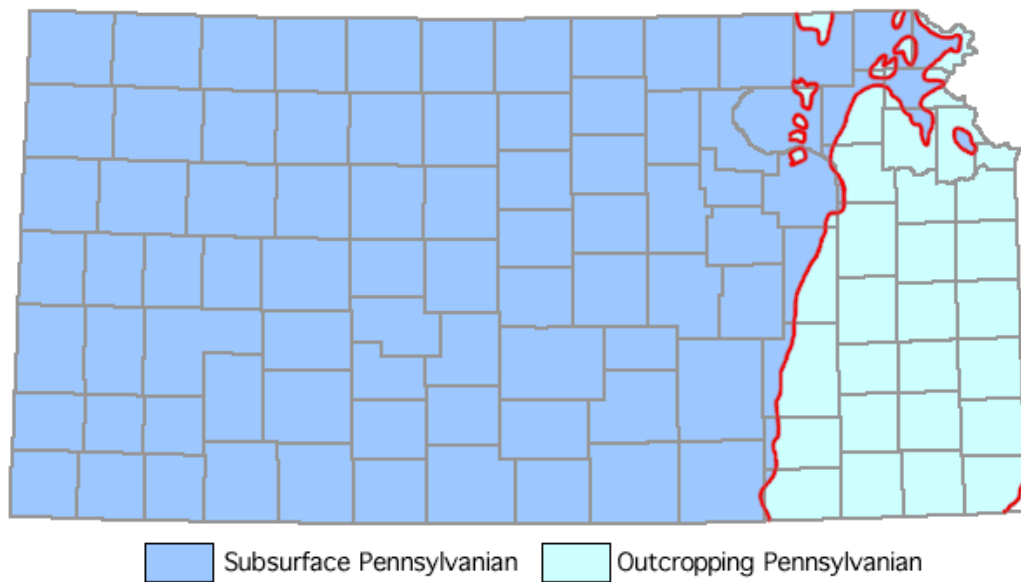


Figure 2.2 Surface and subsurface distribution of Pennsylvanian aged rocks in Kansas. (Moore et al., 1951)

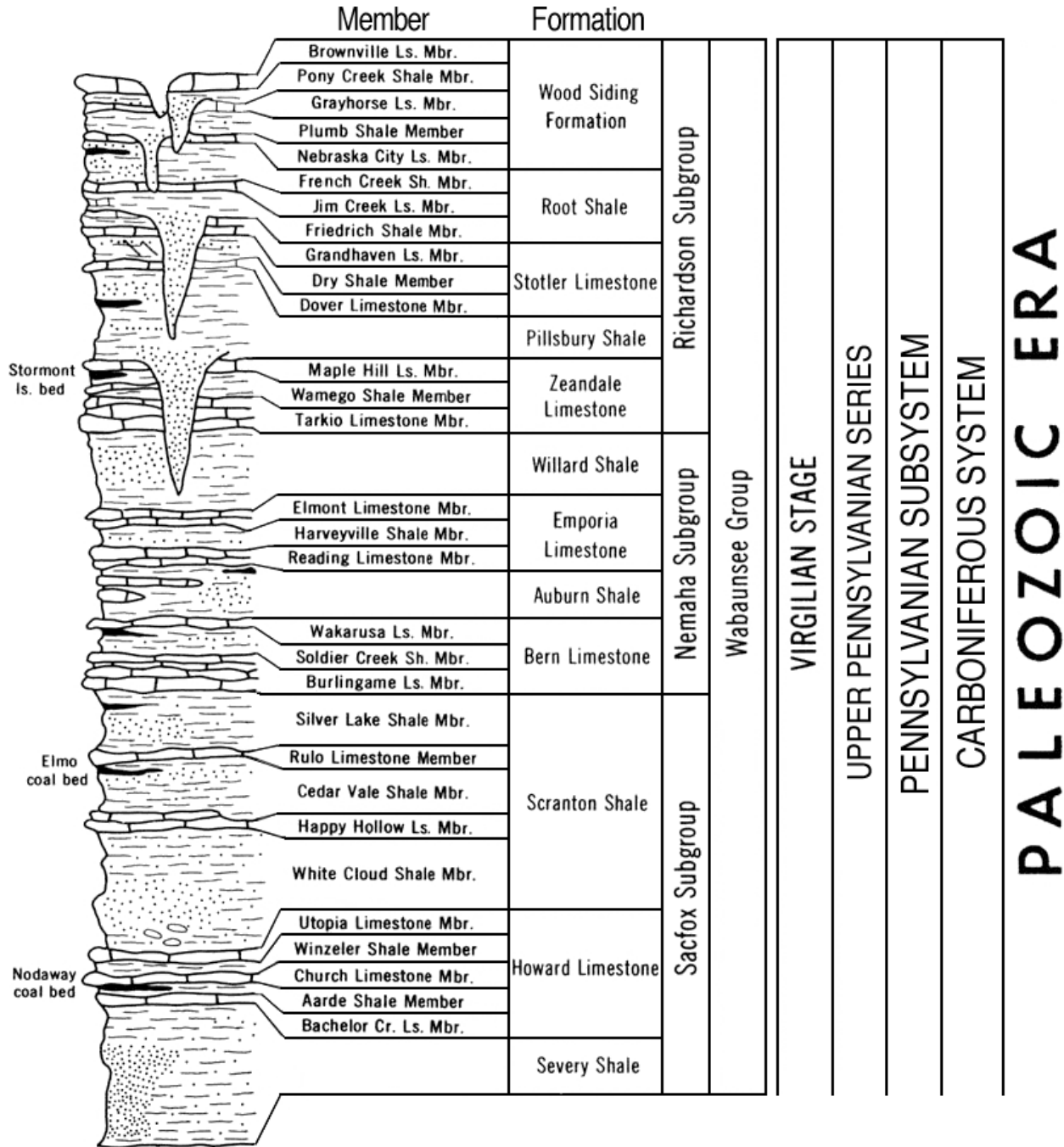


Figure 2.3 Stratigraphic column including the Auburn Shale and Winzeler Shale Member that are included in the study. Image from Zellner, 1968.

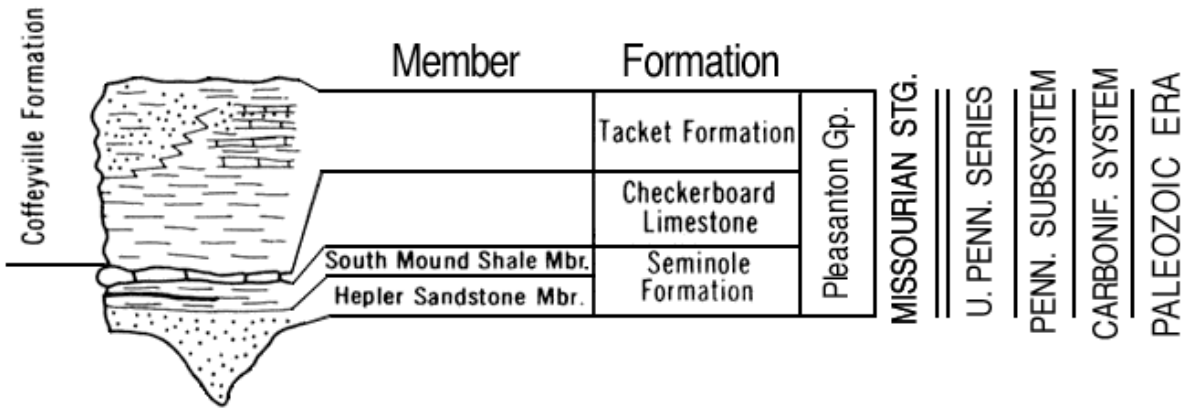


Figure 2.4 Stratigraphic column including the Tacket Formation that is included in the study. Image from Zellner, 1968.

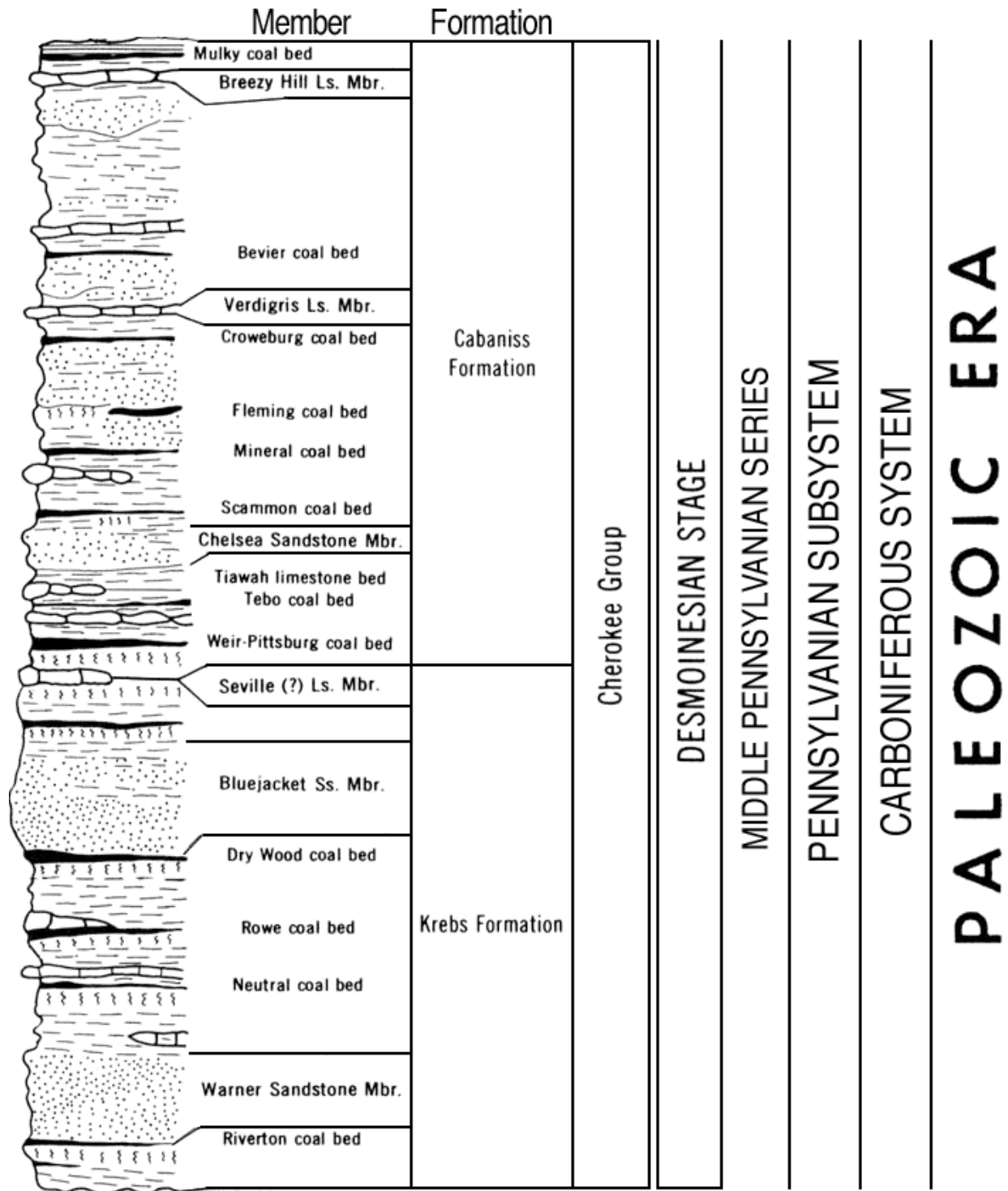


Figure 2.5 Stratigraphic column including the Cabaniss Formation that is included in the study. Image from Zellner, 1968.

The second set of cores was collected from the Mississippian, and the Arbuckle Group formed during the Cambrian to Ordovician. Large packages of carbonates were deposited along the “Great American Bank” during formation of the Arbuckle, which stretched along the edges of the present North American Craton as seen in Figure 2.6 (Wilson et al., 1991). According to Franseen et al. (2004), this area consists of hundreds of meters of largely dolomitized intertidal to shallow subtidal cyclic carbonate rocks overlain by a regional unconformity. The brines were Mg – rich and have been theoretically linked to dolomitization process of the Arbuckle Group on the southern arch.

Due to the sub aerial exposure of the Arbuckle, there was a significant amount of weathering and secondary solution in the upper most areas. This in return generated enhanced porosity and permeability. With the enrichment of pore space and connectivity, this created ideal conditions for a petroleum reservoir (Walters, 1958; Merriam, 1963; Adler, 1971). The uppermost portion of the Arbuckle Group is seen as an oil column that is located directed above a large aquifer (Franseen et al., 2004).



Figure 2.6 Map of North America highlighting the craton. Image from http://www.mnh.si.edu/earth/text/4_1_3_1.html

Arbuckle Group

The Arbuckle Group is found in most areas in the subsurface of Kansas. This excludes areas in the northeastern portion of the state and also in some parts of the Central Kansas Uplift located in Figure 2.7. Extension of the Arbuckle Group across Kansas is seen in Figure 2.7. The Arbuckle is late Cambrian and early Ordovician in age and is comprised of five distinguishable divisions in the southeastern area of Kansas. These divisions include the Eminence, Gasconade, Roubidoux, Cotter and the Jefferson City Dolomites, as seen in Figure 2.9. Looking at the entirety of the Arbuckle Group, it is mainly composed of dolomites. These are all generally dense and crystalline, containing a significant amount of chert in the uppermost part of the group (Merriam, 1963). In the region of focus,

southeastern Kansas, this group ranges from approximately 1000 – 1200 feet in thickness and thins to around 500 feet towards the north (Franseen et al., 2004).

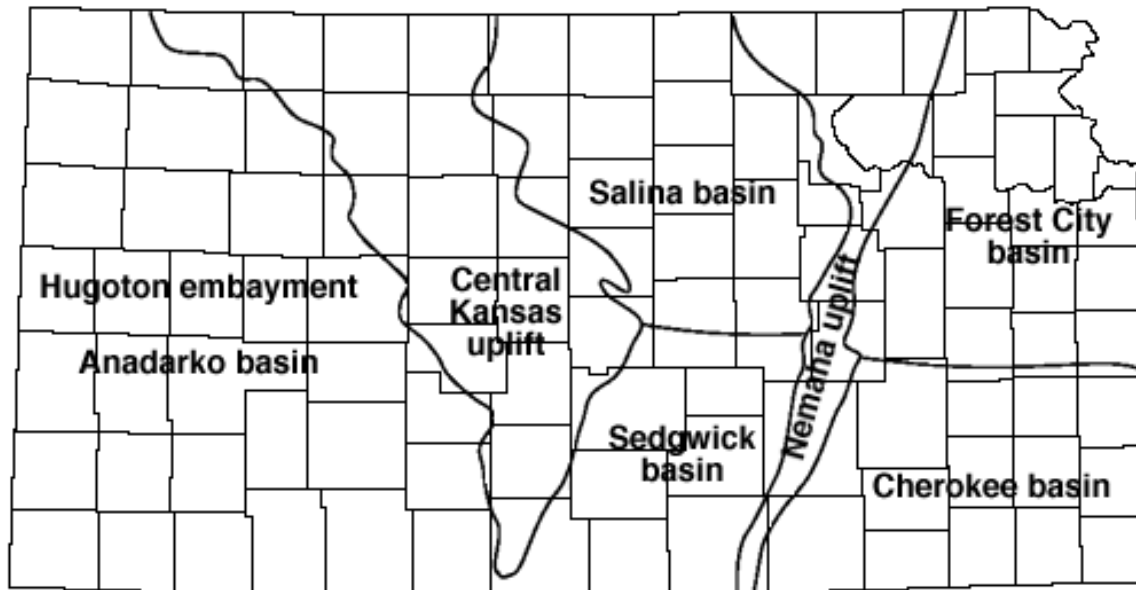


Figure 2.7 Map of Kansas showing major Kansas subsurface structures. Image from KGS.

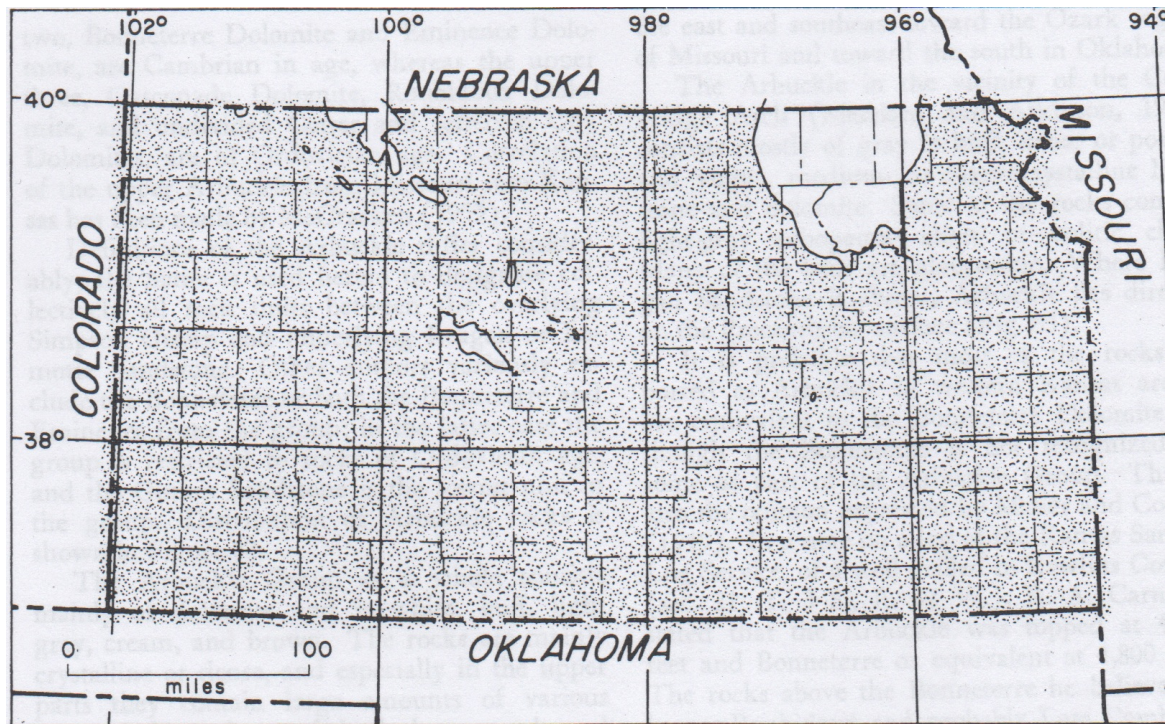


Figure 2.8 Distribution of Arbuckle rocks throughout Kansas. (Merriam, 1963)

Eminence Dolomite

The Eminence Dolomite is late Cambrian in age and the unit ranges from 0 to 150 feet in thickness. This dolomite contains a significant amount of chert that includes cavities that have been lined by finely crystalline quartz. There is an angular unconformity that separates the Eminence Dolomite and the underlying Bonneterre Dolomite.

Gasconade Dolomite

The Gasconade Dolomite is early Ordovician in age and the unit ranges from 0 to 200 feet in thickness. The upper portion of the unit contains chert that is darker in color and denser than the other areas. This chert is dark bluish-gray and lightens in color further down in the unit stratigraphically.

Roubidoux Dolomite

This unit ranges from 150 to 200 feet in thickness and is early Ordovician in age. Throughout Kansas, the Roubidoux Dolomite varies from a sandy dolomite to fine-grained sandstone. Folding and erosion of the rocks in the area preceded the deposition of this unit.

Jefferson City Dolomite and Cotter Dolomite

These two dolomites consist of coarsely granular cherty dolomite and are grouped together as one unit. They range in thickness from 0 to 650 feet. The upper part of the sequence becomes white and decreases in abundance toward the base. At the base of the unit, white chert becomes more plentiful.

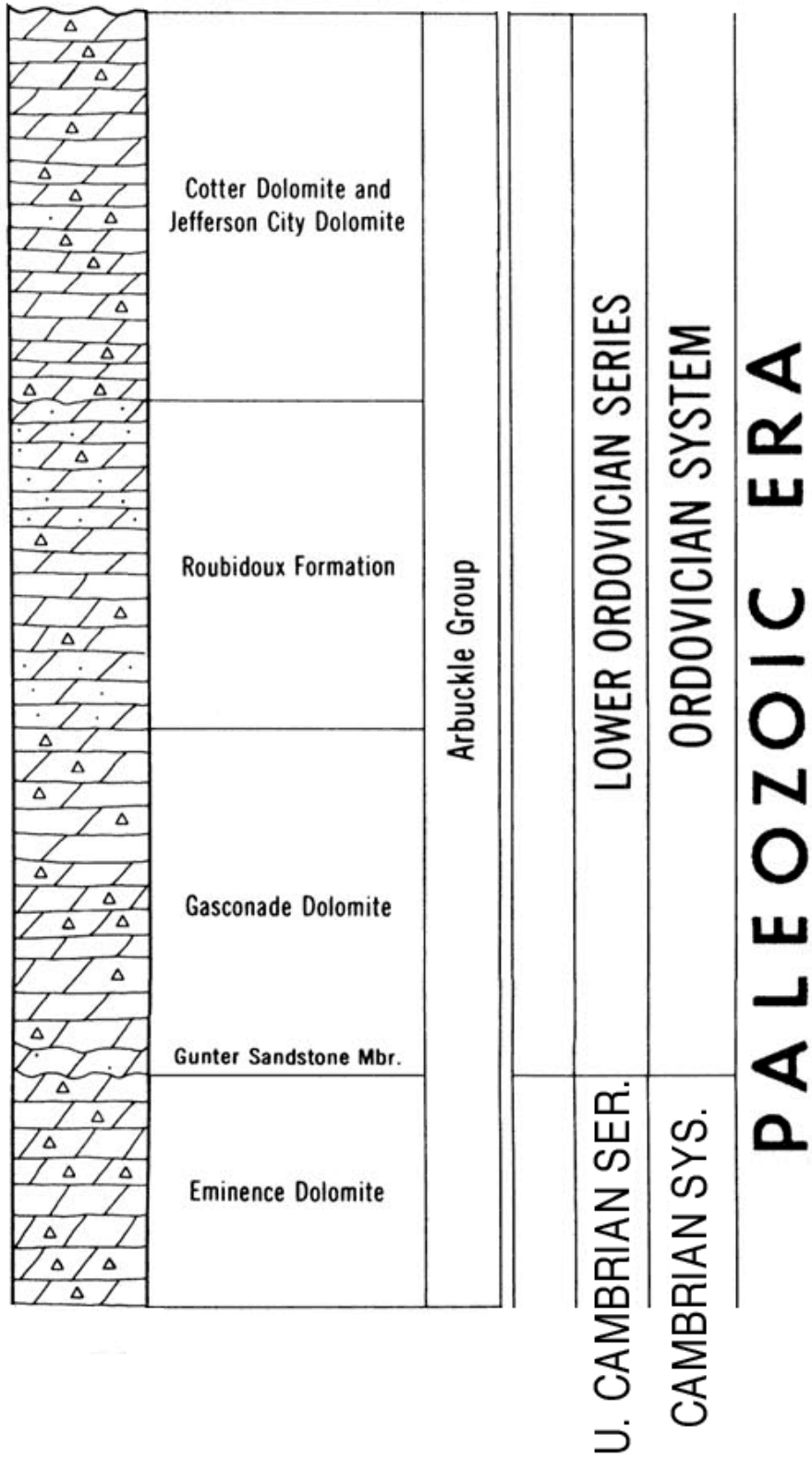


Figure 2.9 Stratigraphic column including the Arbuckle Group that is included in the study. Image from Zellner, 1968.

Mississippian Group

Mississippian aged rocks in southeastern Kansas include the Kinderhookian, Osagian, Meramecian, and Chesteran Series. The Kinderhookian is comprised of the Chouteau Limestone, Sedalia Dolomite and the Gilmore City Limestone, as seen in Figure 2.13. This stage thickens northward towards a basin in Iowa. There is an angular unconformity that separates the Kinderhookian from the overlying Osagian series. The Osagian Series contains the St. Joe Limestone, Reeds Spring Formation, and the Burlington-Keokuk Limestone, as seen in Figure 2.12. The Cowley Facies, Warsaw, Salem, St. Louis and the Genevieve Limestone are all included in the Meramecian Series, as seen in Figure 2.11. The distribution of these rocks throughout Kansas is shown in Figure 2.10.

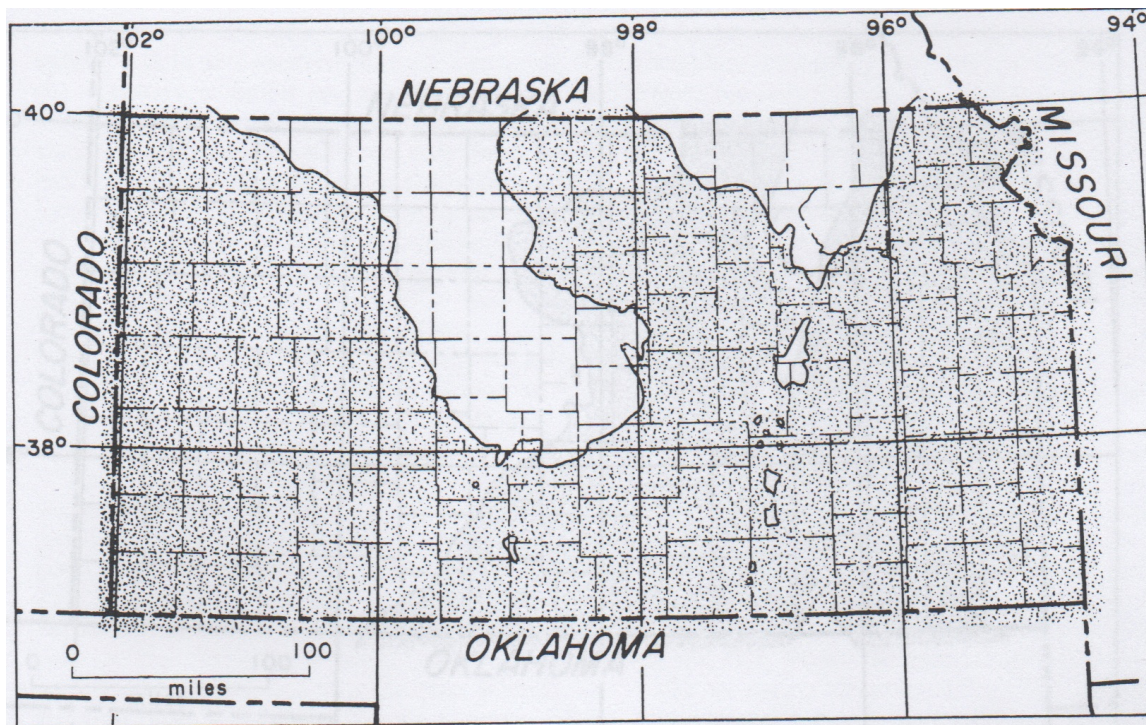


Figure 2.10 Distribution of Mississippian aged rocks throughout Kansas. (Merriam, 1963)

Kinderhookian Stage

Chouteau Limestone

Is a greenish-gray limestone, and is referred to as the Compton Limestone in southeastern Kansas. However, the unit in its entirety is only present east of the Nemaha Anticline and ranges in thickness from 0 – 45 feet.

Sedalia Dolomite

The upper portion of this unit contains minor amounts of chert and is a buff to gray dolomite. The lower section of the Sedalia Dolomite contains ash gray chert that has distinguishable 'stipple' markings. As a whole, the section thins towards southeast Kansas and ranges in thickness from 0 – 30 feet.

Gilmore City Limestone

The Gilmore City Limestone has zones that contain oolites, but most of the unit is a chalky limestone. There are also granules of broken calcareous fossils throughout the unit. This limestone ranges from 0 – 150 in thickness.

Osagian Stage

St. Joe Limestone Member

This limestone is semi-granular and white in color. Also, chert is absent in this member, despite being in a stratigraphic area that typically contains significant amounts of chert. However, there are a noteworthy amount of crinoids present. The bed is approximately 45 feet thick in the southeastern Kansas, study area.

Reeds Spring Formation

The Reeds Spring Formation reaches a maximum thickness around 150 feet. In southwest Kansas, the unit is abundant in dark-gray to brown and semi opaque chert. Siliceous sponge spicules are common throughout the formation.

Burlington – Keokuk Limestone

In southeast Kansas the Burlington unit is absent. However, the Keokuk is present and is a siliceous dolomite that contains white tripolitic chert. The chert content is generally around 50% in both weight and volume. The thickness of the unit ranges from 100 to 350 feet.

Meramecian Series

Cowley Facies

This facies is only present just north of the Oklahoma and Kansas border. Silty, siliceous dolomite and limestone are the major constituents of the series. However, there is also a dolomitic siltstone that contains variable amounts of chert. The chert ranges from dark, opaque, microfossiliferous and chalcedonic. Glauconite is present and is thinly distributed in southeastern Kansas.

Warsaw Limestone

The Warsaw Limestone includes significant amounts of chert that have distinguishable characteristics. These characteristics include gray in color, mottled, opaque, and microfossiliferous. Glauconite is also present in the lower portion of this unit, along with sponge spicules. The range of thickness varies from 30 to 250 feet.

Salem Limestone

In northeast Kansas, this unit is comparatively deficient in chert and locally chert is not present. In the study area, the unit is a silty dolomite that contains noncherty calcarenite interbedded throughout. It also contains microfossiliferous chert that is similar to that of the Warsaw Limestone. In southwest Kansas the unit is coarsely crystalline and is dominated by oolitic limestone, saccharoidal dolomite, dolomitic limestone, and chert. The thickness of the unit ranges from 50 to 200 feet.

St. Louis Limestone

The St. Louis Limestone contains widespread beds of oolitic limestone and calcarenite. Noncherty lithographic and sublithographic limestones make up the content of the unit that ranges from 50 to 200 feet in thickness.

Genevieve Limestone

The Genevieve Limestone contains interbedded, fine-grained oolitic limestone and calcarenite. This unit is a silty and sandy white limestone that is fossiliferous and ranges in thickness from 30 to 200 feet.

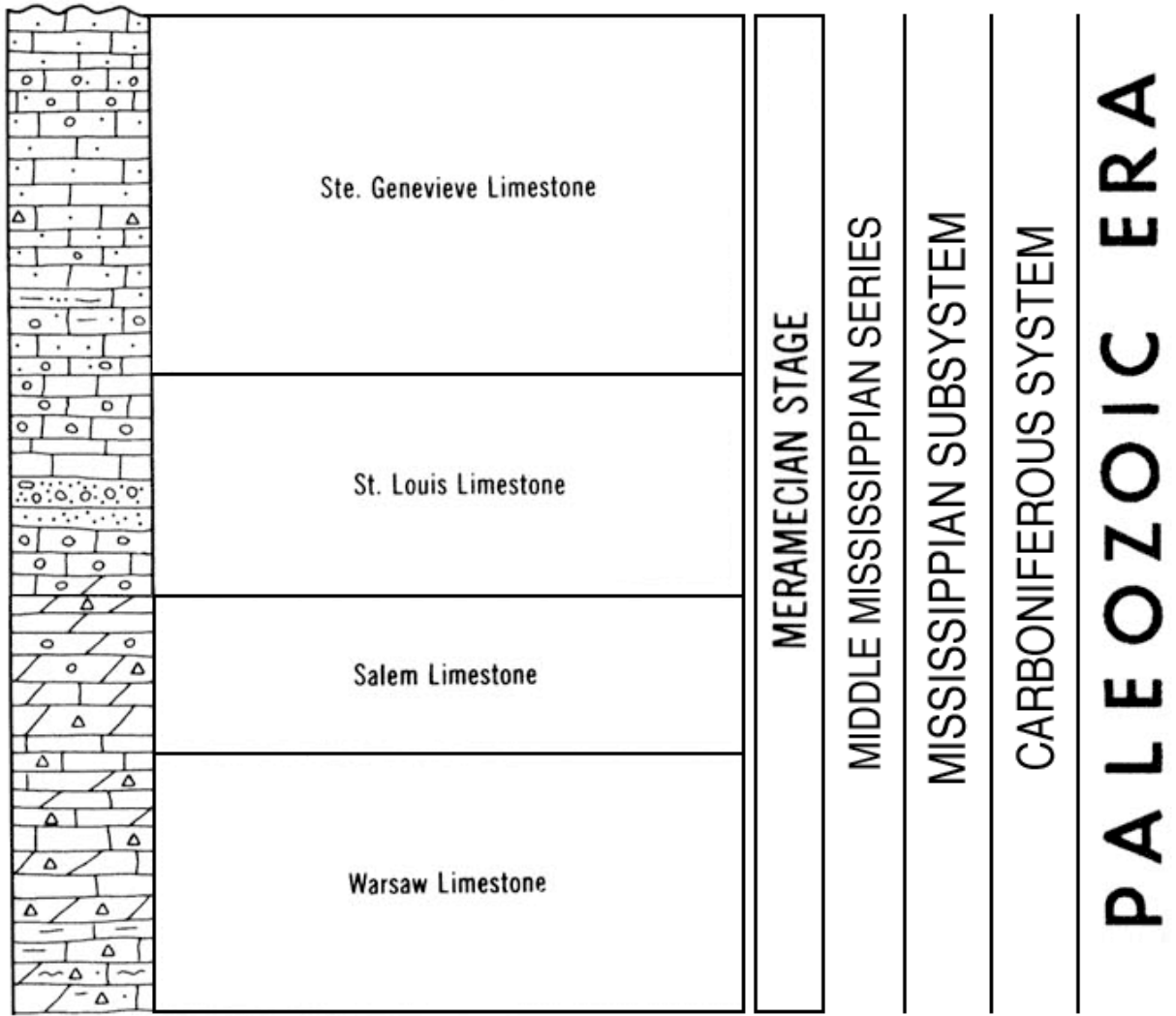


Figure 2.11 Stratigraphic column including the Meramecian Stage of the Mississippian Group that is included in the study. Image from Zellner, 1968.

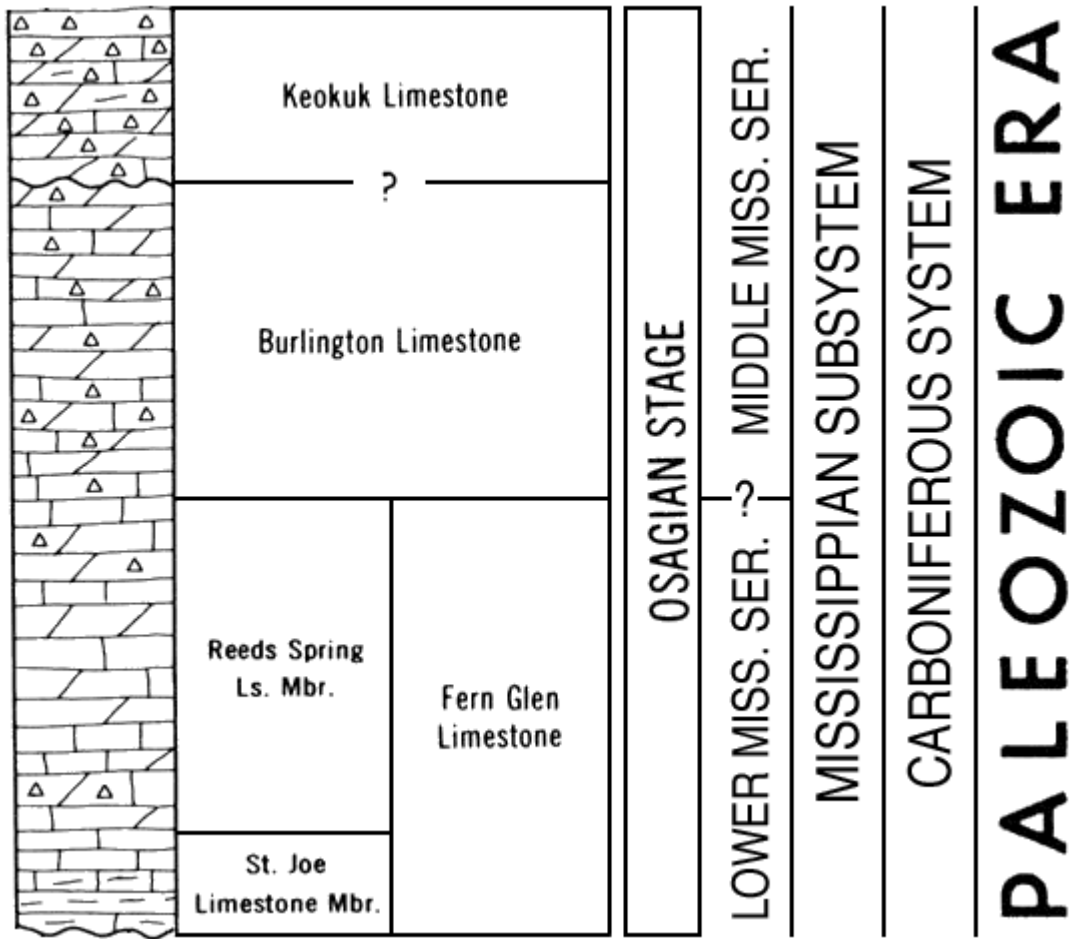


Figure 2.12 Stratigraphic column including the Osagian Stage of the Mississippian Group that is included in the study. Image from Zellner, 1968.

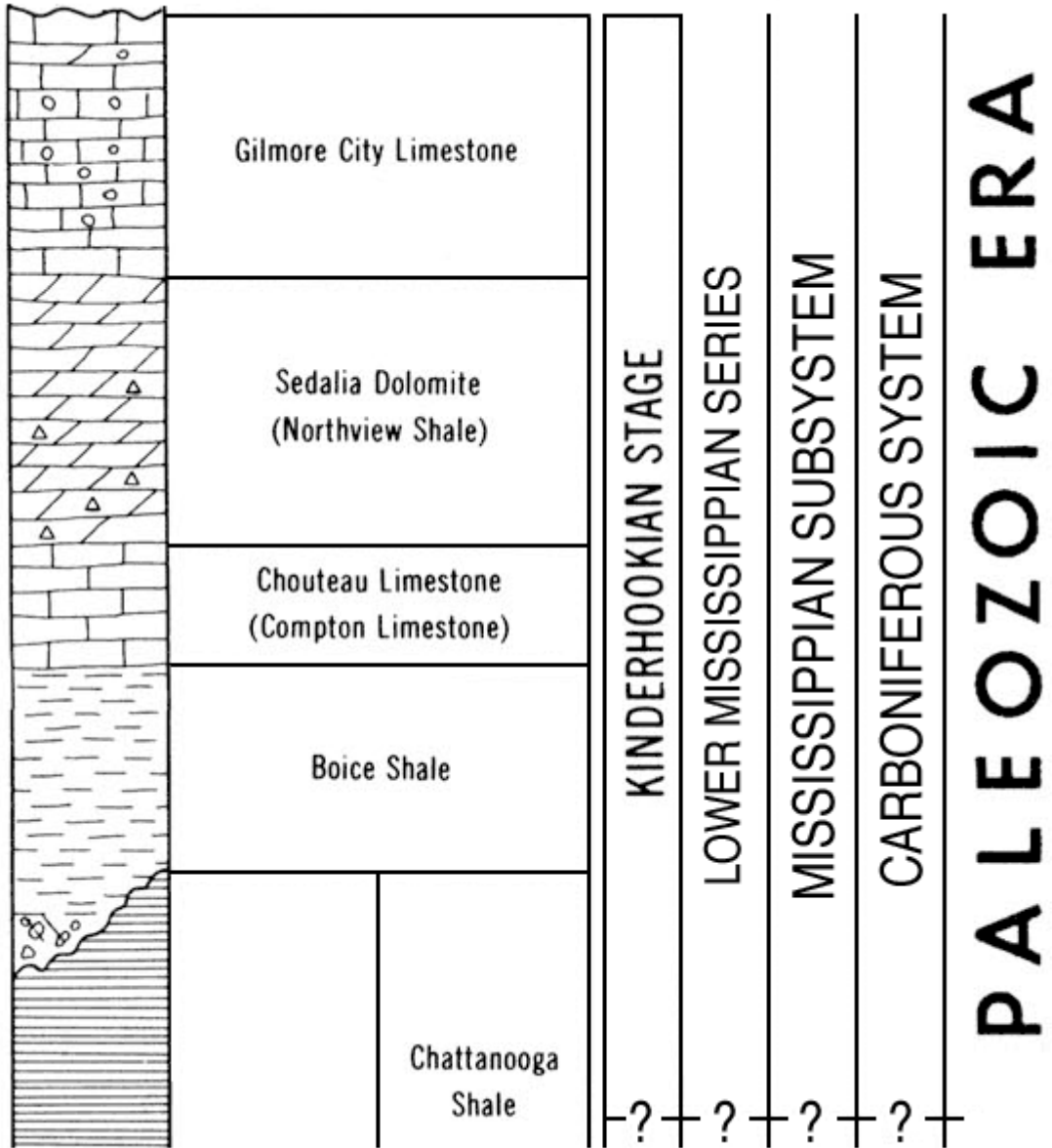


Figure 2.13 Stratigraphic column including the Kinderhookian Stage of the Mississippian Group that is included in the study. Image from Zellner, 1968.

Era- them	System	Series	Stage	Stratigraphic Unit	
Paleozoic	Pennsylvanian	Upper	Virgilian	Wabunsee Group	
				Shawnee Group	
				Douglas Group	
			Missourian	Lansing Group	
		Kansas City Group			
		Pleasanton Group			
		Middle		Des- moinesian	Marmaton Group
			Cherokee Group		
	Mississippian		Upper	Chesterian	
				Meramecian	
		Lower	Osagean		
			Kinderhookian		
			Ordovician	Upper	Maquoketa Shale
					Viola Group
			Middle	Simpson Group	
Lower	Arbuckle Group				
		Cambrian	Upper	Reagan Sandstone	
Precambrian	Granite, Schist				

Figure 2.14 Generalized Kansas stratigraphic column showing units from the Precambrian to the Paleozoic. (Carr et al., 2005)

Chapter 3 - Methodology

Ultrasonic velocity measurements have been used in geology and geophysics to gain a better understanding of elastic-wave propagation, elastic properties, and elastic wave attenuation (Simmons, 1965). Grochau and Gurevich (2009) conducted a study using both sonic logs and ultrasonic laboratory velocity measurements to try to better understand Gassmann fluid substitution. The integrated use of these types of data is similar to that of this study. However, it is important to note that there are other fluid substitution models, including, but not limited to, Biot's relations, Marion's bounding average method, Mavko-Jizba squirt relations, and Biot-squirt model (Mavko et al., 2009).

Ult 100 Ultrasonic System

The system used throughout the course of my work was the Ultrasonic Velocity Measurement System (Ult 100) manufactured by GCTS Testing Systems. This system includes the ULT controller, graphical user interface to the controller, platens that contain piezoelectric crystals, and CATS Ultrasonic software. The setup of the system and the lab can be seen in Figure 3.1. The software is installed on a separate computer and all of the appropriate components on the ULT 100 system are then connected, allowing the two systems to interact.



Figure 3.1 Physical setup of the lab and the GCTS System. Platens on hydraulic press are showing face-to-face setup with pressure gauge affixed to the top.

The main use of ultrasonic velocity measurements is to study the elastic properties of rock core samples. Due to the fact that the system is non-destructive, this is an effective method to test cores that require preservation. The Ult 100 system and the accompanying software are able to generate digital waveforms. Using first arrival time, which is the time it takes a wave to propagate through a given medium, the software can determine compression and shear wave velocities. These velocities are then used by the system to calculate dynamic elastic constants such as Young's Modulus, Bulk Modulus, Shear (Rigidity) Modulus, and Poisson's Ratio. The equations for these calculations can be found later in the discussion.

GCTS supplied a standard, already prepared, aluminum core that was used as a model for core sample size and basis for first arrival determination. The specimens were cut as close to this size as possible. However, due to the physical restrictions and limited continuous physical preservation of the core, the exact aspect ratio replication was not always possible. The samples were cut perpendicular to the cored axis. Dimensions were precisely measured and volumes and densities were then calculated.

The face-to-face platen measurement, if not already completed by GCTS, needs to be run before any other measurement. This is the arrival time where the platens are placed directly on top of each other with only an acoustic couplant in between the surfaces. This takes a reading with essentially no attenuation involved. The acoustic couplant, in this case honey, eliminates air between the platens. This is important because P and S waves will not propagate through air. During this initial test, it is crucial to ensure that the waveforms are strong and coming through properly. The face-to-face arrival times are used as a constant that are eliminated from the compression and shear waves to determine proper first arrival time using the following equation:

$$\text{Velocity} = (\text{height of specimen}) / (\text{arrival time} - \text{platen "face-to-face" arrival time})$$

Once a proper and consistent waveform is detected from the face-to-face measurements, the next step is to test the standard aluminum core provided by the GCTS as seen in Figure 3.2. If there are any problems with the wave detection, then it is necessary to reevaluate the system's connections and the software's parameters. This is also an opportunity to properly grasp how to determine first arrival locations, and therefore times, for both the S-wave and the P-wave. Piezoelectric crystals were used to generate a mechanical vibration from an electric source at ultrasonic frequencies, and an aluminum

rod was used as a standard for the system's calibration. The software includes a manual with ideal properties (V_p and V_s) that should be determined by the ultrasonic velocity measurement system for the aluminum sample. Replicating velocities within the standard values for the aluminum core ensures that the system is functioning properly and that the first arrival locations are correct. After running the preliminary tests and making sure there were no malfunctions with the equipment or system, we were able to run our core samples with confidence of the results.



Figure 3.2 Picture of Ult 100 System showing the platens and aluminum core.

Velocity measurements on the rock core specimens generate digital waveforms for both the P- and S-wave, as seen in Figures 3.3 and 3.4. This is also where the location of the signal's first arrival time is determined.

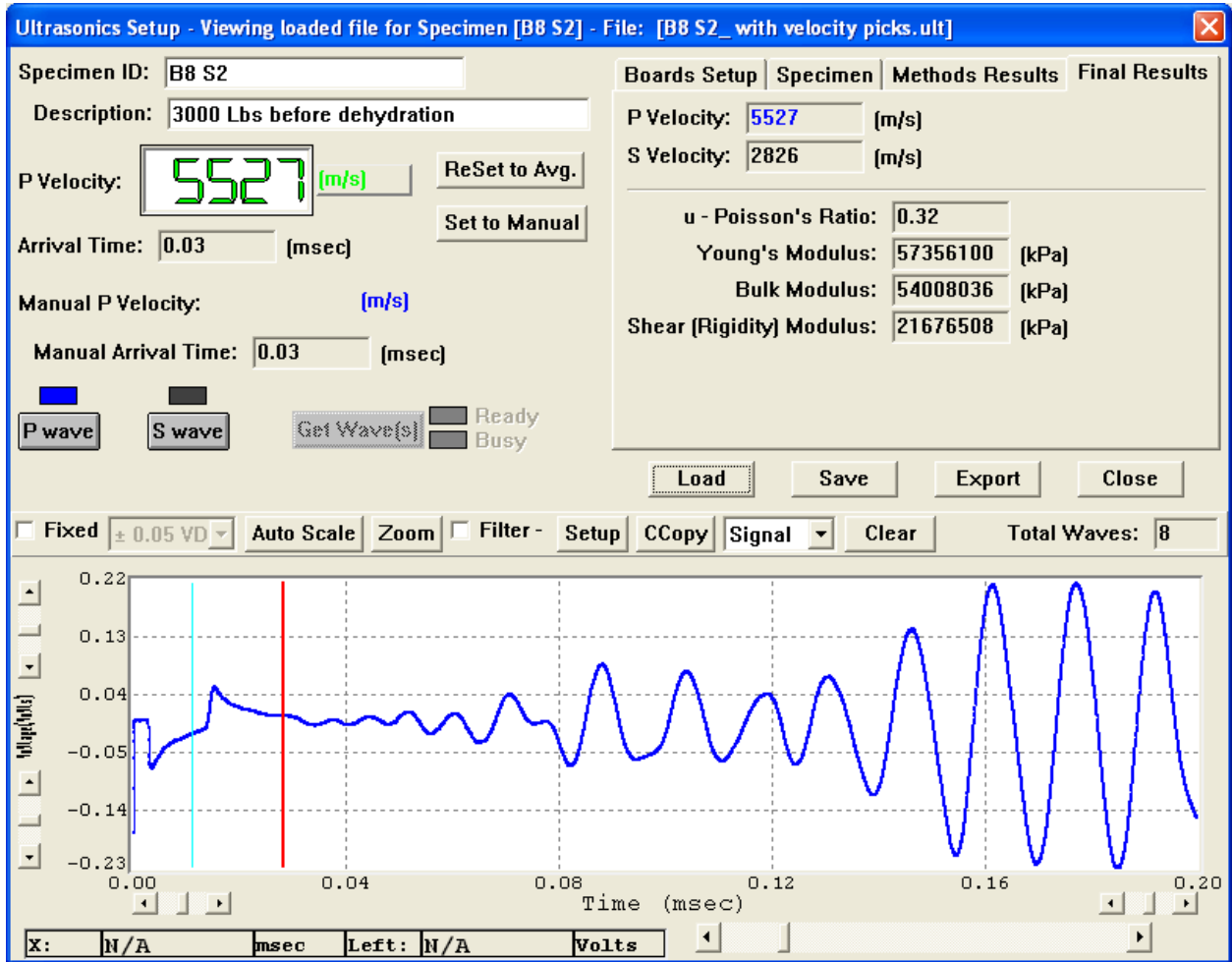


Figure 3.3 Sample B8S2 digital P waveform generated from Ult 100 system at 3000 lbf.



Figure 3.4 Sample B8S2 digital S waveform generated from Ult 100 system at 3000 lbf.

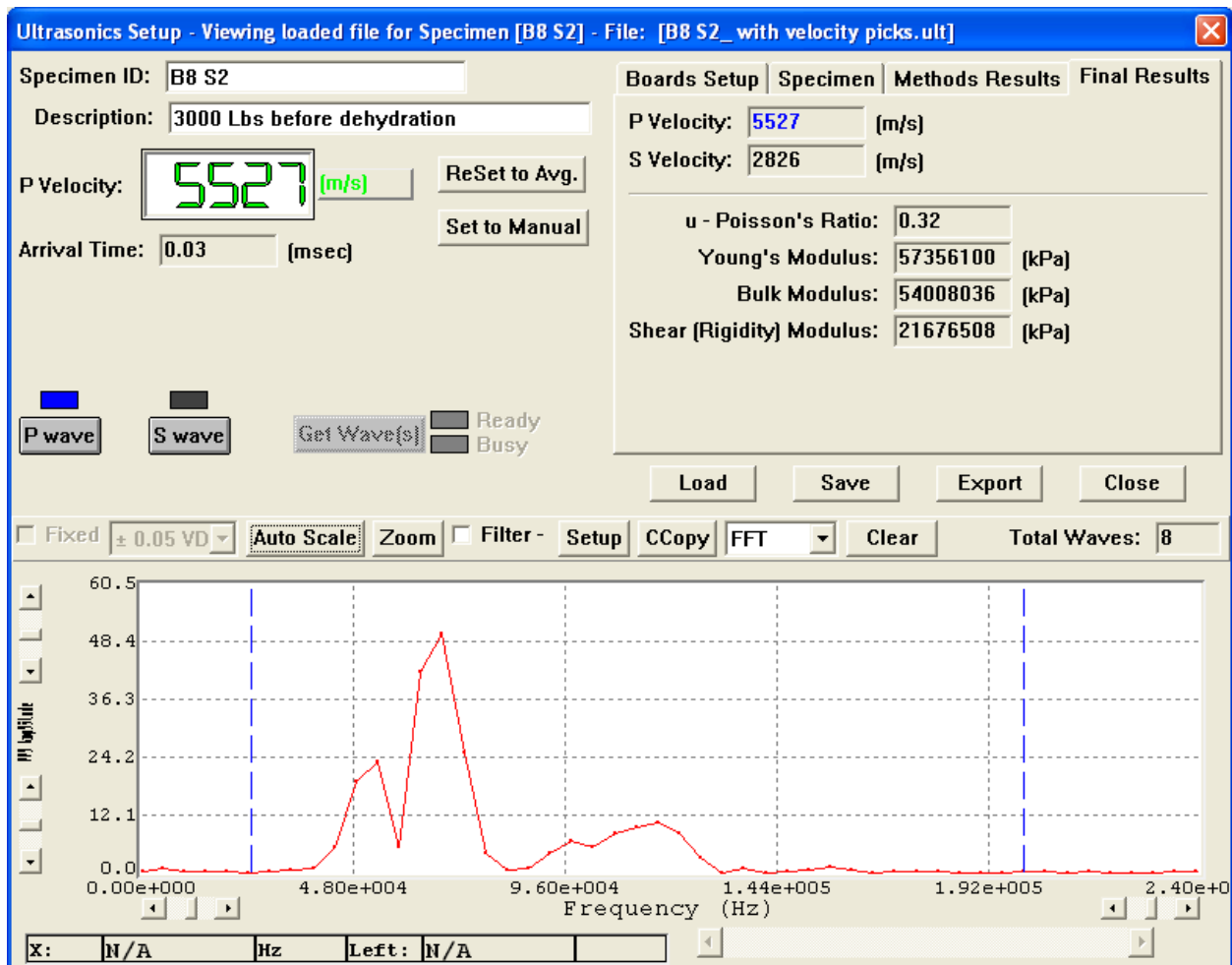


Figure 3.5 Display showing an example of FFT amplitude spectra of a signal showing bandwidth frequency used for measurements.

In this study, both siliciclastic and carbonate rocks were tested using the Ult 100 system. These samples ranged from near surface to approximately 4700 feet in depth. Within the testing parameters of the system, the user is given the option to identify the sample type. This allows the system to use the preset values for the given lithology as a comparison for acquired values. However, if the lithology is unknown, or too complex to fit in a given category of rock type, this selection can be left out without any interference to the software.

Wave propagation through a sample can be affected by a number of factors. Some of these factors include rock type, density, porosity, texture, stress, water content, heterogeneous lithologies and temperature. Randomly oriented discontinuities throughout a sample have the ability to significantly weaken the signal. Operating the system at a low frequency can minimize attenuation losses. Reducing the energy output will minimize excessive wave refraction that can occur with high outputs. The wave refraction may be a problem for short specimens. If there is noise present during the testing, averaging the waveforms will decrease the influence of noise.

Ultrasonic P-wave and S-wave velocities

It is essential to determine the precise location of the signal's first arrival, because this location is used to determine the wave's velocity.

$$V = L/T_f$$

Where V is the velocity, L is the sample length and T_f is first arrival time of signal. The system allows for automatic determination or manually picking of the first arrival.

Automatic Determination of Velocities

Determination of velocities is highly dependent on establishment of proper first arrival times. The arrival time methods that are given as options for Automatic Determination from the system are Absolute Threshold, Relative Threshold, Relative of First Peak, First Peak Time, and Tangent of First Peak as stated in the GCTS User Manual.

Absolute Threshold – The arrival time is determined as the value of the first point that passes the absolute threshold. When the signal value is equal to or has been exceeded

for the first time. The absolute threshold method is given in millivolts and the default is at 10 mV. This method is shown in Figure 3.6.

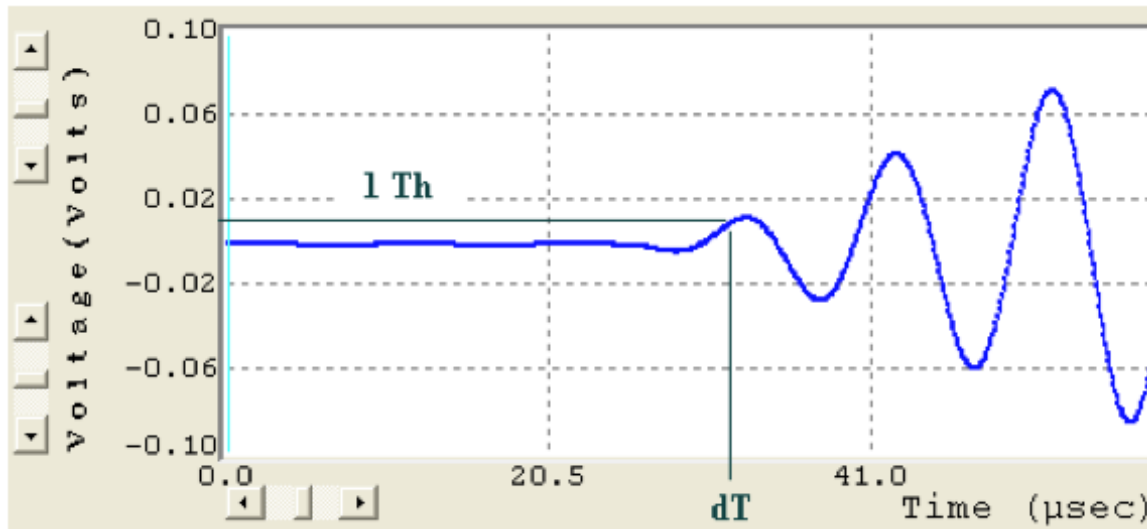


Figure 3.6 Automatic picking display for the absolute threshold method from the C.A.T.S. Ultrasonic software. Image from GCTS User Manual.

Relative Threshold – Arrival time is determined as the time value of the first point to pass the relative threshold. The relative threshold is defined as the maximum amplitude of the signal multiplied by the relative threshold as defined. The time value is taken when the signal is equal to or exceeds the relative threshold of the maximum signal amplitude. This is given in percentages and has a default of 3 percent for this method of automatic determination. This method is shown in Figure 3.7.

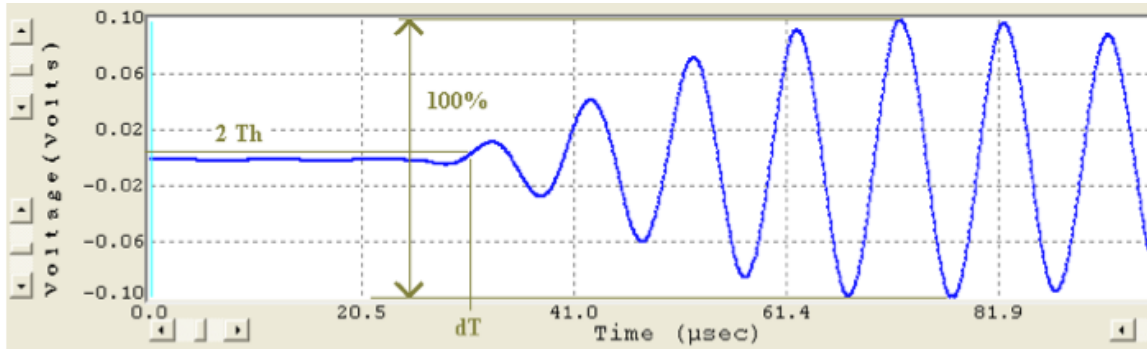


Figure 3.7 Automatic picking display for the relative threshold method from the C.A.T.S. Ultrasonic software. Image from GCTS User Manual.

Relative of First Peak – This method selects the arrival time to be the time value of the signal at which the first peak amplitude threshold is equaled or exceeded for the first time. This is determined as a percentage of the first peak amplitude. The first peak is established by using the absolute or relative threshold method, or an average using a combination of both. The default is set at 10 percent. This method is shown in Figure 3.8.

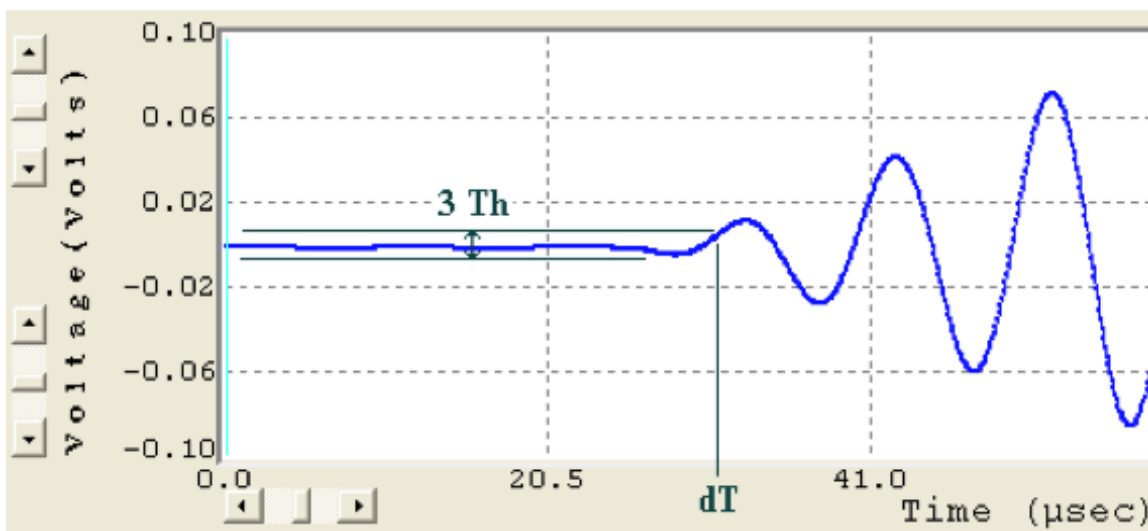


Figure 3.8 Automatic picking display for the relative of first peak method from the C.A.T.S. Ultrasonic software. Image from GCTS User Manual.

First Peak Time – This method of determination uses the time value of the signal at the maximum value of the first peak. The first peak is picked using the absolute or relative threshold, or a calculated average of both methods. However, this is not recommended for S-waves, because the first trough is the suggested correct pick. This method is shown in Figure 3.9.



Figure 3.9 Automatic picking display for the first peak time method from the C.A.T.S. Ultrasonic software. Image from GCTS User Manual.

Tangent of First Peak – Arrival time is equal to the signal value at which the tangent line to the first peak touches the mean value of the signal line. Only the first peak values that equal or precede the first peak amplitude upper threshold are used for the calculation of the tangent line. It is also important to note the difference between the First Peak Amplitude Upper Threshold, default of 85 percent, and the First Peak Amplitude Lower Threshold, default of 15 percent. This method is shown in Figure 3.10.

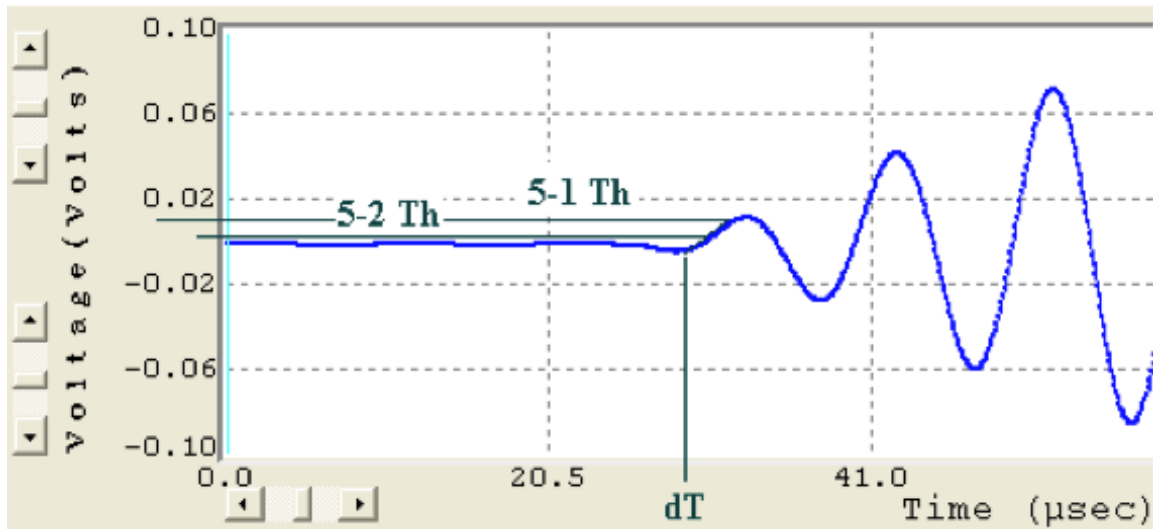


Figure 3.10 Automatic picking display for the tangent of first peak method from the C.A.T.S. Ultrasonic software. Image from GCTS User Manual.

Though automatic determination of velocities can be beneficial, it poses more problems than solutions for picking first arrival times in our project. With low amplitude waves, the program is never able to place an exact location of first arrival and therefore leaves the velocity undermined as seen in Figure 3.11. In Figure 3.12, the amplitude of the wave is high enough for the system to pick a location of first arrival. However, the location of the pick is not in the correct place. The accurate position of the first arrival for the P-wave is shown in Figure 3.14.

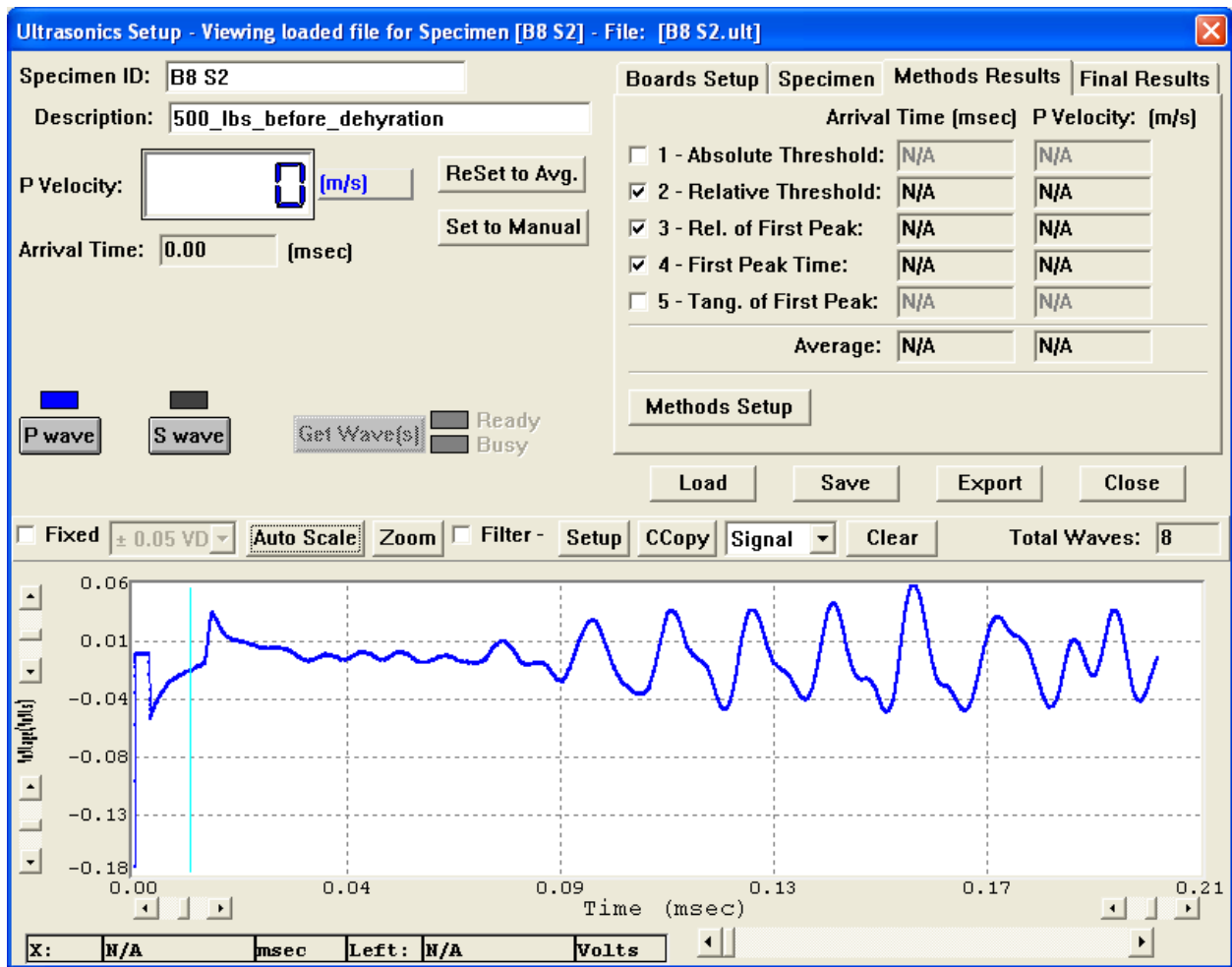


Figure 3.11 Sample B8S2 using automatic determination picking methods for the P-wave at 500 lbf before dehydration.

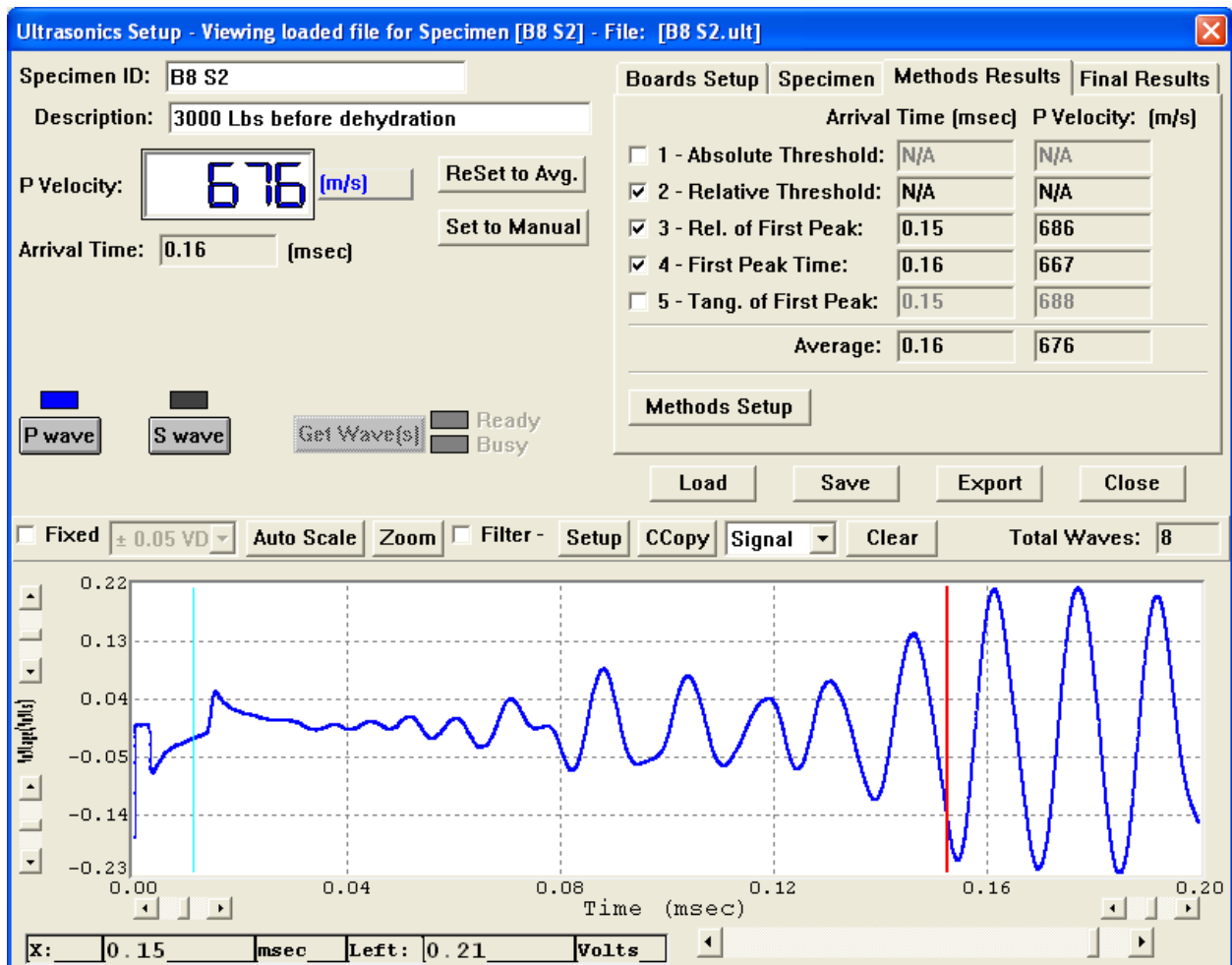


Figure 3.12 Sample B8S1 using automatic determination picking methods for the P-wave at 3000 lbf before dehydration.

Manual Determination of Velocities

Instead of using the automatic determination process from the CATS software, the user can manually select the location on the wave that indicates first arrival. When manual picking, the location to make the pick is where the waveform becomes repeatable. A low amplitude wave can make locating the precise position on the waveform a complicated task and reduces the accuracy of the pick's location. From a number of trial and error efforts of

manual picking, we developed the most accurate and effective method possible for this study.

On each core specimen, multiple velocity measurements were run with increasing force. We then exported these waveforms and graphically stacked them to identify the variations occurring. In every case, there was a clear spot of signal departure from the reproducible noise to the first onset of the S waveform. This separation of waveforms indicates the location of first arrival of the signal. However, identifying the departure in waveforms for P-waves involves a different process, because of the smaller amplitude variation at the location of the first arrival. This initially led to the integrated process of using the largest amplitude wave to establish the first arrival time, and then using the first significant peak or trough to create a shift to apply to the rest of the waveforms for a given sample. However, this method always under predicted the velocities, and when applied to the aluminum core (standard), the first arrival never determined the correct velocities. This created a few questions that were answered by stretching the Y-axis to see the site of the much smaller waveform deviation (Figure 3.13). From here, the location on the waveform can be constantly picked for the sample, which will yield proper P-wave velocities. The correct location of the first time arrival is where the waveform begins, indicated by the ellipse in Figure 3.13. Manual determination is preferred and used for this project in order to provide consistency and accuracy with each first arrival pick. After viewing numerous P and S waveforms, we noticed a similar, yet distinctively different, pattern consistently occurring. The P waveform displayed an early onset, followed by low amplitude and erratic waves until a defined waveform was present. However, for the S waveform, there was very low amplitude noise, then a clear departure of the wave for the

first arrival. This could potentially be due to the wave propagation differences in P- and S-waves. To validate this, more research would need to be conducted.

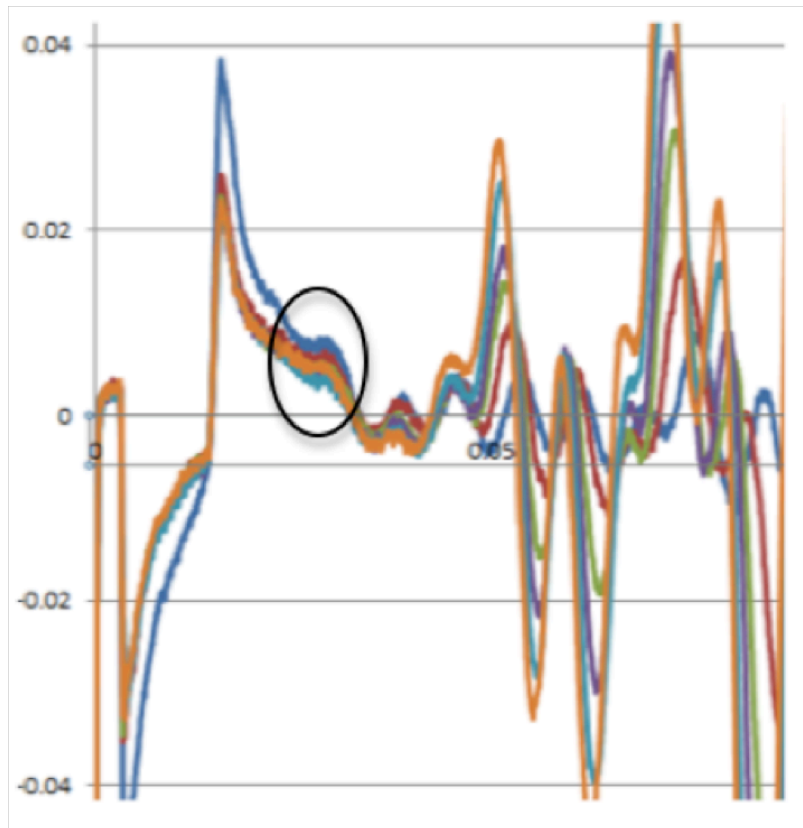


Figure 3.13 Enlarged picture of stacked P waveforms showing beginning of waveform, ellipse indicates area of first arrival.

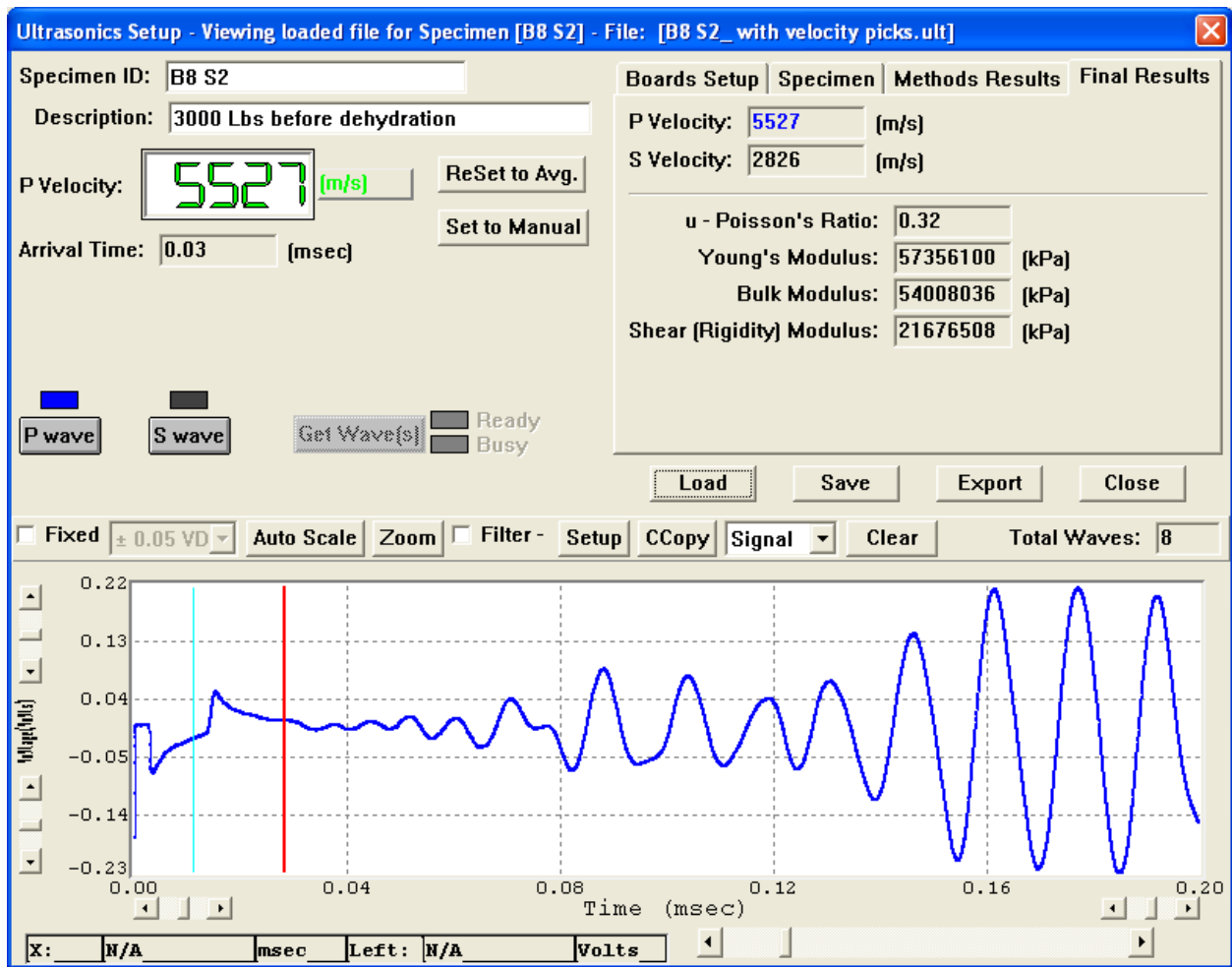


Figure 3.14 Sample B8S1 using manual determination for picking first arrival of the P-wave at 3000 lbf before dehydration.

Final Velocities and Elastic Moduli Results

With the specimen's physical properties (height, diameter, mass), density, waveforms, and velocity, the software is then able to calculate Poisson's Ratio, Young's Modulus, Bulk Modulus, and Shear (Rigidity) Modulus. These elastic moduli are measures of the specimen's stiffness and use ratios of stress to strain for calculation.

Poisson's Ratio is dependent on P- and S-wave velocities. It is determined by the ratio of lateral strain to axial strain in an axial loaded specimen. The formula is valid only within the elastic limit of a material.

$$\sigma = (\alpha^2 - 2\beta^2) / (2(\alpha^2 - \beta^2))$$

$$\sigma = (3K - 2G) / (6K + 2G)$$

$$E = 2G(1 + \sigma) = 3K(1 - 2\sigma)$$

$$K = EG / (3(3G - E))$$

$$V_s = \sqrt{G/\rho}$$

Where σ is Poisson's ratio, α is velocity of P-waves, β is the velocity of S-waves, E is Young's Modulus, K is bulk modulus, G is Shear Modulus, and ρ is density.

Testing Procedures

KDOT Cores

The near surface cores provided from the Kansas Department of Transportation were contributed to the project without a need for them to be returned. This allowed for destructive testing, if necessary. For each sample, we ran ultrasonic velocity measurement tests with an acoustic couplant (honey), and then with increasing uniaxial pressures in 500 lbf (pound force) increments. When measuring less competent rock core specimens, we only measured up to 1000 lbf prior to dehydration, to guarantee preservation of the core. With more competent samples, we measured up to 3000 lbf before dehydration. Pound force can be converted into effective stress of pound per square inch (psi) by taking the lbf and dividing it by the cross sectional area of the core that contacts the platen. Each sample was then dehydrated to a given point, according to its size and lithology. Monitoring and

measurements, during the dehydration process, were taken every 30 minutes in order to prevent over drying. Due to the lack of water saturation knowledge for each core, they were removed from the drying oven when mass reduction became insignificant. If the rock is completely dry, predicted velocities will be too fast, so small amounts of moisture are considered to be the “dry rock” (Smith, et al., 2003; Clark, et al., 1980). After dehydration, ultrasonic velocity measurements were taken in increasing increments of 500 lbf up to 3000 lbf on all cores. This data can be found in Chapter 4.

KGS Cores

The cores supplied from Kansas Geological Survey and Department of Energy are part of an ongoing study focused on geologic sequestration of carbon dioxide, and required non-destructive testing. The cores for this study were taken from a range of 3717.9 to 4626.9 feet in depth and were able to naturally withstand more pressure exertion than the other set of cores. For this set of core testing, we again varied the pressures in increments of 500 lbf, but did not dehydrate the cores. This is because the cores are part of a larger, ongoing study and required non-invasive testing or alterations. The pressure testing concluded at the general depth equivalent. Using an approximation of 2.3 g/cm³ as the average overburden grain density, we calculated that one foot of burial is equal to effective stress of one psi. After this calculation, we were able to determine the force needed in lbf to equal the psi each core would be experiencing at in situ conditions in a uniaxial direction.

Applied “overburden” stress (psi) = Force (lbf)/cross-sectional surface area of core (square inch)

Gassmann Modeling

In rock physics, the fluid substitution problem is considered to be one of the most important issues of concern. Trying to predict the wave velocities after fluid substitution is a complex task, even with the integrated analysis of well logs, cores, and seismic data. Fluid replacement modeling can be very beneficial for reservoir monitoring. As stated by Mavko et al. (2009), Gassmann's relations can estimate the change of a porous media's elastic moduli, at low frequencies, when there is a change in pore fluid saturation. Using both compression and shear velocities, with rocks saturated with the initial pore fluid (or gas), fluid substitution can be performed by extracting the bulk and shear modulus. Then, using Gassmann's relations velocities can be recreated with the bulk modulus of the rock with pore space occupied by the substituting fluid (Mavko et al., 1998). The use of Gassmann's theory has been applicable for modeling fluid substitution through the integration of the saturated bulk modulus, bulk modulus of mineral matrix, bulk modulus of pore fluid, bulk modulus of porous rock frame and porosity. The equation for saturated bulk modulus is seen in the following equation:

$$K_{sat} = K^* + \frac{\left(1 - \frac{K^*}{K_o}\right)^2}{\frac{\Phi}{K_{fl}} + \frac{(1 - \Phi)}{K_o} - \frac{K^*}{(K_o)^2}}$$

Where K_{sat} is saturated bulk modulus, K_o is the bulk modulus of mineral matrix, K_{fl} is bulk modulus of pore fluid, K^* is bulk modulus of porous rock frame, and Φ is porosity. Equation from Mavko et al. (2009).

Prior to completing the calculations based on the substitution of fluids, there are certain petrophysical properties that need to be acquired. The components include rock porosity (ϕ), bulk modulus of the fluid (K_{fl}), fluid density (ρ_{fl}) of pore space fluids, mineral matrix's bulk modulus (K_o), and the porous rock frame's bulk modulus (K^*). Through the use of laboratory measurements and analysis of wireline log data, all these properties can be identified or deduced (Smith et al., 2003).

Gassmann modeling can accomplish post saturation prediction of velocities after fluid replacement, when working within the necessary assumptions. These assumptions and limitations include the rock being homogeneous (monomineralic) and isotropic, pore space is completely connected, the system is closed, equilibrium of pore pressure has been reached between pores, and the pore fluid does not chemically affect the solid frame (Mavko et al., 2009; Smith, et al., 2003; Adam et al., 2006). Overgeneralization of application, or improper understanding, of these assumptions can produce invalid outcomes (Smith et al., 2003). In order for mathematical simplification, major assumptions have to be made due to the complexity of the rock-fluid system (Grochau and Guerevich, 2008). However, pore geometry, rock symmetry, inclusion geometry and crack density does not affect the equation's applicability as it does for other fluid substitution theories (Adam et al., 2006).

Gassmann's required assumptions constrain the applicability of the fluid substitution method. Generally, limitations include the use of low frequencies and

siliciclastic rocks. Seismic frequencies (or lower) are used for Gassmann's relations because at these low frequencies, the fluid within the rock has sufficient time to equilibrate. However, the permeability of the rock and fluid's viscosity and density affect the repose time of the fluid (Adam et al., 2006). According to Wang (2000), Baechle et al. (2005), and Rogen et al. (2005), for oil or brine saturated rocks; Gassmann's relations have a tendency to underestimate ultrasonic velocities, with occasional occurrences of overestimation. The application for carbonate rocks is limited because of the complex heterogeneous mineralogy, internal structures and porosity. With the presence of dolomitization, there can be an increase in overall porosity and permeability due to the dissolution of grains or fossils, which helps validate the Gassmann assumption of continuous pore connectivity (Adam et al., 2006). This could potentially make dolomites, with similar scenarios, more applicable for Gassmann's fluid replacement modeling.

Validity of Gassmann's fluid replacement for time-lapse studies is reliant on a number of assumptions for the field (Grochau and Gurevich, 2008). Seismic anomalies or AVO anomalies can potentially be detected through seismic interpretation when evaluating fluid scenarios using the framework provided from Gassmann (Sbar, 2000; Smith et al., 2003).

Through the use of an interactive Excel spreadsheet that includes macro functions used to calculate Gassmann's equation, I was able to complete some theoretical velocity modeling. This interactive spreadsheet was provided by Dr. Abdelmoneam Raef from Kansas State University, and uses Gassmann's equation to model post fluid replacement effects on a given rock medium. As shown in Figure 3.15, this worksheet shows the initial situation of the rock and the associated properties. These can be modified based on what

type of fluid and rock skeleton are being modeled. Porosity, which is a major factor in velocities after saturation, can be changed to mimic realistic and theoretical reservoir values. This is helpful, because porosity is an extremely important factor in reservoir characterization and fluid substitution effects on porosity can potentially be seen as an outcome of velocity variation. For this study, we did both theoretical modeling and modeling for the Sumner County, Kansas field site.

For the modeling based solely on theory, we used average values for a sandstone and limestone, and sub-critical and super-critical CO₂. This was completed to note that the largest control on P-wave velocity variation is a change in CO₂ saturation. The data used for and derived from this modeling can be seen in Appendix C. The modeling conducted for the field site in Sumner County, Kansas used the integration of measurements from both the laboratory and well logs. Two cores were selected for fluid replacement modeling: 4-26 at a depth of 3717.9 feet and 14-4 from a depth of 4247 feet. From the depth of these cores' extraction, V_p and V_s were taken from the sonic and dipole sonic logs. Porosity, grain density and initial water saturation were taken from the whole core analysis done by Weatherford Labs. At room conditions, the density of the core was calculated using mass and volume of the core. We also ran near ultrasonic velocities at *in situ* conditions to derive the inverse of the bulk modulus. Through the integration of these properties and inputting them into the interactive excel spreadsheet, we can model the outcome of V_p, V_s, density, bulk modulus, and Poisson's ratio at a given saturation of a hydrocarbon.

SACS: Calculation of the effect of CO2-saturation						
INITIAL SITUATION		NEW SITUATION		CONSTANTS		Units
Velocities from a rock with water saturation Sw and hydrocarbon saturation Shc are known		Velocities from the same rock with a new water saturation Sw2 and hydrocarbon saturation Shc2 are determined				
SAT ROCK		SAT ROCK (GASSMAN)				
Vp(Sw)	2000	Vp(Sw2)	1152			m/s
Vs(Sw)	630	Vs(Sw2)	655			m/s
RHO(Sw)	1994	RHO(Sw2)	1844			kg/m3
K(Sw)	6.921E+09	K(Sw2)	1.392E+09			Pa
Sw	1.00	Sw2	0.00			
Poisson(Sw)	0.445	Poisson(Sv)	0.261			
ROCK SKELETON				SANDSTONE	SHALE	OTHER
Lithology	SS			SS	SH	OTHER
POR	0.3500					
RHOs	2650			2650	2700	2700
COMPs	2.710E-11			2.710E-11	2.530E-11	2.530E-11
Ko	3.690E+10			3.690E+10	3.953E+10	3.953E+10
INITIAL HYDROCARBON		NEW HYDROCARBON		WATER	OIL	GAS
Hydrocarbon	WATER	Hydrocarbon	gas	water	oil	gas
Shc	0.00	Shc2	1.00			
RHOhc	1090	RHOhc2	660	1090	850	660
COMPhc	4.200E-10	COMPhc2	1.429E-08	4.200E-10	6.300E-10	1.429E-08
TOTAL FLUID (water + hc)		TOTAL FLUID 2 (water + hc2)				
COMPf1	4.200E-10	COMPf2	1.429E-08			1/Pa
Kf1	2.381E+09	Kf12	7.000E+07			Pa
DRY ROCK (GASSMAN)						
Vp(dry)	1184					m/s
Vs(dry)	701					m/s
RHO(dry)	1613					kg/m3
K(dry)	1.206E+09					Pa
Poisson(dry)	0.231					
CALCULATION OF VELOCITIES AFTER FLUID SUBSTITUTION						
AUTHOR: Rob Arts						
ALL Values in Brown have been entered		0.07	1000000000	70000000	1.42857E-08	

Figure 3.15 Figure 21. Picture of interactive Excel spreadsheet used for Gassmann modeling.

Chapter 4 - Data and Results

Core Information

KDOT Core

B8S2

Core sample B8S2 is from the near surface core set, provided by Dr. Keith Miller, in collaboration with the Kansas Department of Transportation from a previous project. The rest of the core data from this set are found in Appendix A. Each core, from the near surface set, has corresponding physical parameters (height, diameter, mass before and after dehydration, and density before and after dehydration). These cores were available for invasive testing, so we were able to dehydrate them to see effects of residual fluids on the elastic properties of the rocks.



Figure 4.1 KDOT Core B8S2, view parallel to cored axis.

Figure 4.2 KDOT Core B8S2, view perpendicular to cored axis.

Sample	Height (mm)	Diameter (mm)	Mass before dehydration (g)	Density before dehydration (g/mm ³)
B8 S2	98	50	522.5	2.42E-03

Table 4.1 Physical properties of sample B8S2 prior to dehydration.

Sample	Height (mm)	Diameter (mm)	Mass after dehydration (g)	Density after dehydration (g/mm ³)
B8 S2	98	50	522	2.71E-03

Table 4.2 Physical properties of sample B8S2 after dehydration.

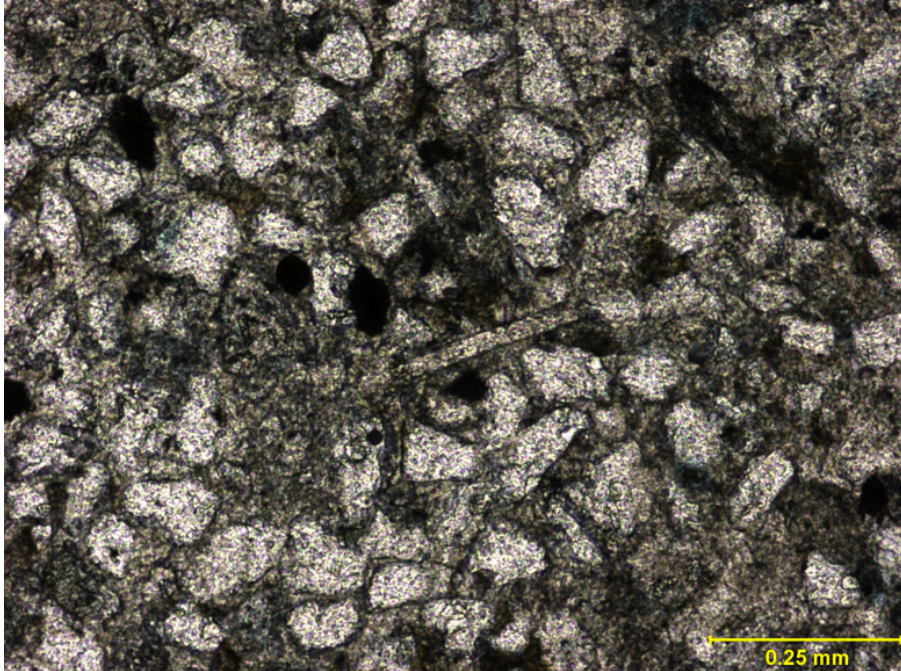


Figure 4.3 Thin section image of KDOT Core sample B8S2. Image is at 10X magnification and in plane polarized light.

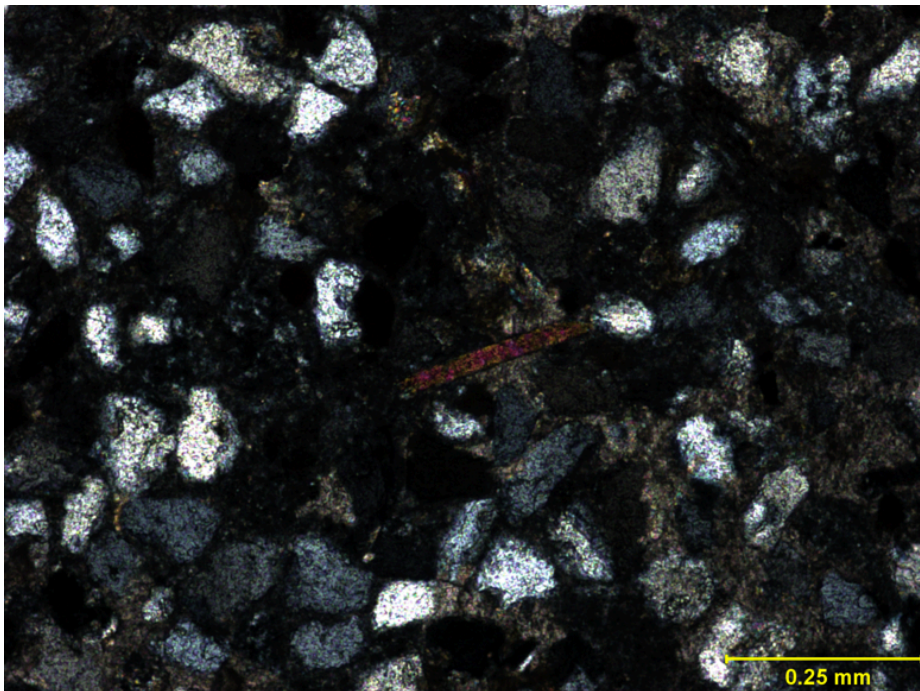


Figure 4.4 Thin section image of KDOT Core sample B8S2. Image is at 10X magnification and in crossed polarized light.

From thin section analysis, as seen in Figures 4.3 and 4.4, sample B8S2 is both grain and matrix supported with sub rounded to angular quartz grains with low porosity. This sample also has calcite cement and shows small amounts of micas, feldspars, and oxides. Looking at the grains in thin section view could potentially explain variations in attenuation differences based on pore and grain architecture. Thin section images of other cores used in this study can be found in Appendix A.

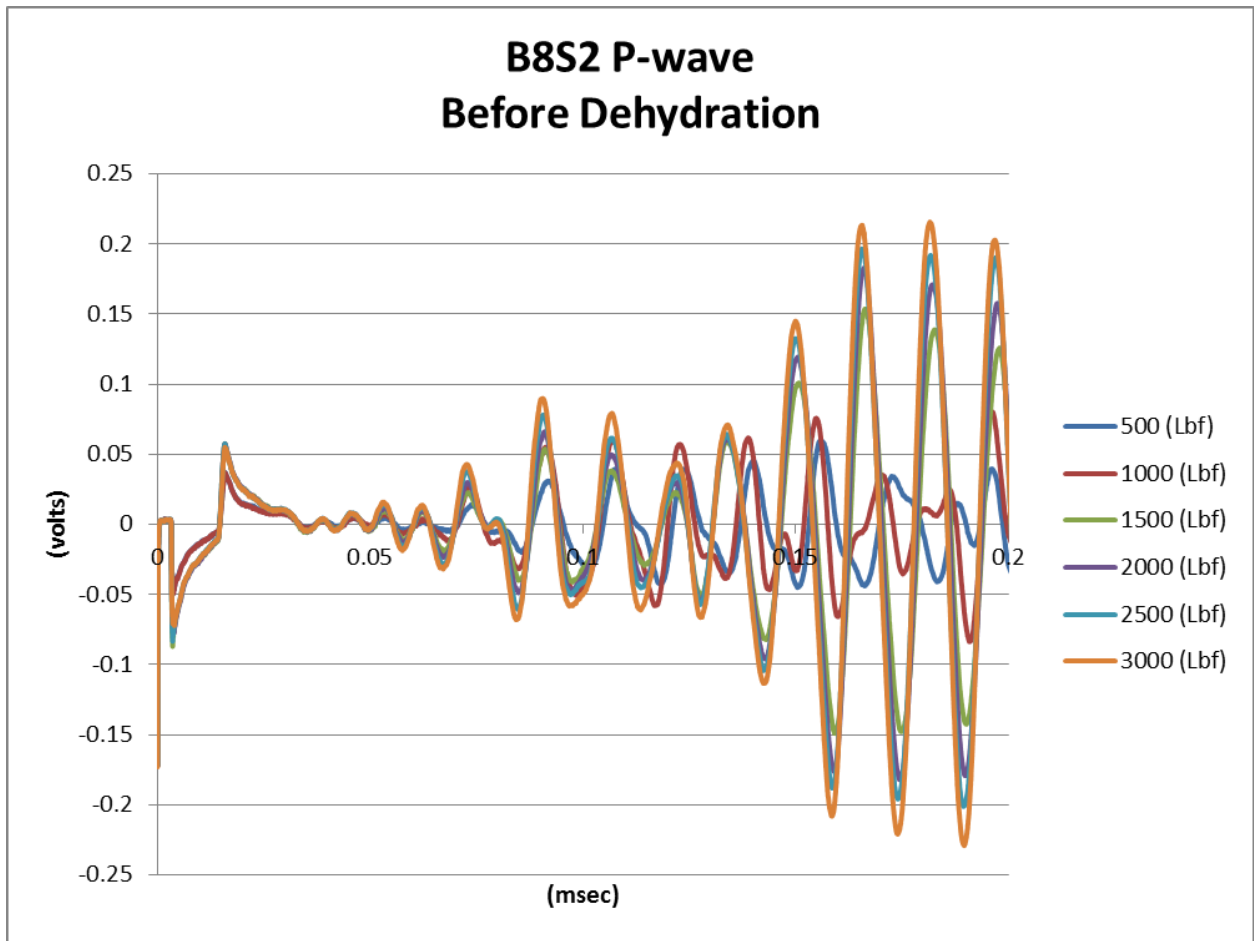


Figure 4.5 Graph of sample B8S2, P waveform from 500 Lbf to 3000 Lbf prior to sample dehydration.

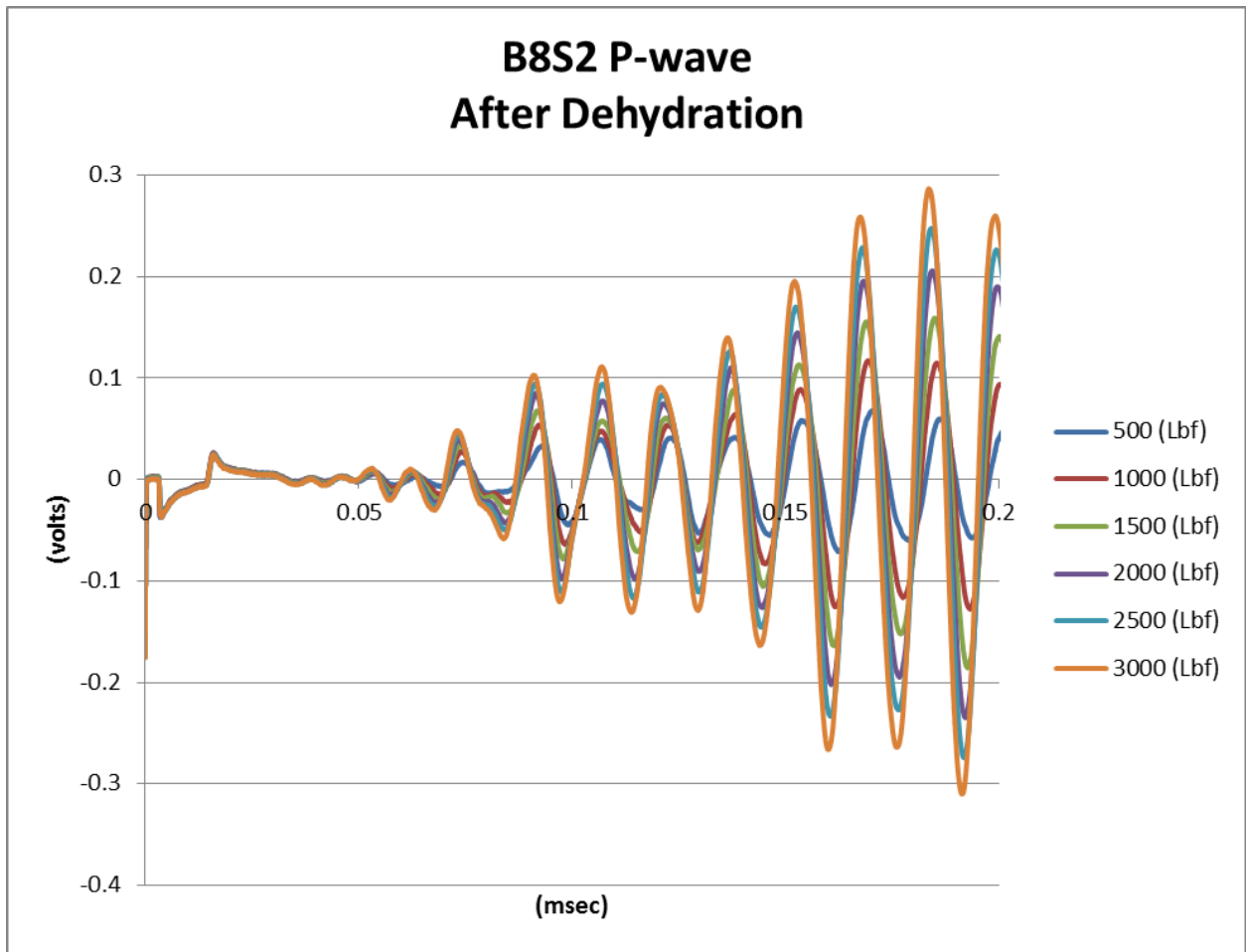


Figure 4.6 Graph of sample B8S2, P waveform stacked from 500 Lbf to 3000 Lbf after sample dehydration.

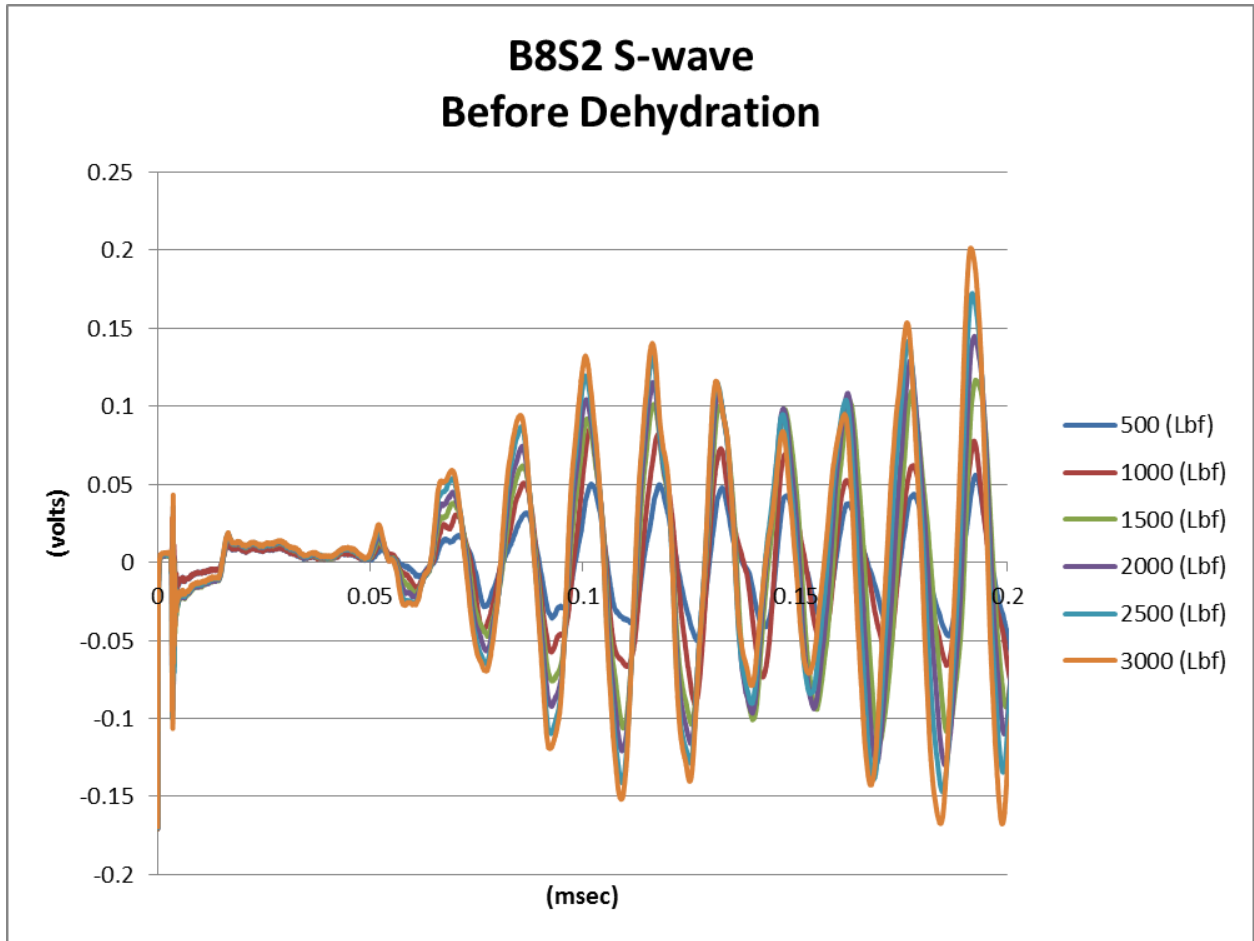


Figure 4.7 Graph of sample B8S2, S waveform stacked from 500 Lbf to 3000 Lbf prior to sample dehydration.

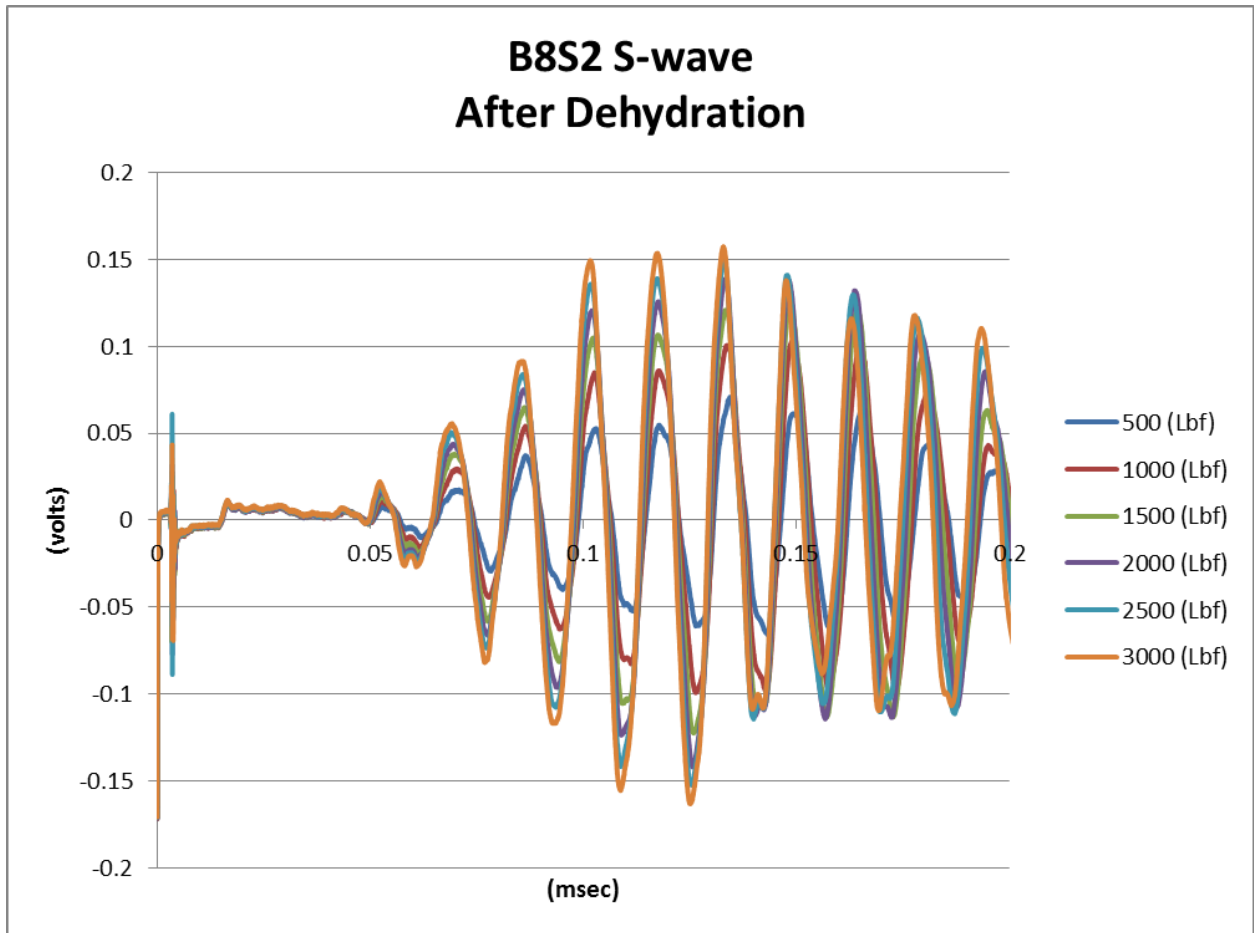


Figure 4.8 Graph of sample B8S2, S waveform stacked from 500 Lbf to 3000 Lbf after sample dehydration.

These stacked waveforms, as seen in Figures 4.5, 4.6, 4.7, and 4.8, give insight to the increase in attenuation and velocity with an increase in effective stress for near surface cores. Tables 4.3 and 4.4 show the P-wave and S-wave velocities and elastic moduli for varying effective stress. Stacked waveform graphs and elastic moduli data tables for the remaining core data can be found in Appendix B.

Lbf	P wave (m/s)	S wave (m/s)	Poisson's Ratio	Young's Modulus (kPa)	Bulk Modulus (kPa)	Shear Modulus (kPa)
500	5291	2756	0.31	54200908	48516240	20627456
1000	5328	2788	0.31	55372376	48947120	21111044
1500	5374	2808	0.31	56165436	49846264	21401176
2000	5415	2819	0.31	56702100	50836544	21574448
2500	5476	2821	0.32	57003300	52577280	21603564
3000	5527	2826	0.32	57356100	54008036	21676508

Table 4.3 Velocity of P- and S-waves and elastic moduli of sample B8S2 before dehydration.

Lbf	P wave (m/s)	S wave (m/s)	Poisson's Ratio	Young's Modulus (kPa)	Bulk Modulus (kPa)	Shear Modulus (kPa)
500	5343	2731	0.32	53542968	50461644	20233050
1000	5483	2753	0.33	54764576	54125740	20567060
1500	5490	2772	0.33	55391780	53975444	20840276
2000	5530	2782	0.33	55866052	54964076	20992832
2500	5558	2797	0.33	56458536	55498864	21217812
3000	5627	2801	0.34	56850356	57498972	21288864

Table 4.4 Velocity of P- and S-waves and elastic moduli of sample B8S2 after dehydration.

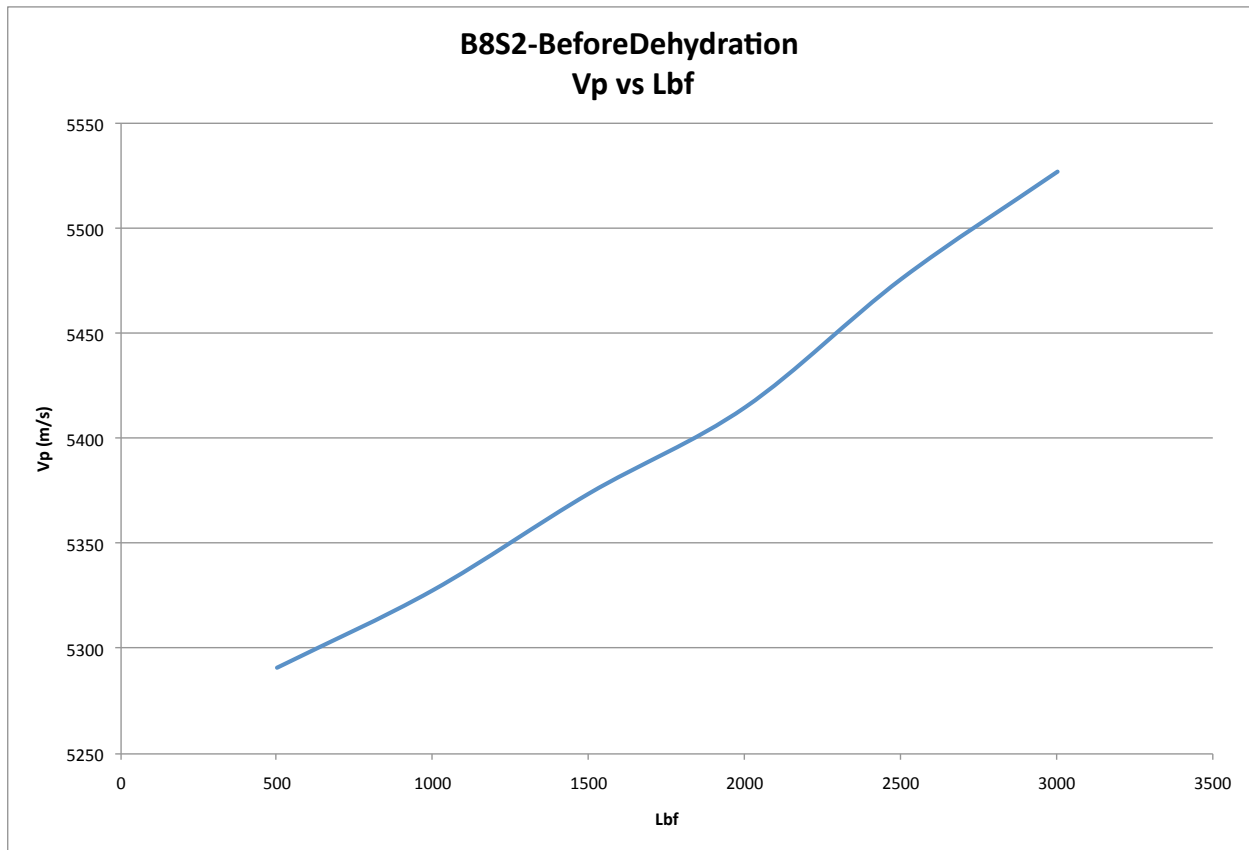


Figure 4.9 Graph comparing P-wave velocity (m/s) to increasing lbf for core sample B8S2 before dehydration. Data used to construct graph in Table 4.3.

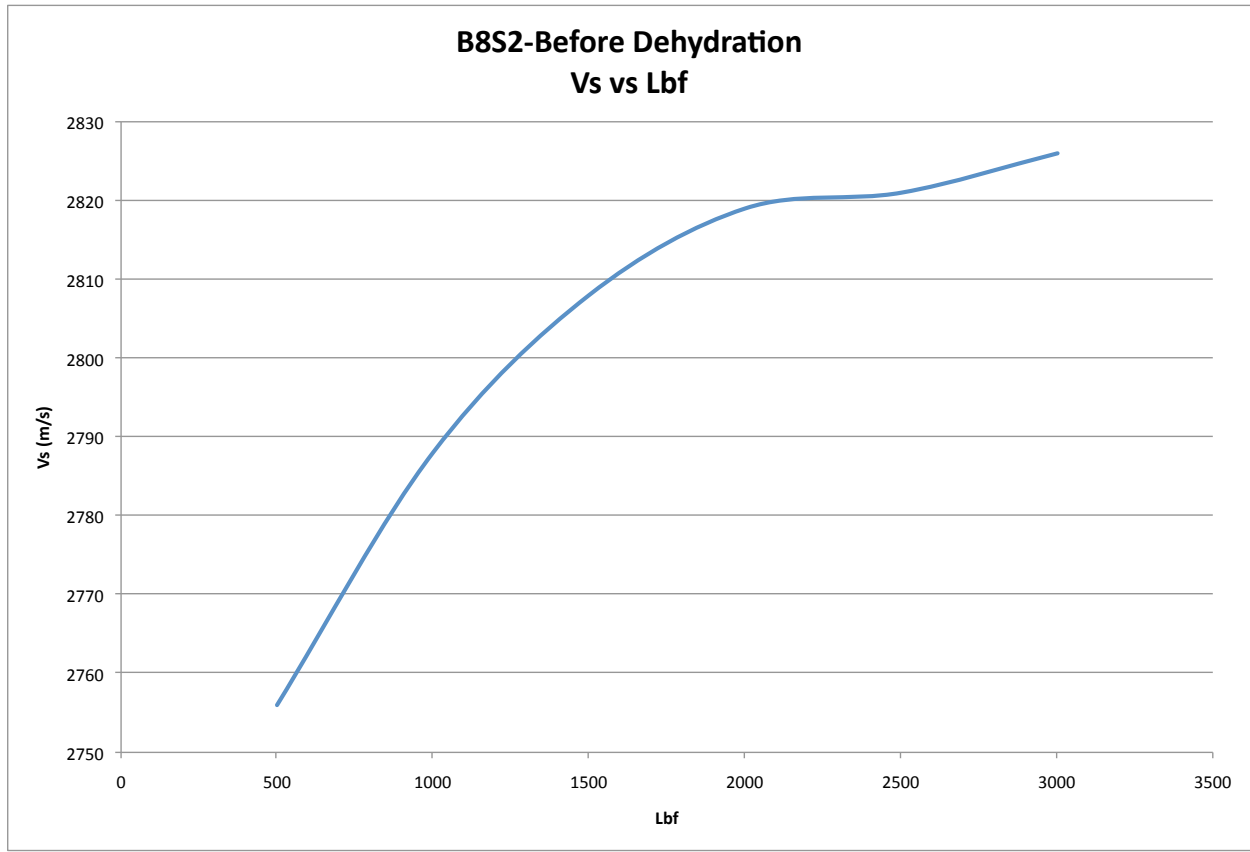


Figure 4.10 Graph comparing S-wave velocity (m/s) to increasing lbf for core sample B8S2 before dehydration. Data used to construct graph in Table 4.3.

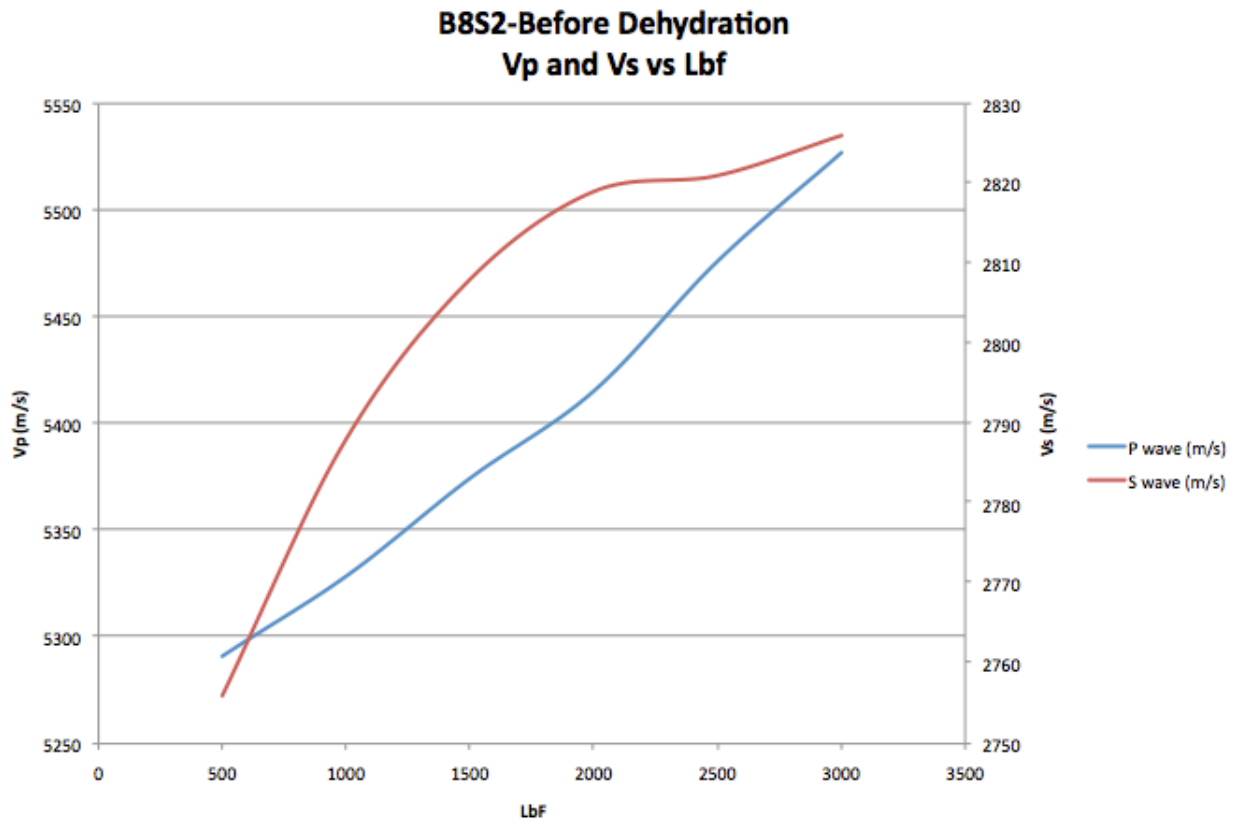


Figure 4.11 Graph comparing P-wave velocity (m/s) and S-wave velocity (m/s) to Lbf for core sample B8S2 before dehydration. Data used to construct graph in Table 4.3.

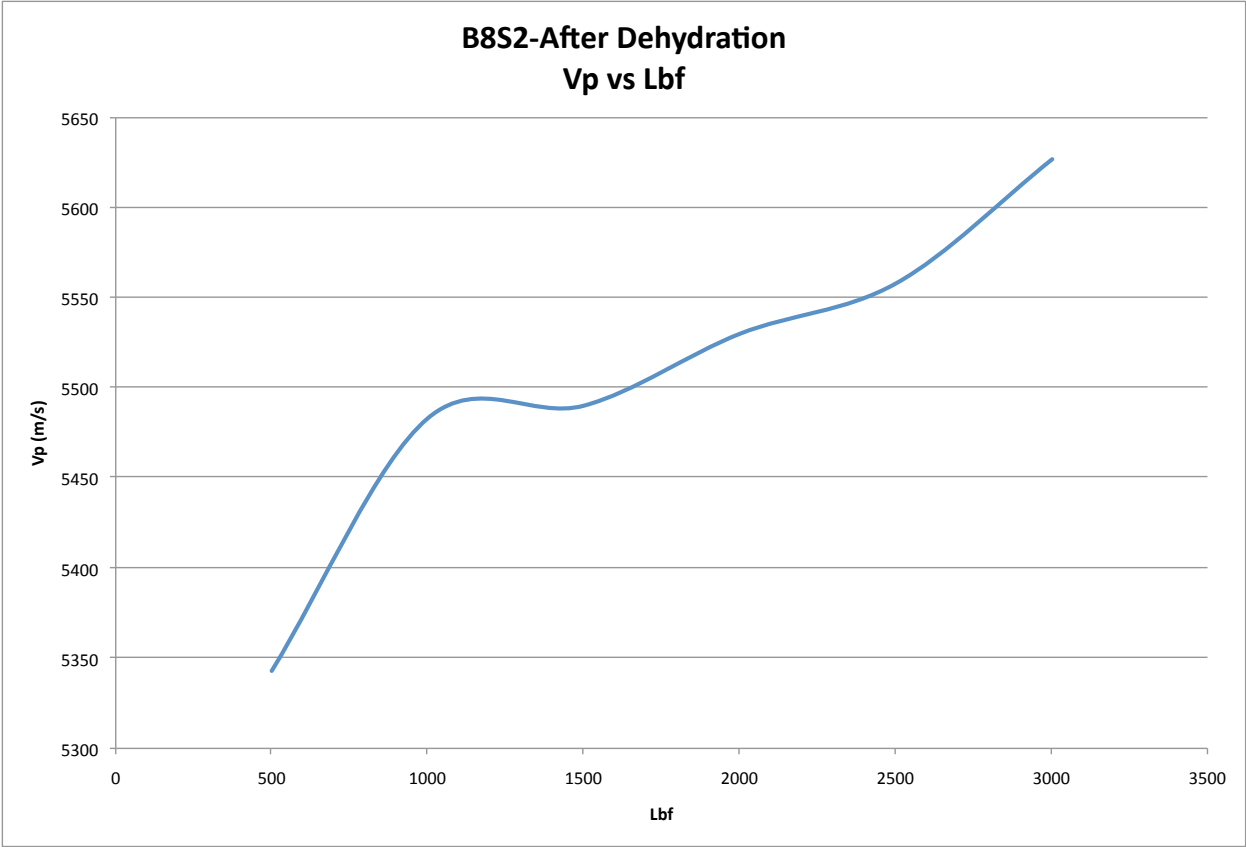


Figure 4.12 Graph comparing P-wave velocity (m/s) to increasing lbf for core sample B8S2 after dehydration. Data used to construct graph in Table 4.4.

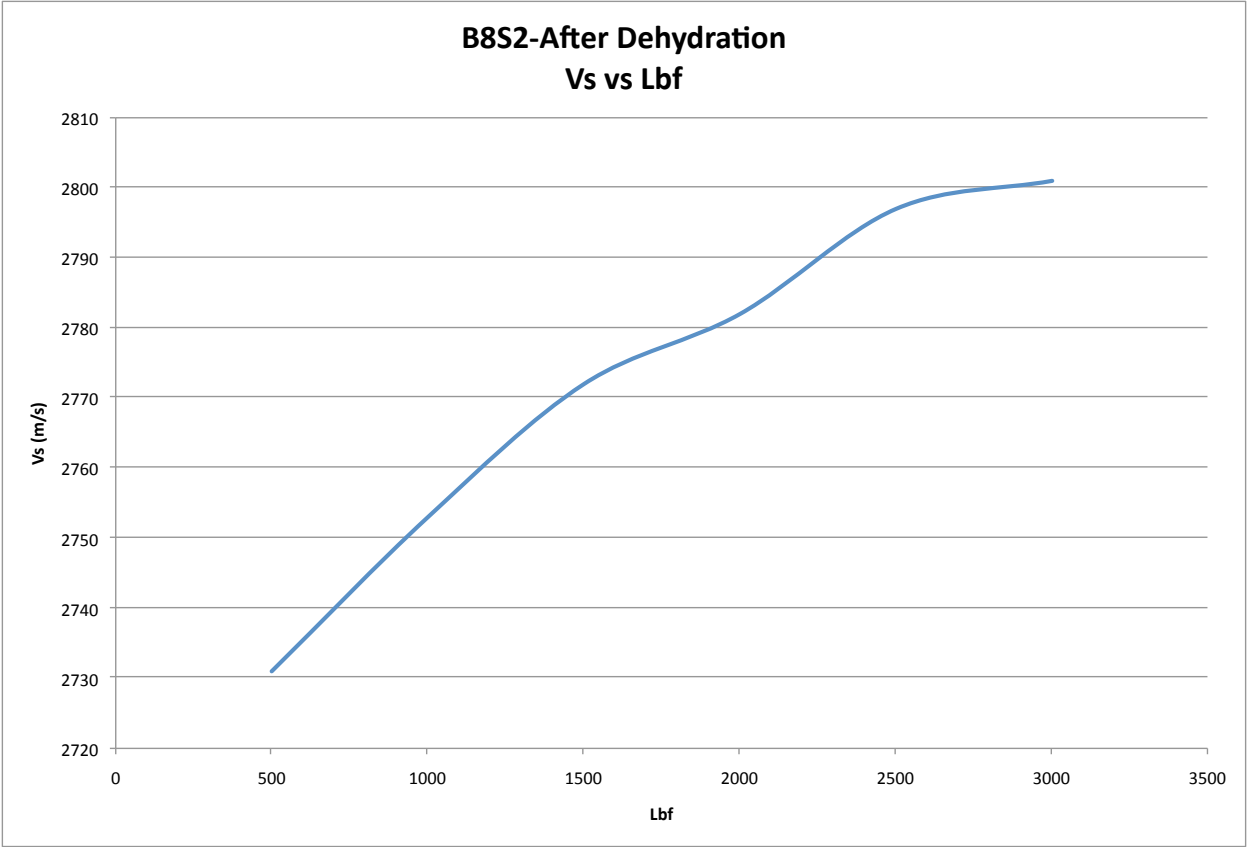


Figure 4.13 Graph comparing S-wave velocity (m/s) to increasing lbf for core sample B8S2 after dehydration. Data used to construct graph in Table 4.4.

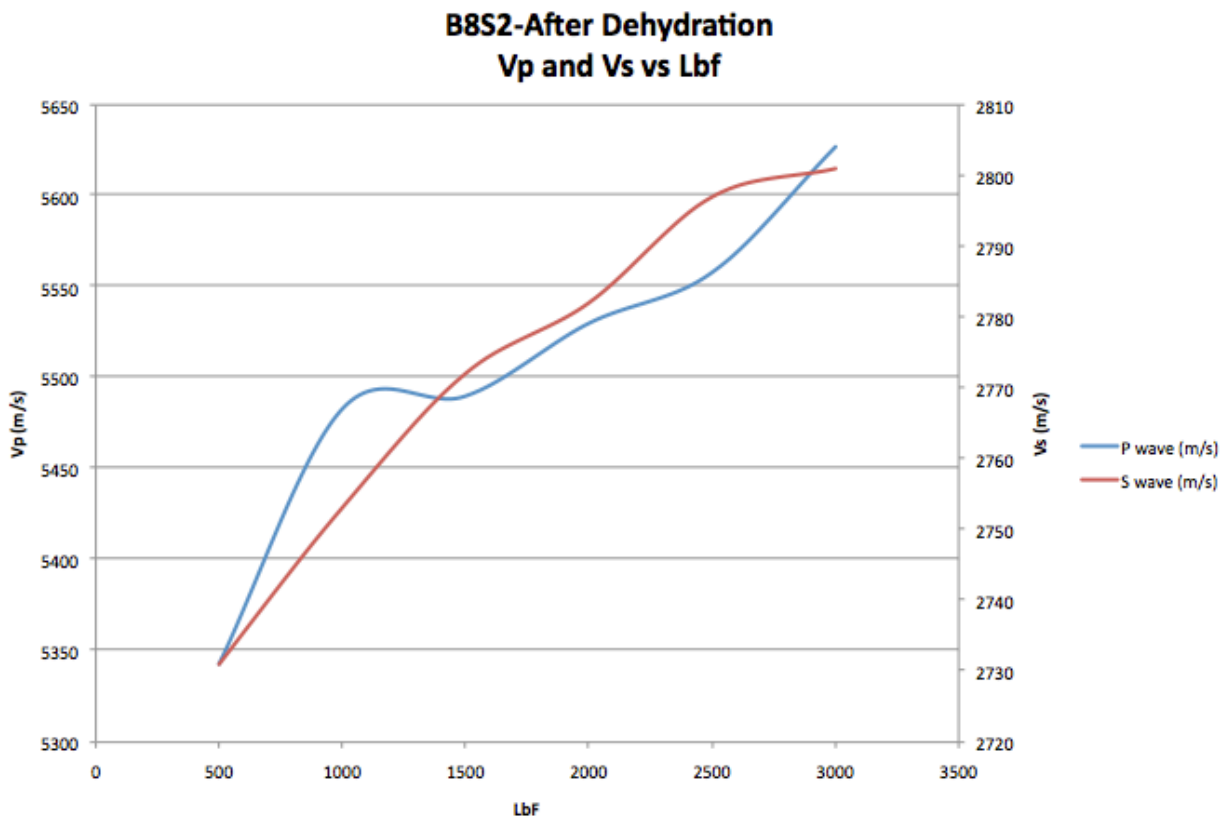


Figure 4.14 Graph comparing P-wave velocity (m/s) and S-wave velocity (m/s) to Lbf for core sample B8S2 after dehydration. Data used to construct graph in Table 4.4.

Figure 4.9 and 4.12 are showing velocity of P-wave in comparison with increasing effective stress before and after dehydration. Velocities of P-waves before dehydration are lower than the curve for post core dehydration. This is most likely due to the decrease in the presence of fluid and therefore the decrease in attenuation. However, the S-wave velocity curves exhibit a reverse characteristic. The velocities increase after dehydration, and this is due to the calculation of S-wave velocities, as seen in the following Vs equation.

$$V_p = \sqrt{\frac{K + \frac{4}{3}\mu}{\rho}}$$

$$V_s = \sqrt{\frac{\mu}{\rho}}$$

Where V_p is P-wave velocity, K is the bulk modulus, μ is the shear modulus, ρ is the density, and V_s is the S-wave velocity. So by decreasing the density of the cores from dehydration, we see an increase in S-wave velocity. Figures 4.11 and 4.14 show the change in P- and S-wave velocities in regards to a change in Lbf. There is an interesting change in wave character from before and after dehydration. However, there is a general trend of increasing wave velocity with an increase in effective pressure.

KGS Cores

4-26

Core sample 4-26 is from the deep surface core set, provided by Dr. Saugatta Datta, in collaboration with the Department of Energy in collaboration with the Kansas Geological Survey and others. This core was extracted from the Mississippian Group from the Wellington KGS 1-32 well in Sumner County, Kansas. The rest of the core data from this set are found in Appendix A. Each core has corresponding physical parameters (height,

diameter, mass, and extraction depth). These cores were not available for invasive testing, due to their role as a part of an ongoing study, so we were unable to dehydrate them to see effects of residual fluids on the elastic properties of the rocks.



Figure 4.15 KGS Core 4-26, view perpendicular to cored axis.

Figure 4.16 KGS Core 4-26, view parallel to cored axis.

Sample	Height (mm)	Diameter (mm)	Mass (g)	Density (g/mm ³)
4_26	79.3	42.3	216.8	1.95E-03

Table 4.5 Physical properties of sample 4-26.

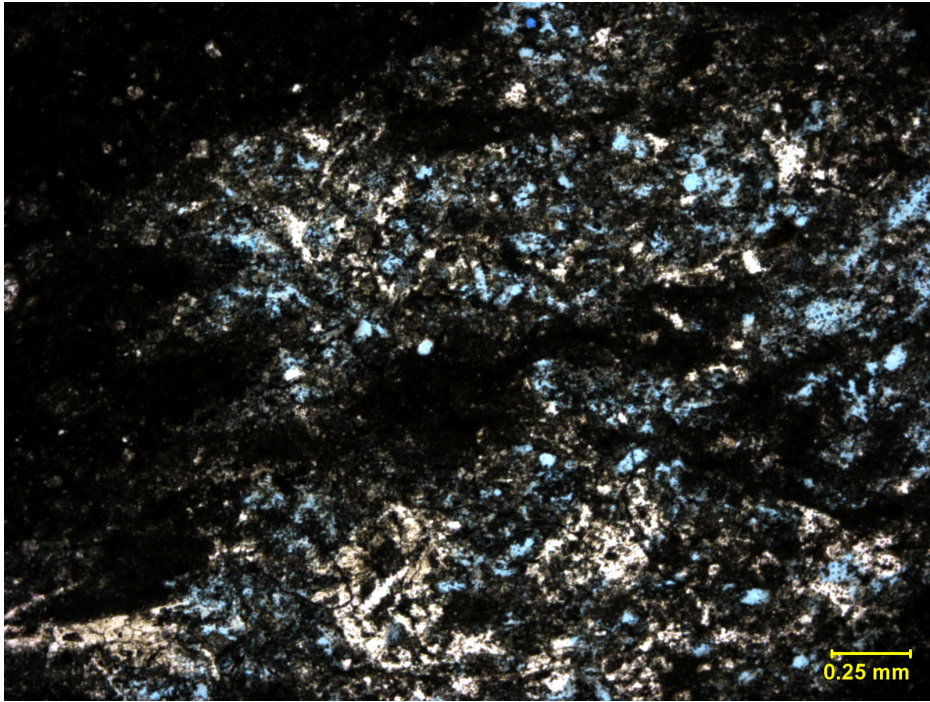


Figure 4.17 Thin section image of KGS Core sample 4-26. Image is at 4X magnification and in plane polarized light.

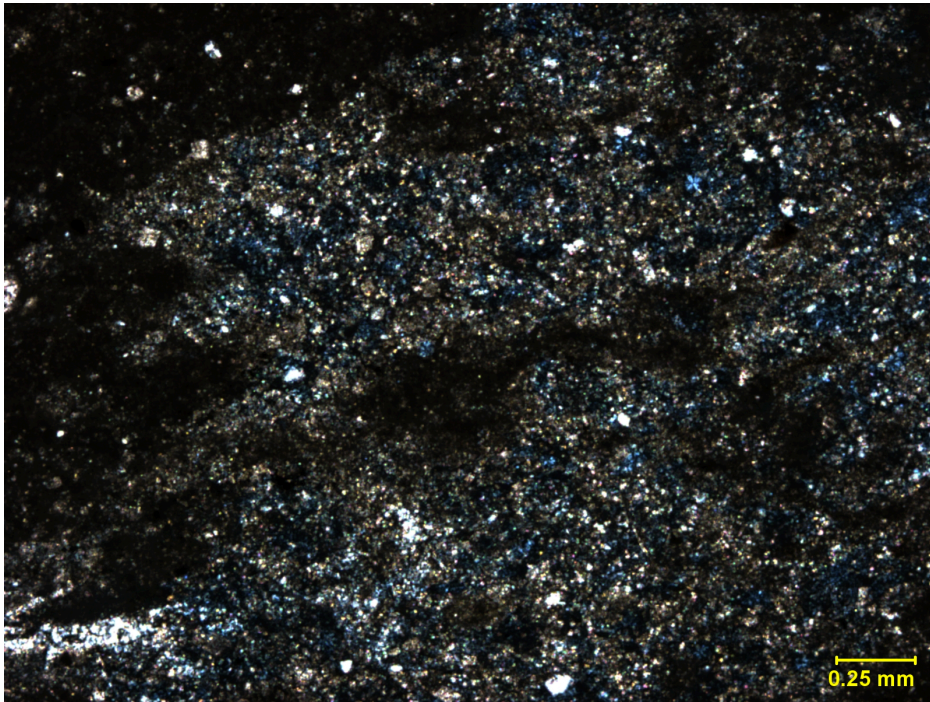


Figure 4.18 Thin section image of KGS Core sample 4-26. Image is at 4X magnification and in crossed polarized light.

From thin section analysis, sample 4-26 is primarily a finely crystalline dolomite with evidence of matrix porosity and zones of silicification. Some opaque black sulfides or oxides were seen as well as some precipitants. Throughout this thin section, there was some evidence of potential oil staining. Looking at the grains in thin section view could potentially explain variations in attenuation differences based on pore and grain architecture. Additional thin section images from the cores involved in this study can be found in Appendix A.

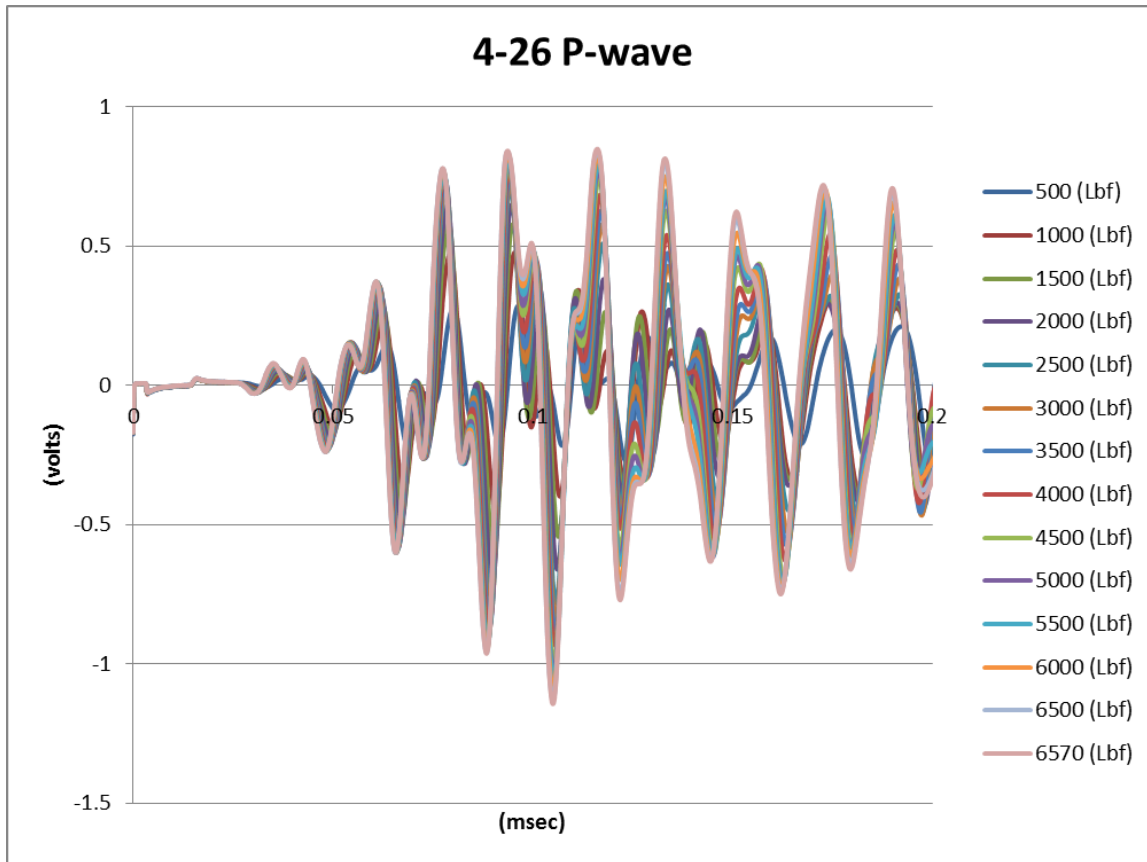


Figure 4.19 Graph of sample 4-26, P waveform stacked from 500 Lbf to 6570 Lbf, simulating near in situ conditions.

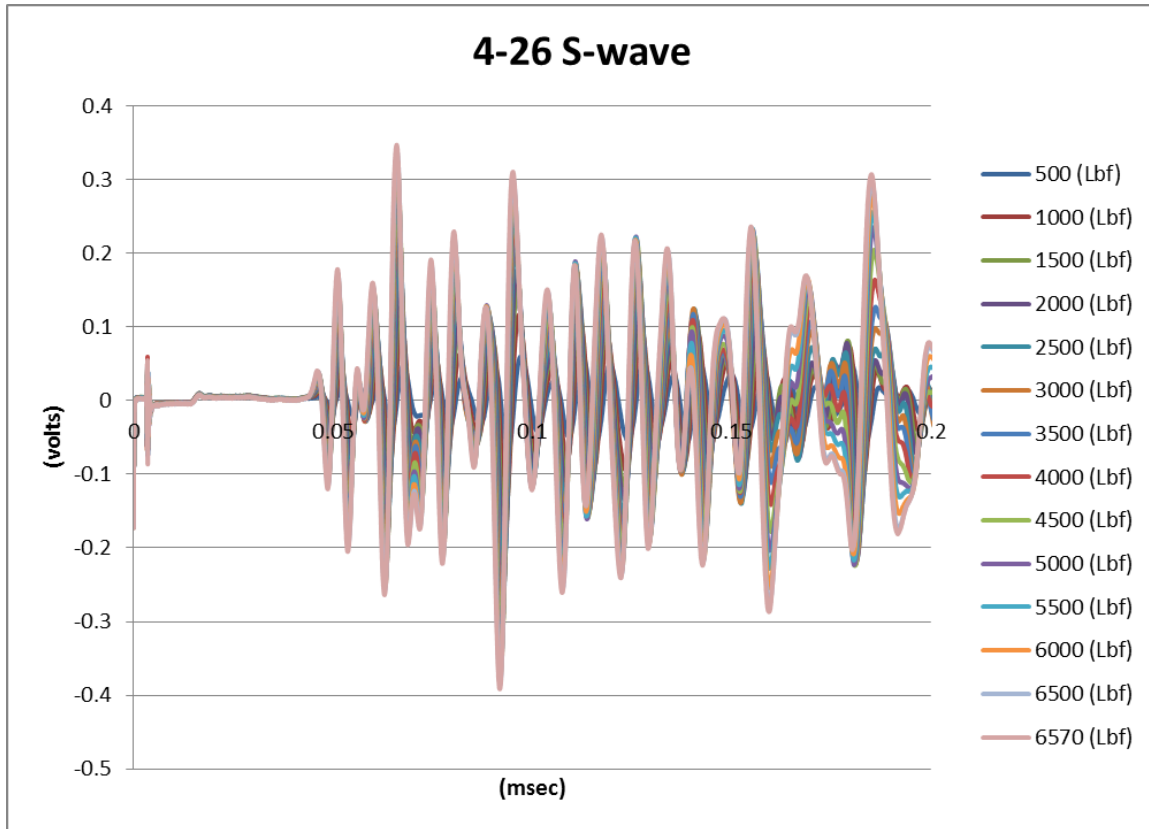


Figure 4.20 Graph of sample 4-26, S waveform stacked from 500 Lbf to 6570 Lbf, simulating near in situ conditions.

These stacked waveforms, as seen in Figures 4.19 and 4.20, give insight to the increase in amplitude and velocity with an increase in effective stress for deep surface cores. Table 4.6 show the P-wave and S-wave velocities and elastic moduli for varying effective stress for sample 4-26. Stacked waveform graphs and elastic moduli data tables for the remaining core data can be found in Appendix B.

Lbf	P wave (m/s)	S wave (m/s)	Poisson's Ratio	Young's Modulus (kPa)	Bulk Modulus (kPa)	Shear Modulus (kPa)
500	4780	2506	0.31	42643828	37482148	16271530
1000	4921	2526	0.32	43675668	40693616	16529789
1500	4987	2531	0.33	44034108	42285960	16598567
2000	5003	2536	0.33	44209056	42642476	16654880
2500	5020	2536	0.33	44260656	43078424	16654880
3000	5052	2540	0.33	44480992	43828348	16711478
3500	5173	2536	0.34	44696984	47106556	16654880
4000	5173	2557	0.34	45342560	46725336	16940794
4500	5173	2557	0.34	45342560	46725336	16940794
5000	5176	2575	0.34	45877984	46514620	17174860
5500	5198	2570	0.34	45806200	47160348	17115892
6000	5231	2579	0.34	46165648	47899484	17234140
6500	5286	2588	0.34	46572728	49260372	17346472
6570	5286	2593	0.34	46725480	49170584	17413812

Table 4.6 Velocity of P- and S-waves and elastic moduli of sample 4-26.

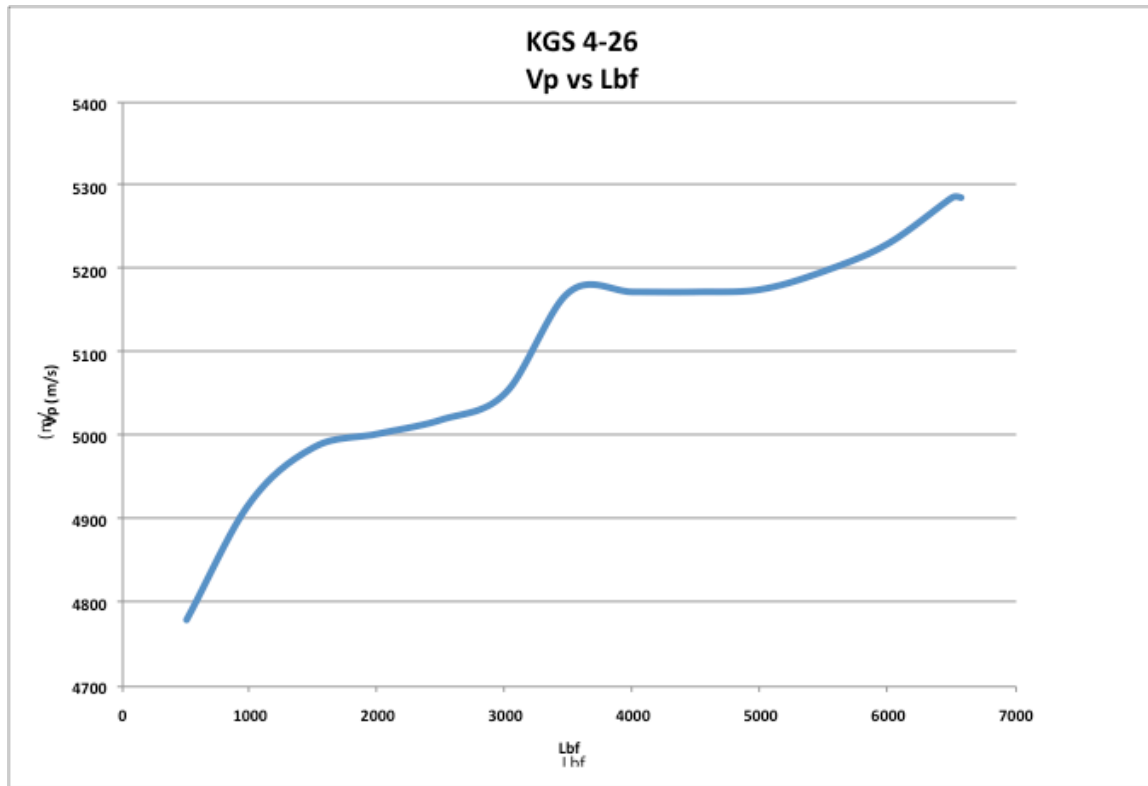


Figure 4.21 Graph comparing P-wave velocity (m/s) to increasing lbf for core sample 4-26. Data used to construct graph in Table 4.6.

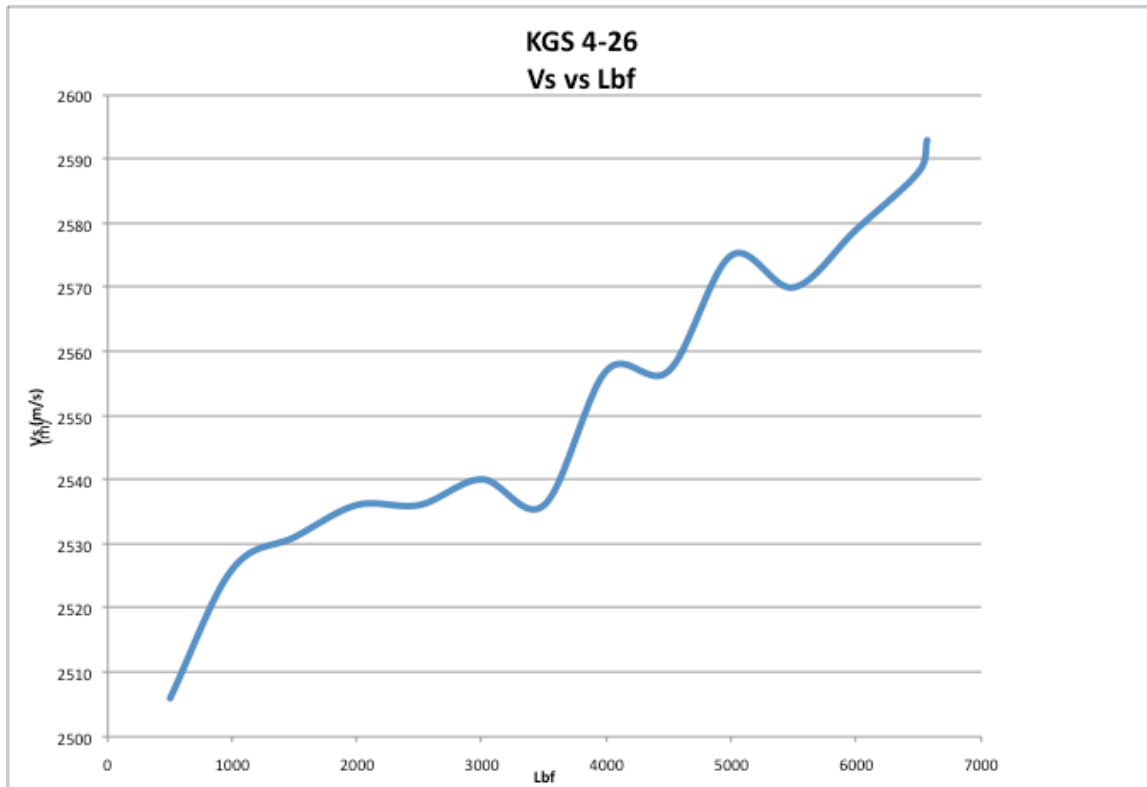


Figure 4.22 Graph comparing S-wave velocity (m/s) to increasing lbf for core sample 4-26. Data used to construct graph in Table 4.6.

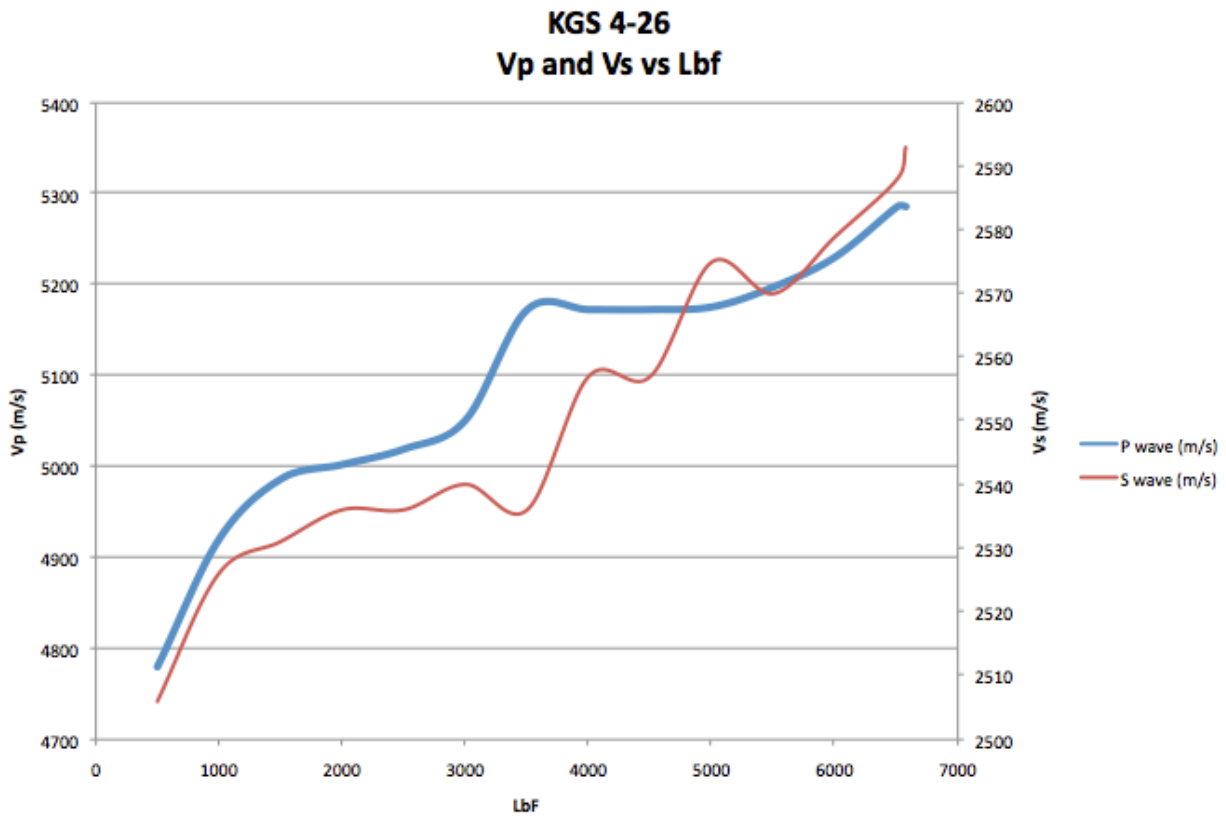


Figure 4.23 Graph comparing P-wave velocity (m/s) to S-wave velocity (m/s) for core sample 4-26. Data used to construct graph in Table 4.6.

Figures 4.21 and 4.22 show a consistency with the near surface cores in regards to an overall increase in velocity with an increase in effective stress. Figure 4.23 shows the change in P- and S-wave velocities in regards to a change in Lbf. There is a general trend of increasing wave velocity with an increase in effective pressure.

14-4

Core sample 14-4 is from the deep surface core set, provided by Dr. Saugatta Datta, in collaboration with the Department of Energy in collaboration with the Kansas Geological Survey and others. This core was extracted from the Arbuckle Group from the Wellington KGS 1-32 well in Sumner County, Kansas. The rest of the core data from this set are found

in Appendix A. Each core has corresponding physical parameters (height, diameter, mass, and extraction depth). These cores were not available for invasive testing, due to their role as a part of an ongoing study, so we were unable to dehydrate them to see effects of residual fluids on the elastic properties of the rocks.



Figure 4.24 KGS Core 14-4, view perpendicular to cored axis.

Figure 4.25 KGS Core 14-4, view parallel to cored axis.

Sample	Height (mm)	Diameter (mm)	Mass (g)	Density (g/mm ³)
14_4	56.3	42.3	155	1.96E-03

Table 4.7 Physical properties of sample 14-4.



Figure 4.26 Thin section image of KGS Core sample 14-4. Image is at 4X magnification and in plane polarized light.

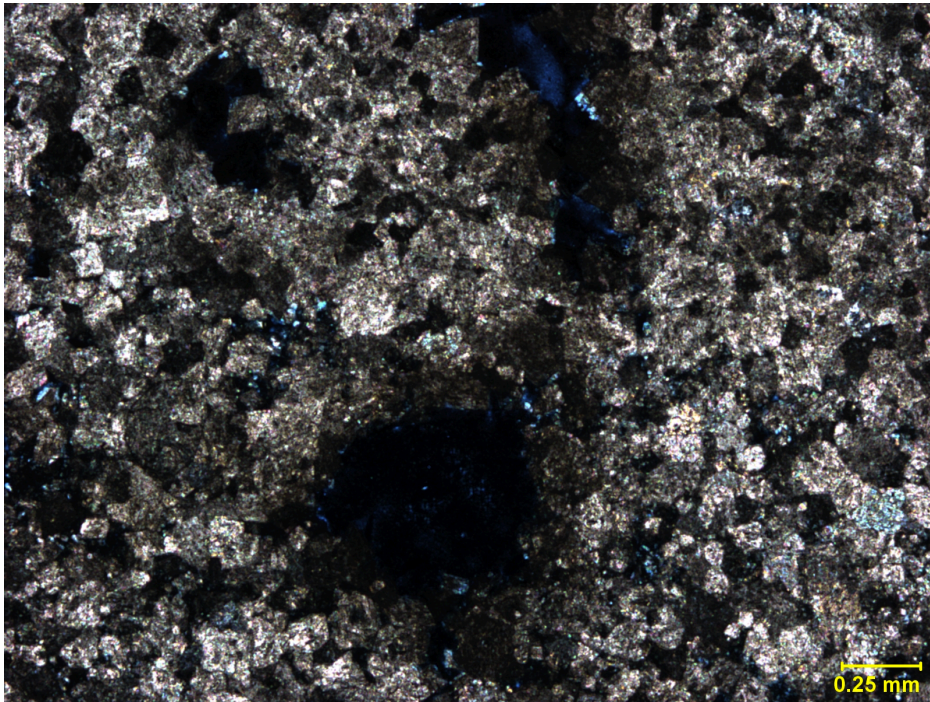


Figure 4.27 Thin section image of KGS Core sample 14-4. Image is at 4X magnification and in crossed polarized light.

Sample 14-4, as seen in thin section, is a primarily sub anhedral to anhedral dolomite, intergrown with some quartz grains. The texture ranges from fine-grained to coarsely crystalline. Porosity is inconsistent and varies from intercrystalline to vuggy. Looking at the grains in thin section view could potentially explain variations in attenuation differences based on pore and grain architecture. Additional thin section images from the cores involved in this study can be found in Appendix A.

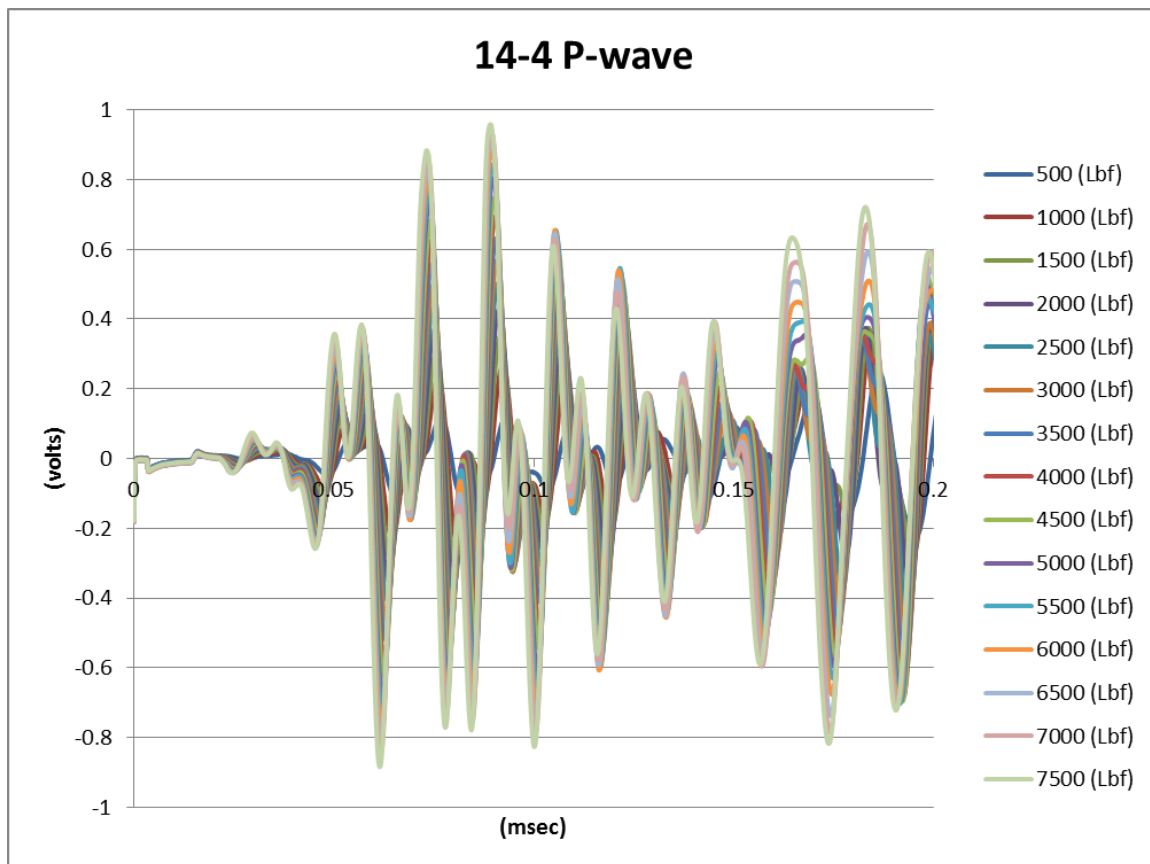


Figure 4.28 Graph of sample 14-4, P waveform stacked from 500 Lbf to 7500 Lbf, simulating near in situ conditions.

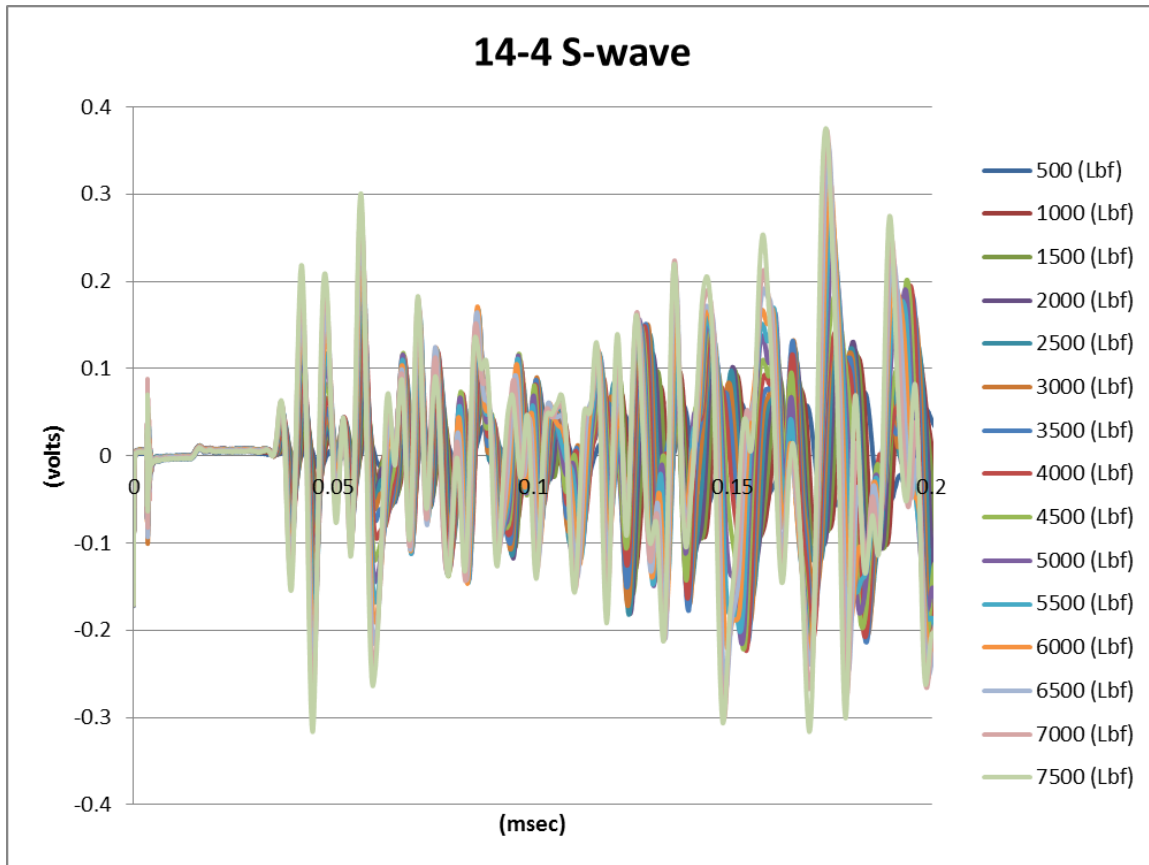


Figure 4.29 Graph of sample 14-4, S waveform stacked from 500 Lbf to 7500 Lbf, simulating near in situ conditions.

These stacked waveforms, as seen in Figures 4.28 and 4.29, give insight to the increase in amplitude and velocity with an increase in effective stress for deep surface cores. Tables 4.8 show the P-wave and S-wave velocities and elastic moduli for varying effective stress. Stacked waveform graphs and elastic moduli data tables for the remaining core data can be found in Appendix B.

Lbf	P wave (m/s)	S wave (m/s)	Poisson's Ratio	Young's Modulus (kPa)	Bulk Modulus (kPa)	Shear Modulus (kPa)
500	4604	2705	0.24	48441324	30640116	19588020
1000	4667	2757	0.23	50144476	31163378	20353824
1500	4796	2792	0.24	51922204	33751576	20875666
2000	4910	2839	0.25	53886428	35775836	21572474
2500	4933	2846	0.25	54234980	36243844	21683560
3000	4943	2870	0.25	54932480	36007284	22048230
3500	5054	2886	0.26	56096556	38646236	22294568
4000	5154	2870	0.28	56238432	41723048	22048230
4500	5206	2902	0.27	57472120	42497360	22545070
5000	5232	2910	0.28	57861384	43062980	22671906
5500	5259	2918	0.28	58254084	43638404	22799814
6000	5396	2936	0.29	59489056	47199324	23058904
6500	5424	2943	0.29	59893260	47842688	23190110
7000	5424	2943	0.29	59893260	47842688	23190110
7500	5453	2943	0.29	60035880	48673952	23190110

Table 4.8 Velocity of P- and S-waves and elastic moduli of sample 14-4.

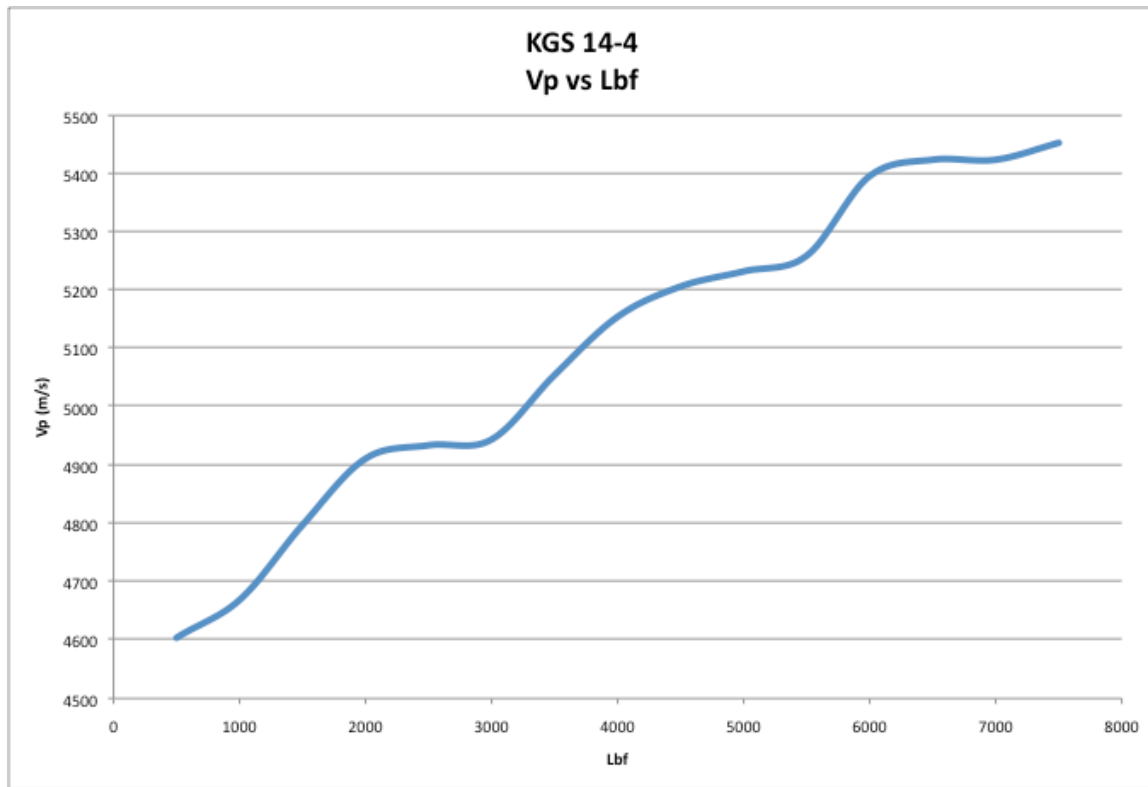


Figure 4.30 Graph comparing P-wave velocity (m/s) to increasing lbf for core sample 14-4. Data used to construct graph in Table 4.8.

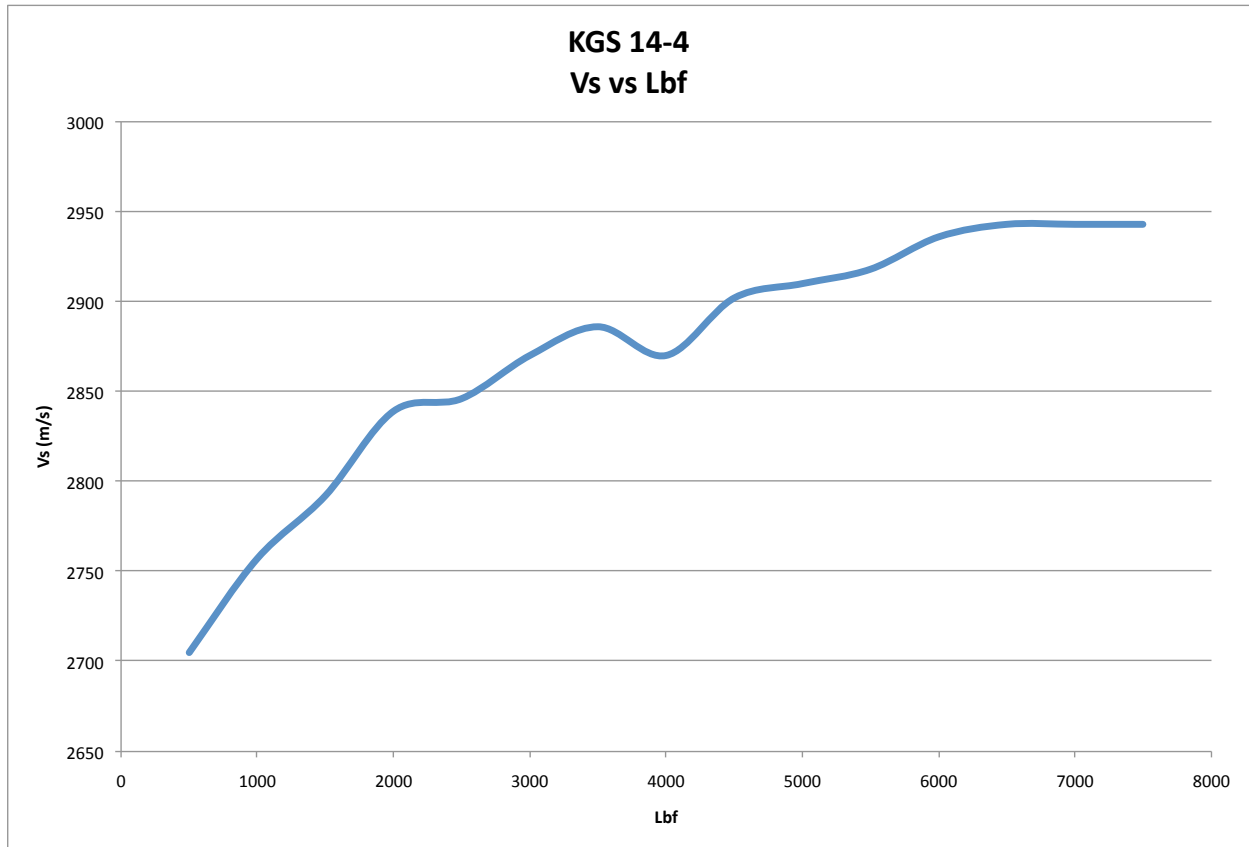


Figure 4.31 Graph comparing S-wave velocity (m/s) to increasing lbf for core sample 14-4. Data used to construct graph in Table 4.8.

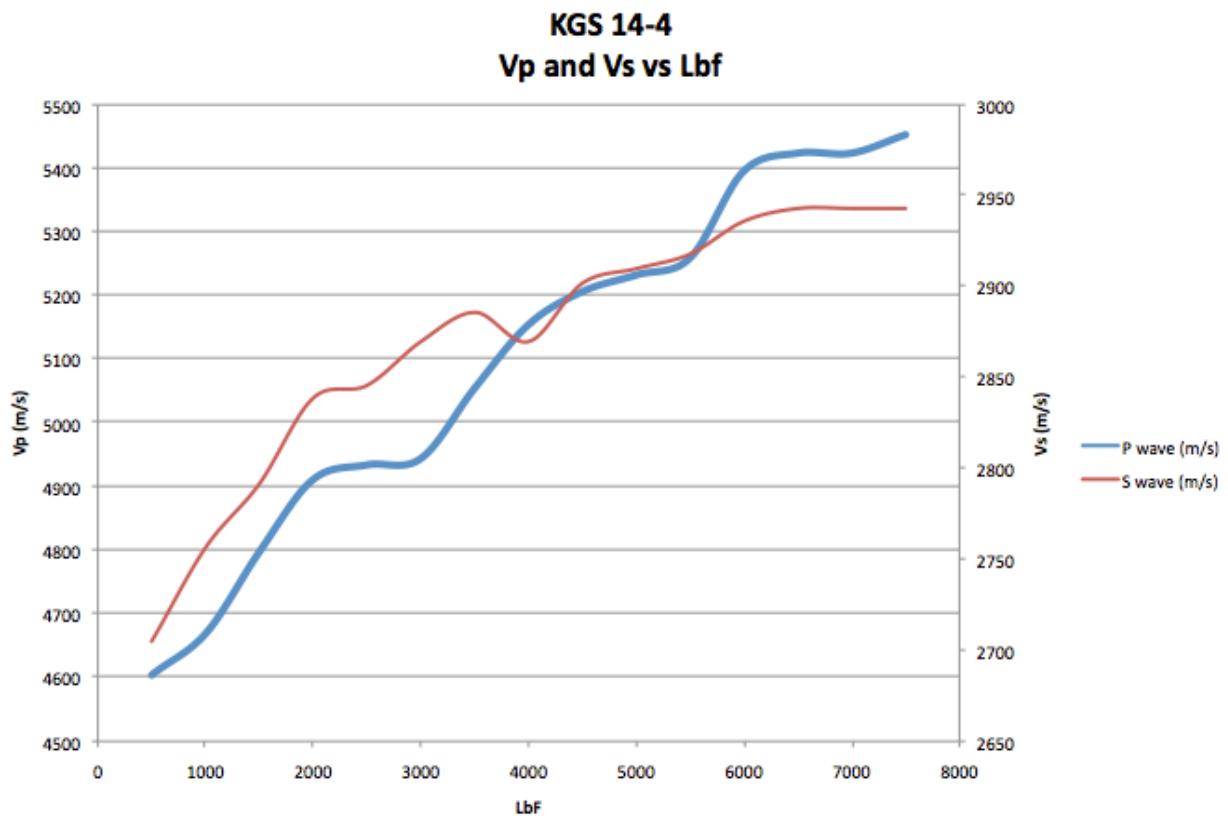


Figure 4.32 Graph comparing P-wave velocity (m/s) and S-wave velocity (m/s) to Lbf for core sample 14-4. Data used to construct graph in Table 4.8.

Figures 4.21 and 4.22 show a consistency with the near surface cores in regards to an overall increase in velocity with an increase in effective stress. Figure 4.32 shows the change in P- and S-wave velocities in regards to a change in Lbf. There is a general trend of increasing wave velocity with an increase in effective pressure.

25-3

Core sample 25-3 is from the deep surface core set, provided by Dr. Saugatta Datta, in collaboration with the Department of Energy in collaboration with the Kansas Geological Survey and others. This core was extracted from the Arbuckle Group from the Wellington KGS 1-32 well in Sumner County, Kansas. The rest of the core data from this set are found

in Appendix A. Each core has corresponding physical parameters (height, diameter, mass, and extraction depth). These cores were not available for invasive testing, due to their role as a part of an ongoing study, so we were unable to dehydrate them to see effects of residual fluids on the elastic properties of the rocks.



Figure 4.33 KGS Core 25-3, view perpendicular to cored axis.

Figure 4.34 KGS Core 25-3, view parallel to cored axis.

Sample	Height (mm)	Diameter (mm)	Mass (g)	Density (g/mm ³)
25_3	55.8	42.2	155.1	1.99E-03

Table 4.9 Physical properties of sample 25-3.

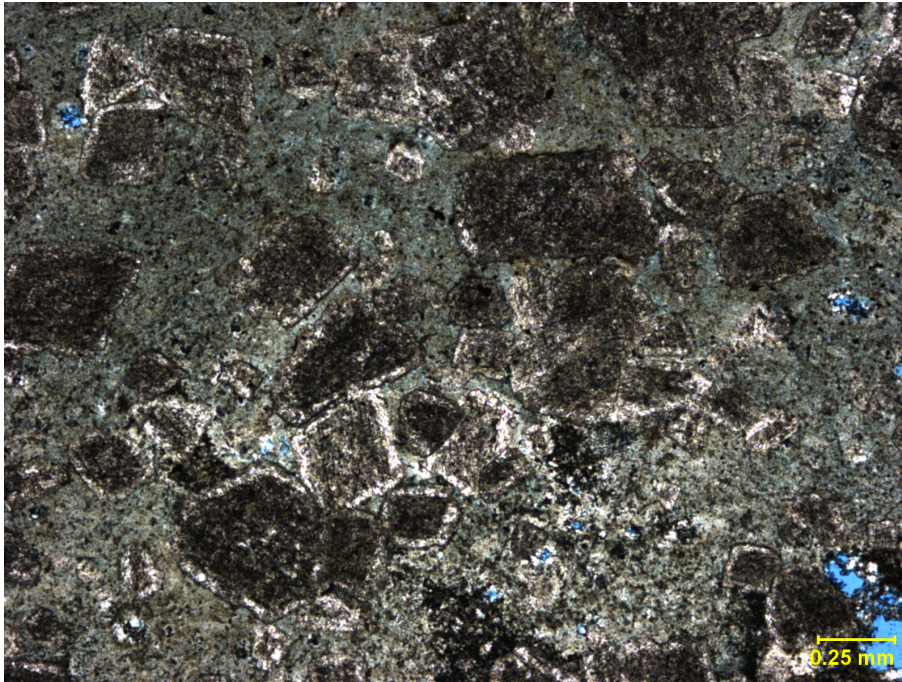


Figure 4.35 Thin section image of KGS Core sample 25-3. Image is at 4X magnification and in plane polarized light.

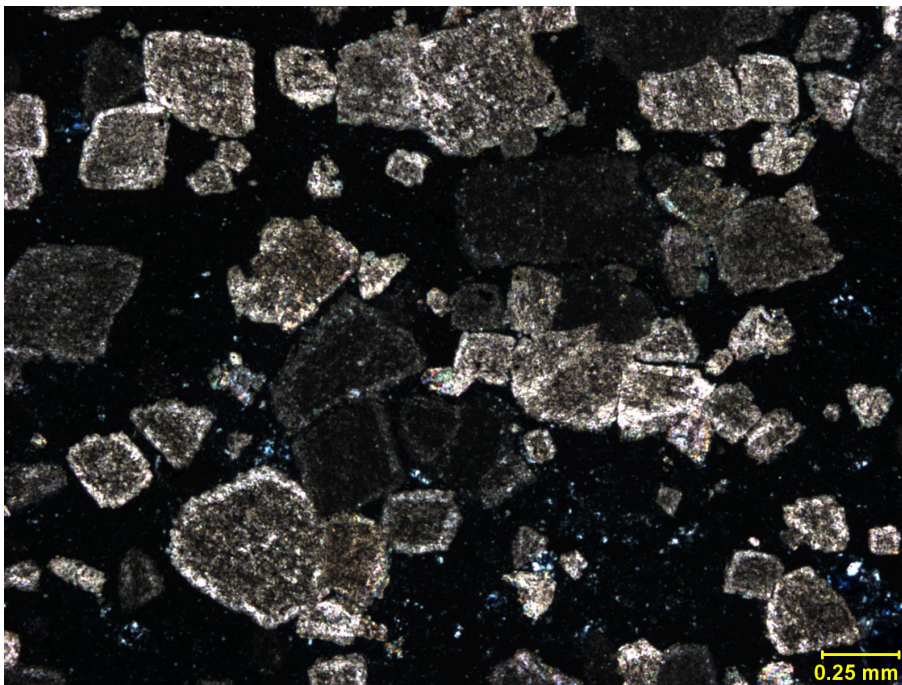


Figure 4.36 Thin section image of KGS Core sample 25-3. Image is at 4X magnification and in crossed polarized light.

Observation from thin section indicates that sample 25-3 is a sub euhedral to euhedral dolomite. The dolomite rhombohedras have darker centers with lighter rims. It also contains some oxides, zones with opaque oxide precipitants, intergranular fill, minor clay filled fractures, and silica growth within pore space. This core also shows variable porosity. Looking at the grains in thin section view could potentially explain variations in attenuation differences based on pore and grain architecture. Additional thin section images from the cores involved in this study can be found in Appendix A.

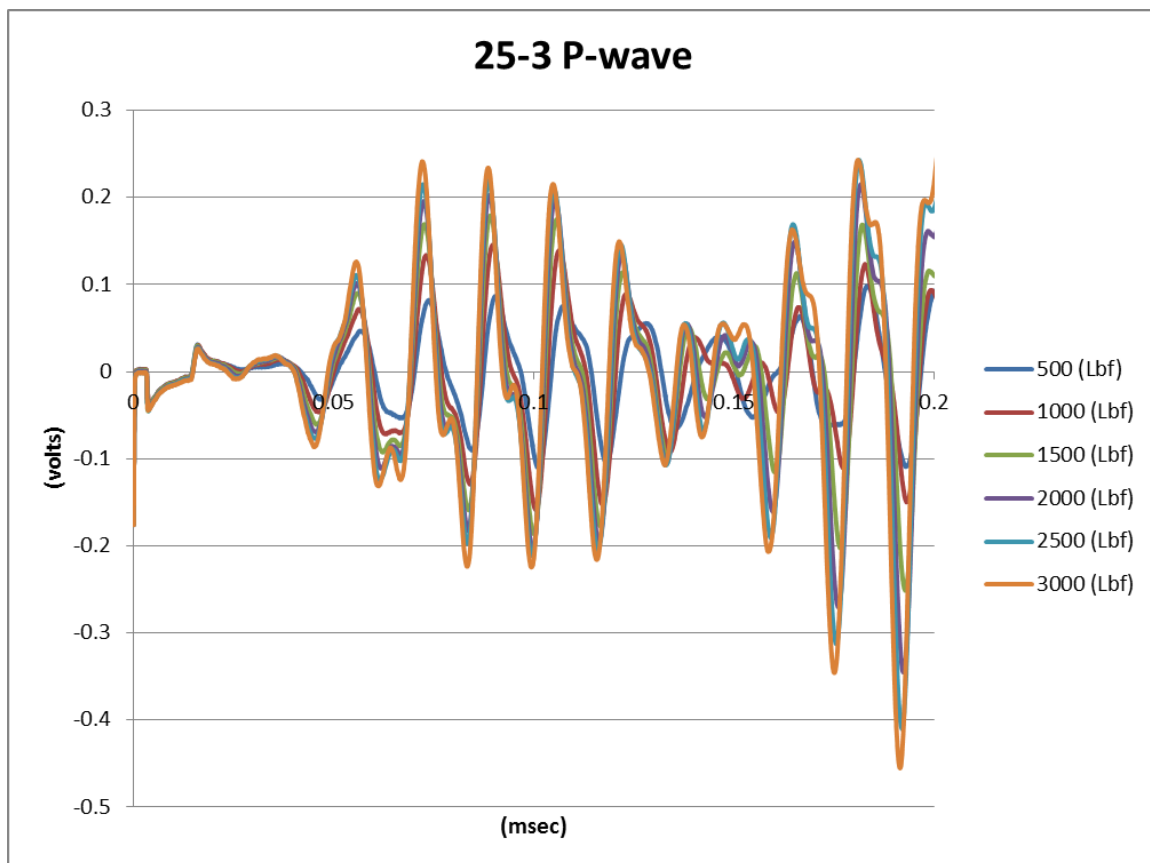


Figure 4.37 Graph of sample 25-3, P wave stacked from 500 Lbf to 3000 Lbf.

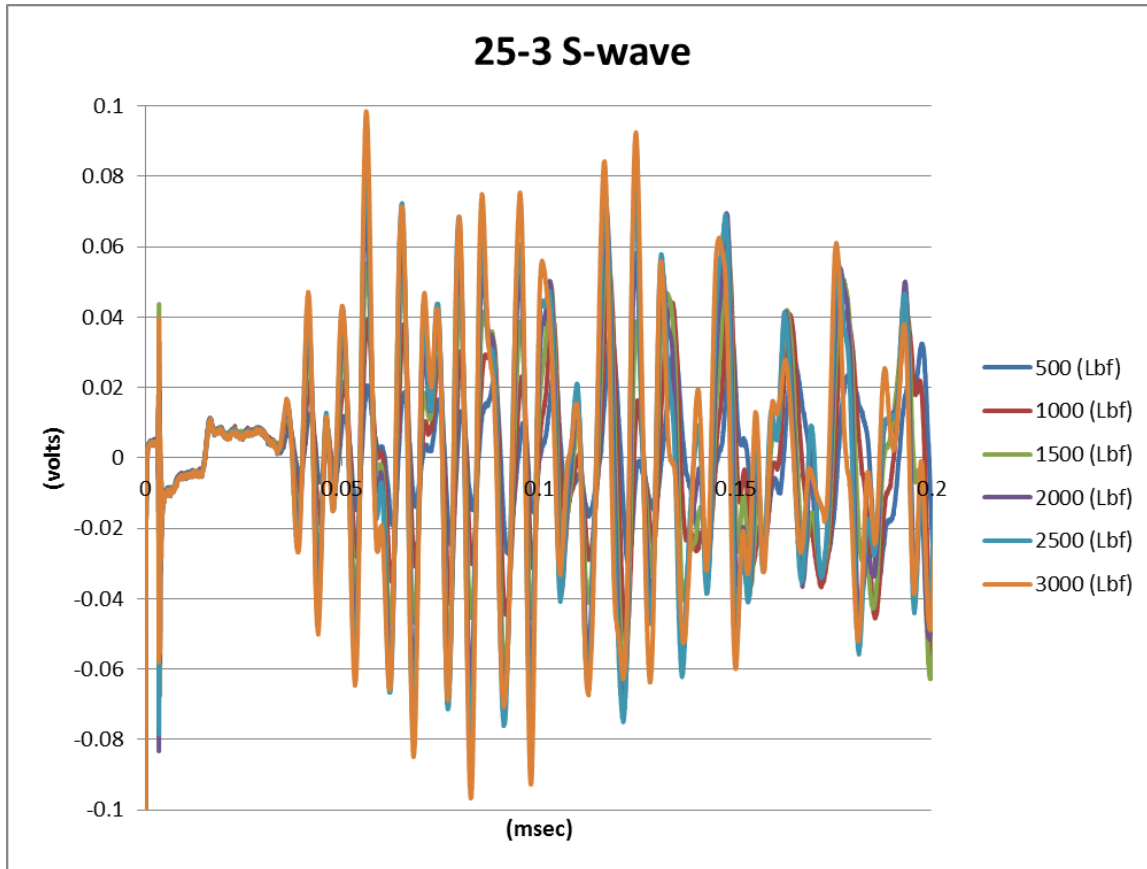


Figure 4.38 Graph of sample 25-3, S waveform stacked from 500 Lbf to 3000 Lbf.

These stacked waveforms, as seen in Figures 4.37 and 4.38, give insight to the increase in attenuation and velocity with an increase in effective stress for deep surface cores. Tables 4.10 show the P-wave and S-wave velocities and elastic moduli for varying effective stress. Stacked waveform graphs and elastic moduli data tables for the remaining core data can be found in Appendix B.

Lbf	P wave (m/s)	S wave (m/s)	Poisson's Ratio	Young's Modulus (kPa)	Bulk Modulus (kPa)	Shear Modulus (kPa)
500	5026	2886	0.25	41508384	28130270	16549463
1000	5125	2925	0.26	42788416	29535282	16999144
1500	5217	2961	0.26	43990940	30853176	17424032
2000	5293	2936	0.28	43768604	32847282	17124956
2500	5355	2961	0.28	44596572	33745892	17424032
3000	5469	2961	0.29	45046220	36207232	17424032

Table 4.10 Velocity of P- and S-waves and elastic moduli of sample 25-3.

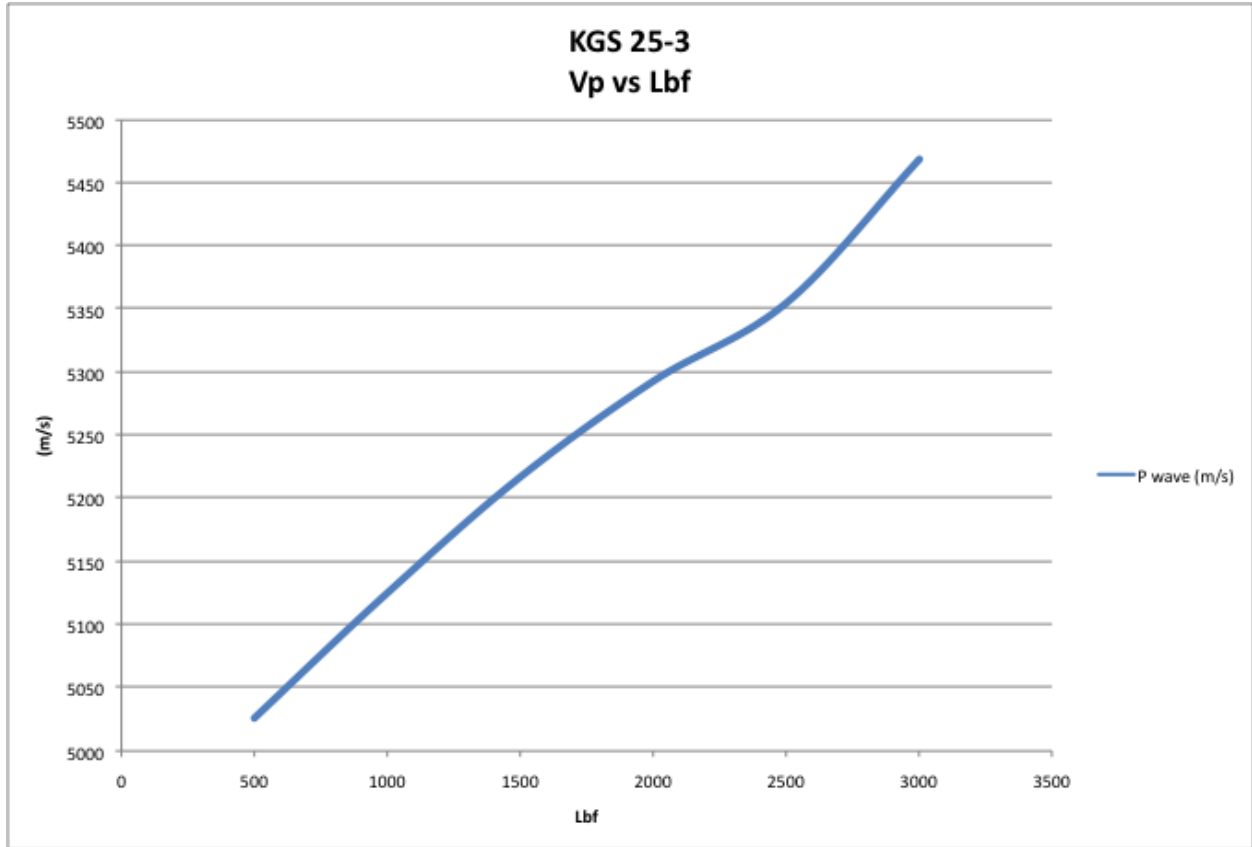


Figure 4.39 Graph comparing P-wave velocity (m/s) to increasing lbf for core sample 25-3. Data used to construct graph in Table 4.10.

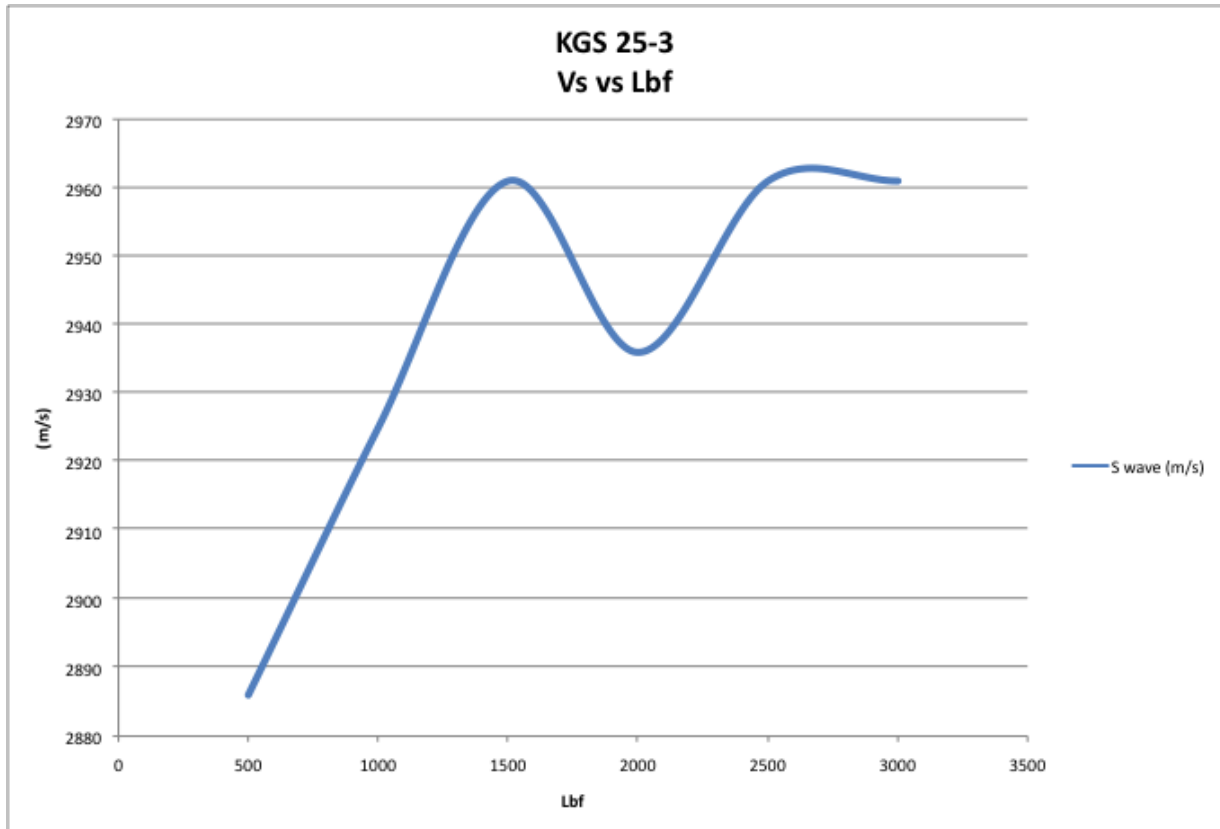


Figure 4.40 Graph comparing S-wave velocity (m/s) to increasing lbf for core sample 25-3. Data used to construct graph in Table 4.10.

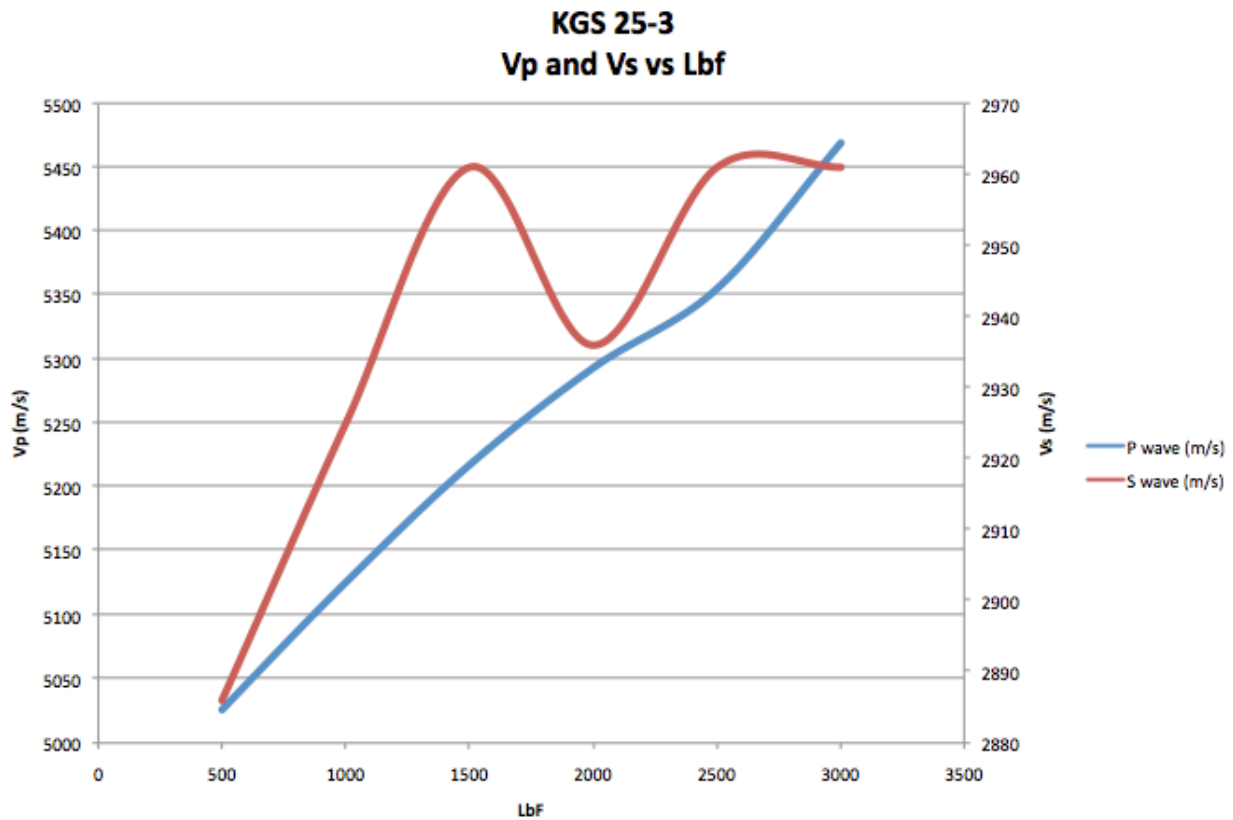


Figure 4.41 Graph comparing P-wave velocity (m/s) and S-wave velocity (m/s) to Lbf for core sample 25-3. Data used to construct graph in Table 4.10.

Figure 4.41 shows the change in P- and S-wave velocities in regards to a change in Lbf. There is a general trend of increasing wave velocity with an increase in effective pressure.

After analysis of the velocity graphs, the inconsistency in the graph pattern could be due to creation and closure of micro cracks within the core. Further research needs to be completed to verify if this is in fact the case, but if so, there is potential applications for fracture monitoring. Additional images of core samples and thin sections can be found in Appendix A, and waveform and elastic moduli data can be found in Appendix B.

Amplitude Variations and Attenuation

Each core sample exhibited an amplitude increase with an increase of pressure. This amplitude variation can potentially be used in time-lapse monitoring from amplitude response. The effective pressure is equal to the overburden pressure minus the pore pressure. When monitoring a given reservoir for a specific type of event, there should be a predictable pressure scenario. The pressure scenario should also be in cohesion with the amplitude response. During CO₂ sequestration monitoring, pore pressure would increase. With the increase in pore pressure, there would be a decrease in effective pressure. This could potentially translate into a decrease in amplitude. However, if there were a leak of CO₂, then this might create an increase in amplitude response. Similarly, after well log velocities are acquired, they should respond in a predictable way. Velocity and amplitude variations could play a role in the feasibility of using time lapse seismic monitoring for CO₂ sequestration.

$$A_c = A_o e^{-\alpha x}$$

Where A_c is the peak amplitude of the core's waveform, A_o is the initial peak amplitude from the face-to-face test, and x is the length of the sample (in meters). From the integration of this data, we can solve for α , which is the attenuation coefficient.

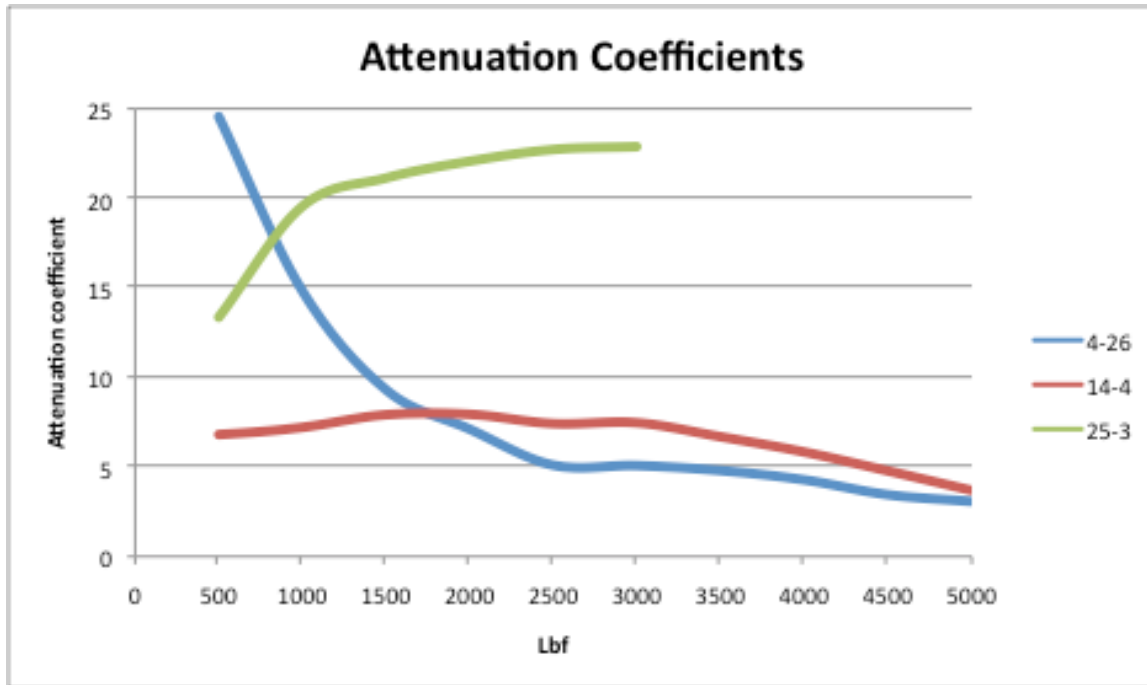


Figure 4.42 Attenuation coefficients for the Wellington oil field site.

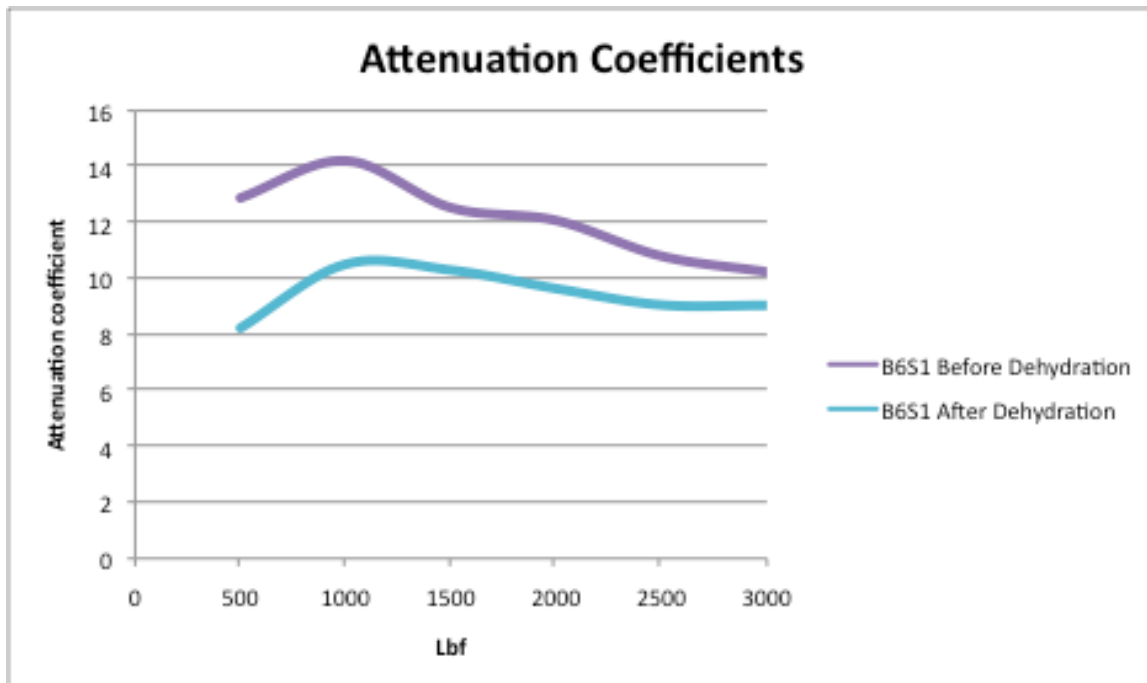


Figure 4.43 Attenuation coefficients for sample B6S1, before and after dehydration.

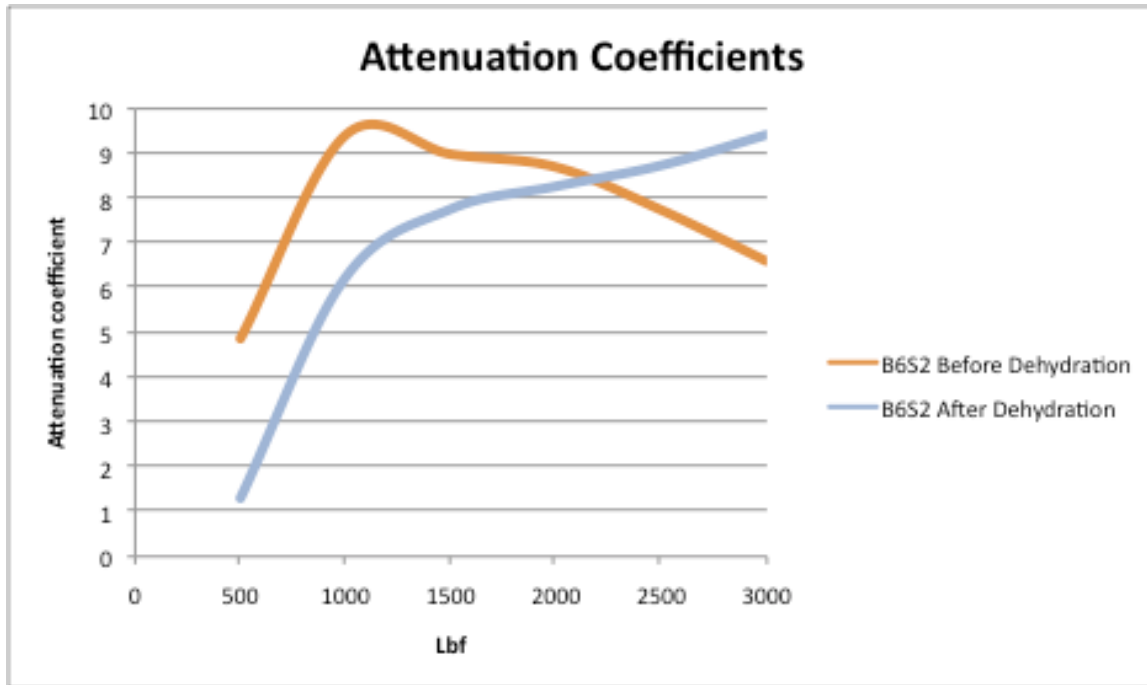


Figure 4.44 Attenuation coefficients for sample B6S2, before and after dehydration.

As seen in Figures 4.43 and 4.44, after dehydration, there is a decrease in the attenuation coefficient. The fluid reduction subsequently lowers the attenuation. Also, when looking at the difference in the attenuation curves compared to thin section properties, it can be suggested that the difference in curve character could be based on a difference in crystalline texture. More research is necessary to thoroughly understand these effects and influences of pore and grain architecture. This difference could be potentially due to the difference between grain supported and matrix supported rock, with an influence from compliant versus stiff cracks. Attenuation of waves can, however, be an important factor in reservoir characterization.

Comparison of In Situ and Laboratory Velocities

Well log at Sonic Frequency			
Sample	Depth (ft)	P wave (m/s)	S wave (m/s)
4_26	3717.9	4986.09521	2911.45286
14_4	4247	5208.47573	2989.70083

Table 4.11 P- and S-wave velocities from well logs at sonic frequencies.

Laboratory at Ultrasonic Frequency			
Sample	Lbf	P wave (m/s)	S wave (m/s)
4_26	6570	5286	2593
14_4	7070	5453	2943

Table 4.12 P- and S-wave velocities from laboratory data at ultrasonic frequencies.

Sonic and dipole sonic velocities were acquired from well log data, as seen in Figures 4.46, 4.48, and 4.50. These velocities were then input into Gassmann’s fluid replacement modeling scenarios for cores 4-26 and 14-4, and were representative of the Mississippian and Arbuckle respectively.

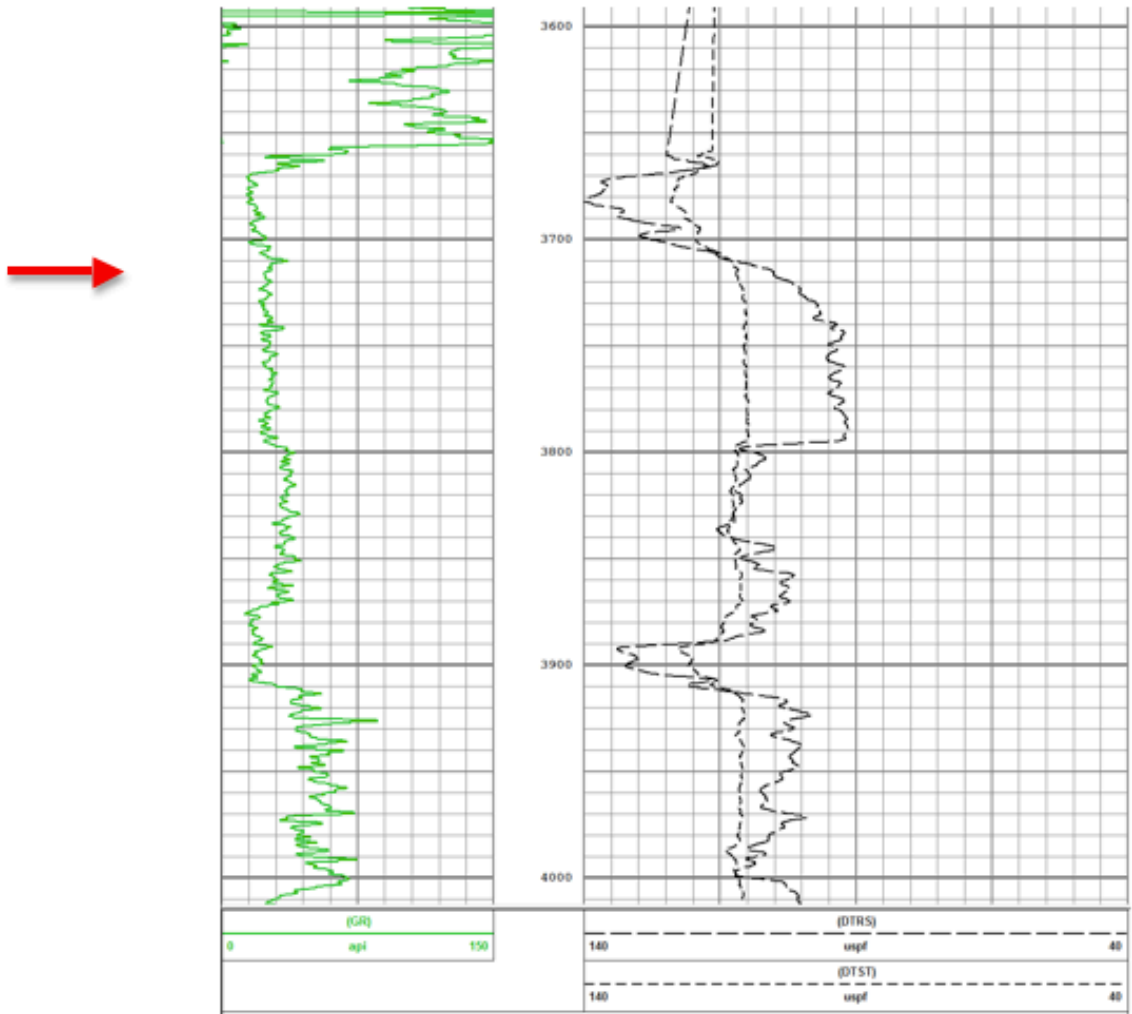


Figure 4.45 Well log interval for sample 4-26 at 3717 ft (indicated by red arrow) showing gamma ray (green curve) and sonic and dipole sonic logs (black curves).

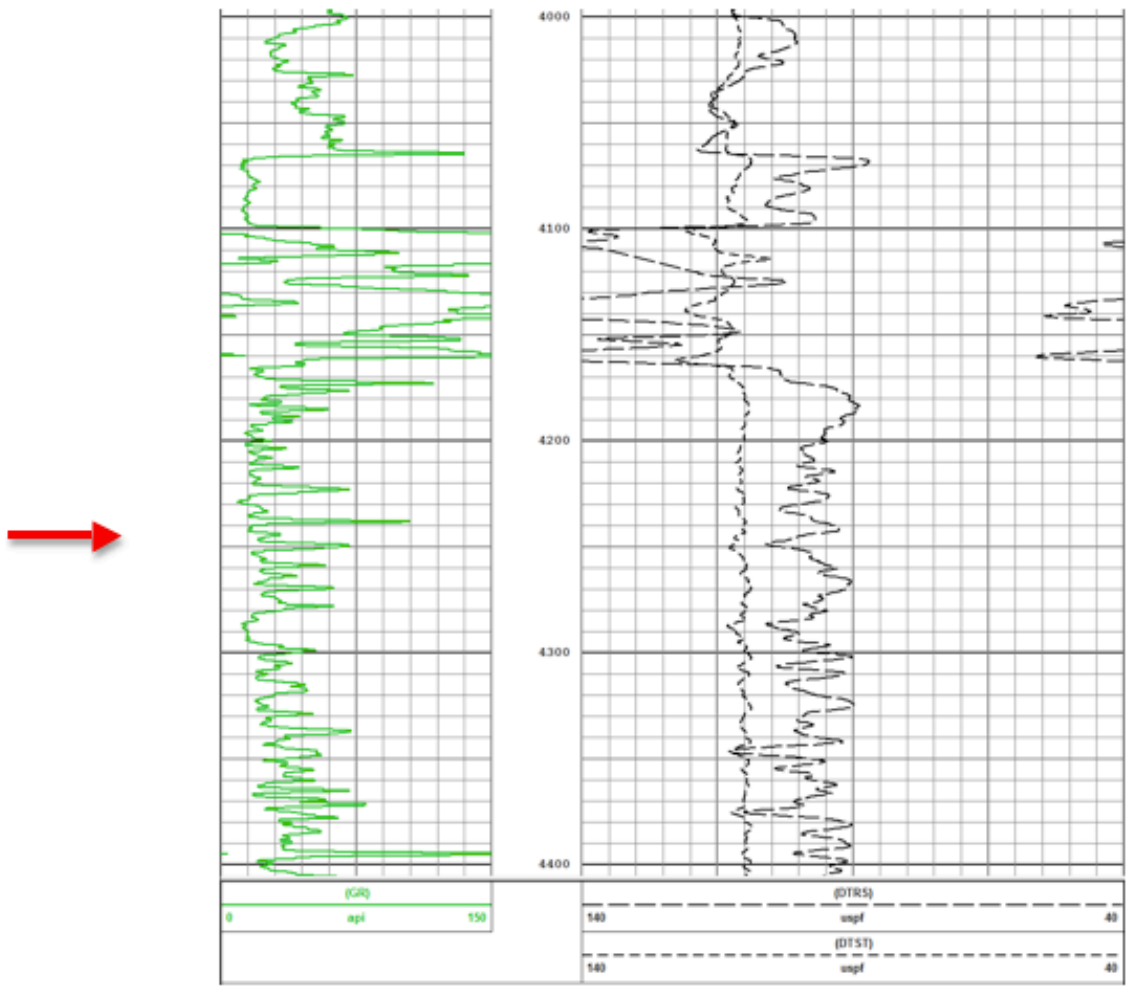


Figure 4.46 Well log interval for sample 14-4 at 4247 ft (indicated by red arrow) showing gamma ray (green curve) and sonic and dipole sonic logs (black curves).

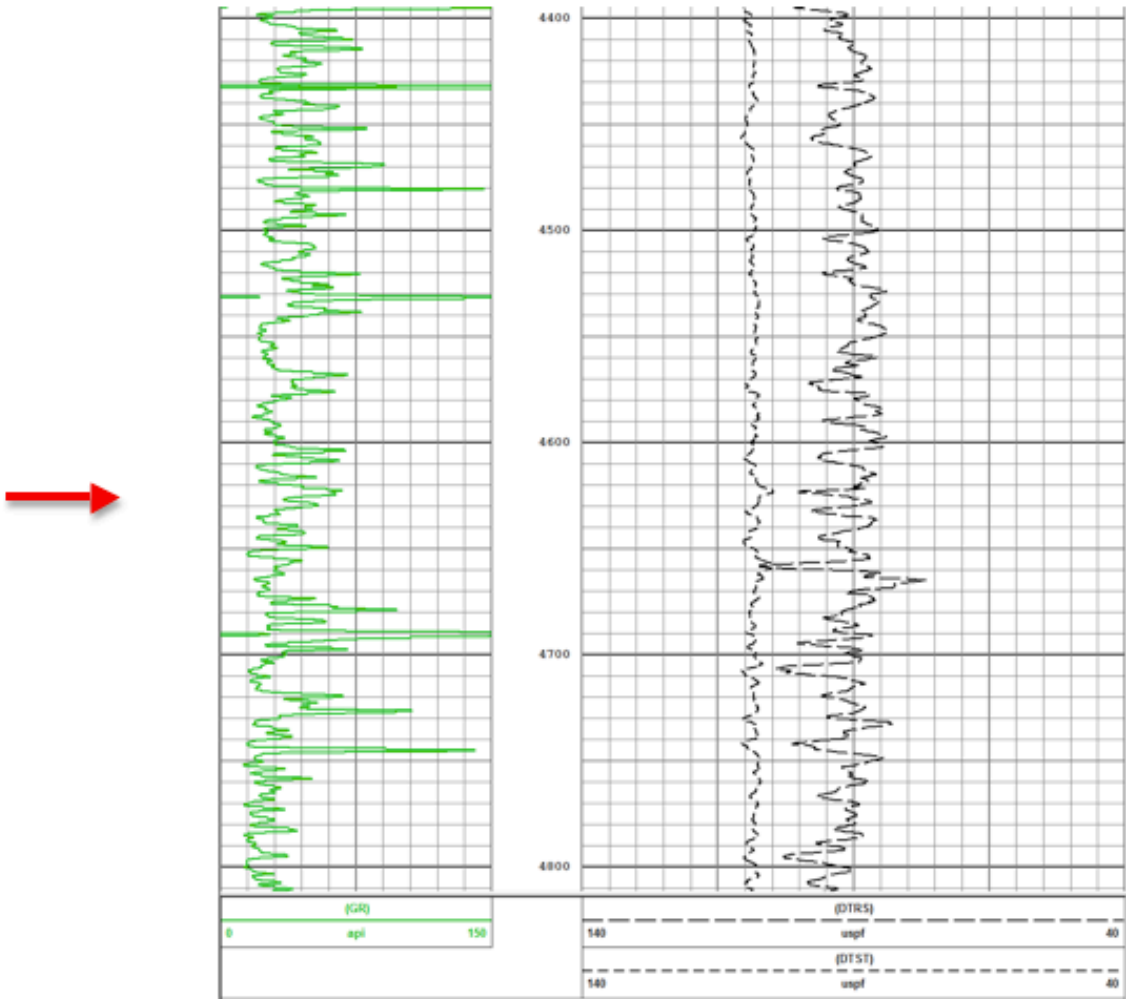


Figure 4.47 Well log interval for sample 25-3 at 4626 ft (indicated by red arrow) showing gamma ray (green curve) and sonic and dipole sonic logs (black curves).

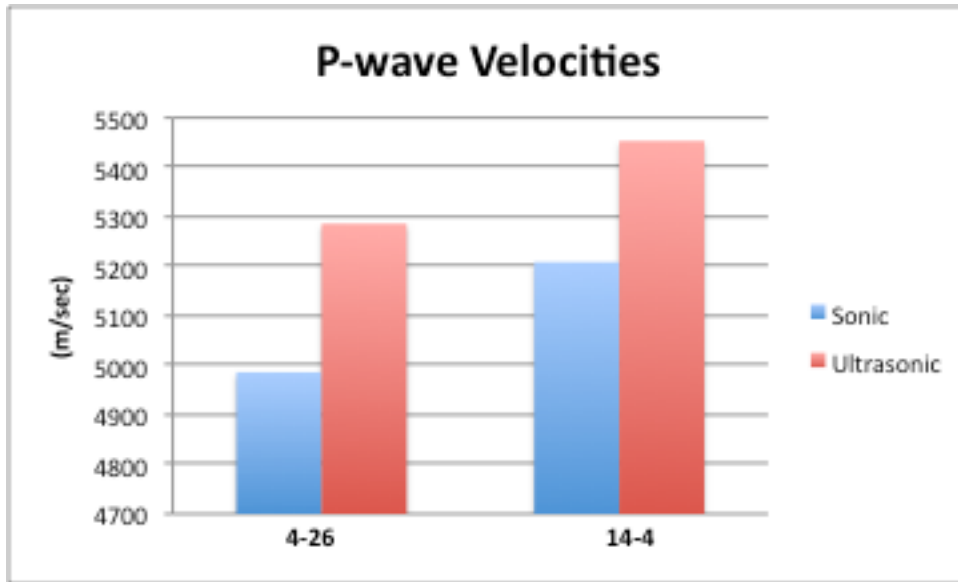


Figure 4.48 Comparison of P-wave velocities at sonic and ultrasonic frequencies obtained from well logs and laboratory measurements (see Tables 4.11 and 4.12).

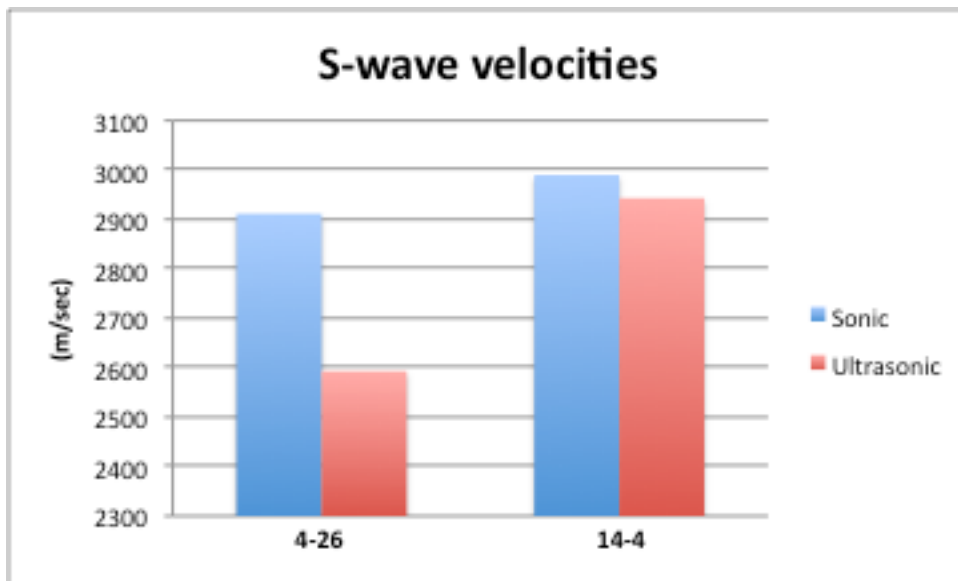


Figure 4.49 Comparison of S-wave velocities at sonic and ultrasonic frequencies obtained from well logs and laboratory measurements (see Tables 4.11 and 4.12).

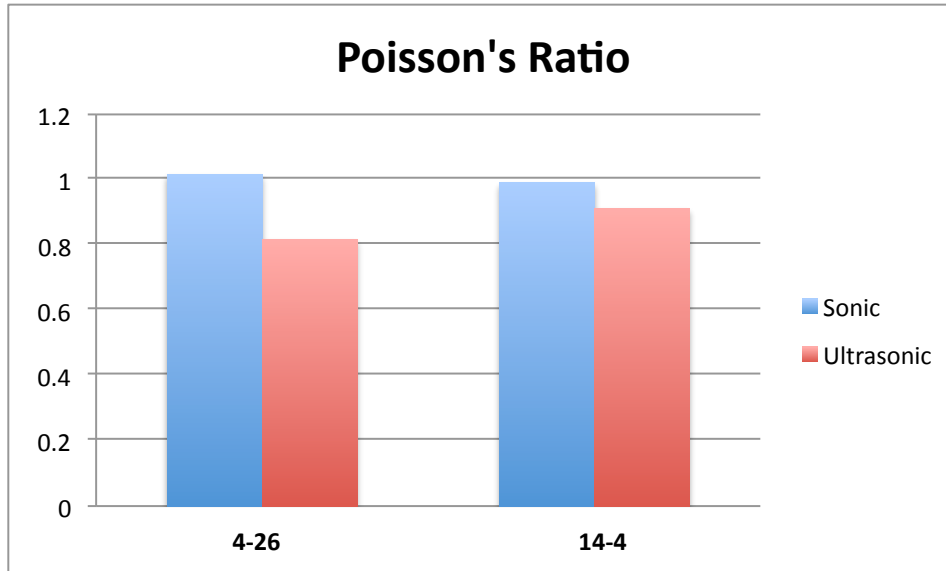


Figure 4.50 Comparison of Poisson's Ratio at sonic and ultrasonic frequencies.

When comparing P-wave velocities at sonic and ultrasonic frequencies, as seen in Figure 4.48, we see that, for these cores, velocities from ultrasonic data yielded higher values than at sonic frequencies. Also, the shift in velocity difference was relatively comparable. However, the comparison for S-wave velocities, as seen in Figure 4.49, resulted in lower velocities from ultrasonic frequencies. The difference in velocities for S-waves was more erratic and less similar. So the next step we took was comparing Poisson's ratio at the different frequencies, as seen in Figure 4.50. Poisson's ratio can be seen in the following equation.

$$\sigma = (\alpha^2 - 2\beta^2) / (2(\alpha^2 - \beta^2))$$

Where σ is Poisson's ratio, α is velocity of P-waves and β is the velocity of S-waves. So with substantial core data, there could be potential in calibrating a relationship to determine S-wave velocities where dipole log data is lacking.

Gassmann Modeling

From using the interactive Excel spreadsheet we were able to generate predicted velocities of P- and S-waves, density, bulk modulus and Poisson's ratio in a given medium with variation in CO₂ saturations. Gassmann's relations in terms of P-wave velocity, bulk modulus, shear modulus, density, and porosity can be seen in the following equations.

$$(V_p)_{sat}^2 = \frac{K_p + K_{dry} + \frac{4}{3}\mu}{\rho_{sat}}$$

$$K_{sat} = K^* + \frac{\left(1 - \frac{K^*}{K_o}\right)^2}{\frac{\Phi}{K_{fl}} + \frac{(1 - \Phi)}{K_o} - \frac{K^*}{(K_o)^2}}$$

Where V_p is P-wave velocity, V_s is S-wave velocity, K is bulk modulus, μ is shear modulus, ρ is density, K_{sat} is saturated bulk modulus, K_o is the bulk modulus of mineral matrix, K_{fl} is bulk modulus of pore fluid, K^* is bulk modulus of porous rock frame, and Φ is porosity. Equations are from Murphy et al. (1991) and Mavko et al. (2009), respectively.

We ran both theoretical and two deep surface core scenarios for Gassmann modeling. The outcome of Gassmann's relation proves that fluids, due to their lack of rigidity, do not affect V_s on the first order of magnitude. For the theoretical modeling, I ran

four different scenarios including sandstone and limestone with both super-critical and sub-critical CO₂ at various saturations. Figures 4.51, 4.52, 4.53, and 4.54 are the graphical representation of the results. Based on interpretation of the graphs, the greatest difference within a rock type is that P-wave velocities in the limestone are more dependent on porosity than the sandstone. The theoretical modeling suggests that the velocity of the P waves decreases with increased porosity in each rock type due to the additional pore space present in the rock matrix. Limestone has a larger variation of pore spaces than sandstone. While Gassmann's equation is best applied to siliciclastic rocks, the equation is still applicable for carbonates, although it is not as robust. When saturation levels of CO₂ increase, so does the pore pressure. There is a constant increase in the velocity of the P waves at a given porosity. This linear increase can be used to potentially prove the effectiveness of 4-D seismic monitoring of CO₂ in geological sequestration. If the trend would be interrupted while monitoring, it would indicate a possible leak of CO₂ that could potentially have significant effects on the surrounding rock strata.

Sub-Critical CO₂ in a Limestone

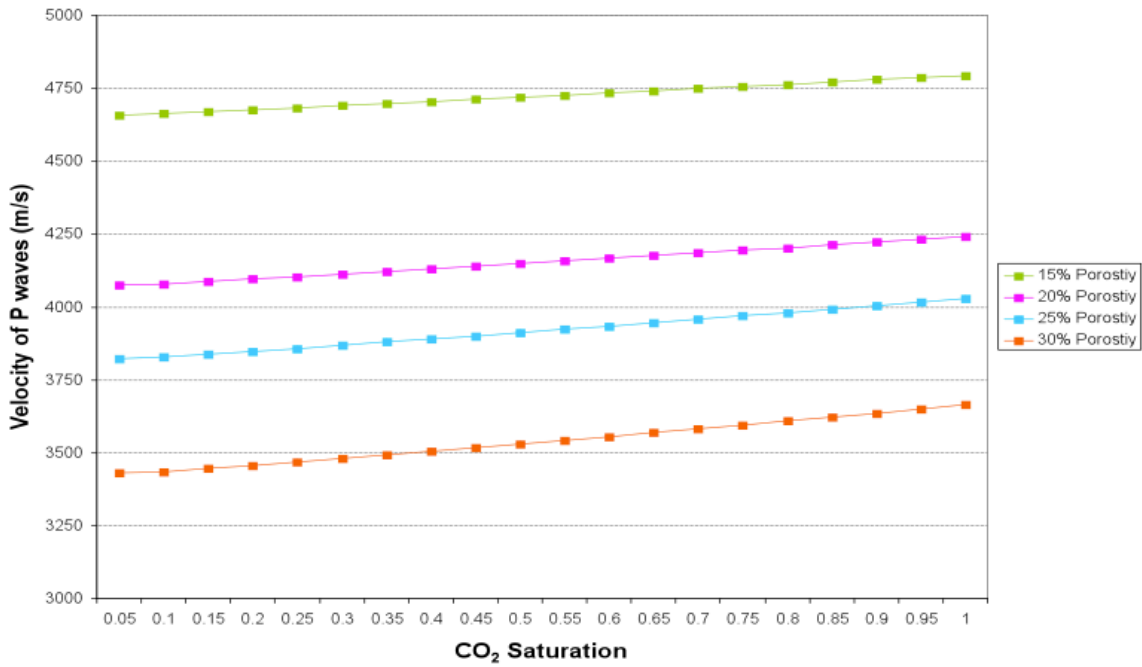


Figure 4.51 Graph of theoretical values of sub-critical CO₂ in limestone, comparing velocity of P-waves (m/s) to increasing saturation levels CO₂. Data used to create graph is found in Appendix C.

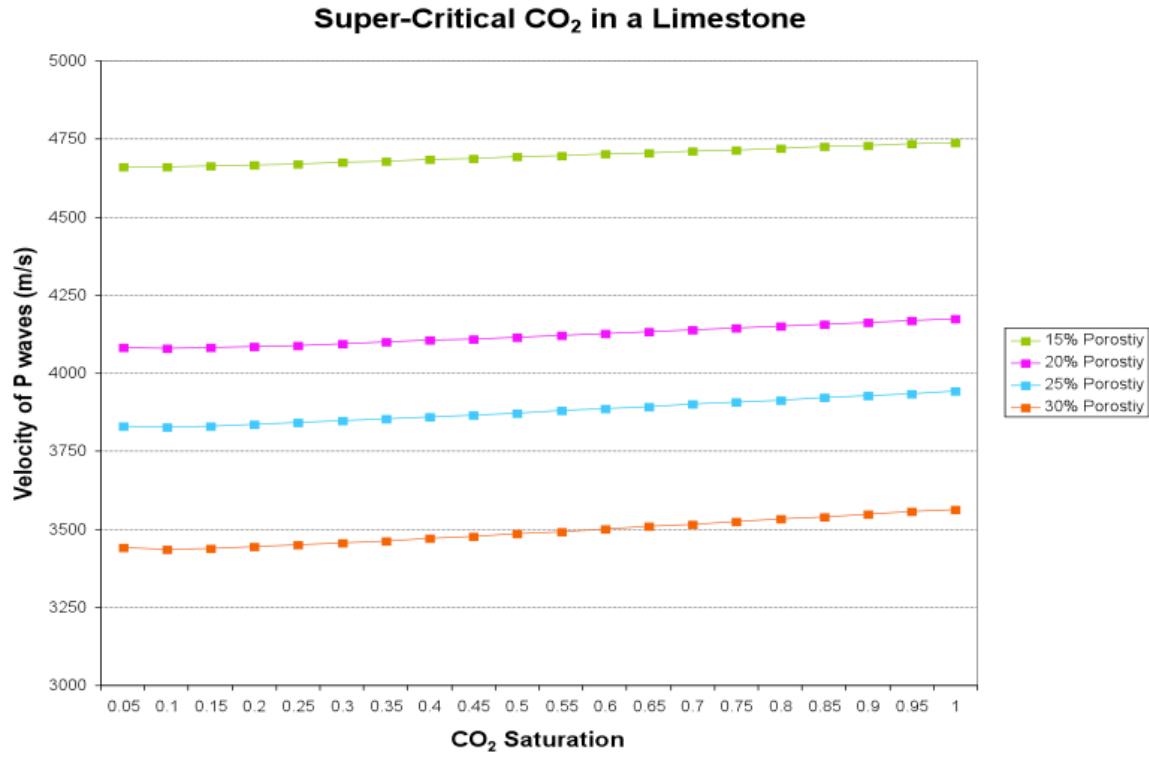


Figure 4.52 Graph of theoretical values of super-critical CO₂ in limestone, comparing velocity of P-waves (m/s) to increasing saturation levels CO₂. Data used to create graph is found in Appendix C.

Sub-Critical CO₂ in a Sandstone

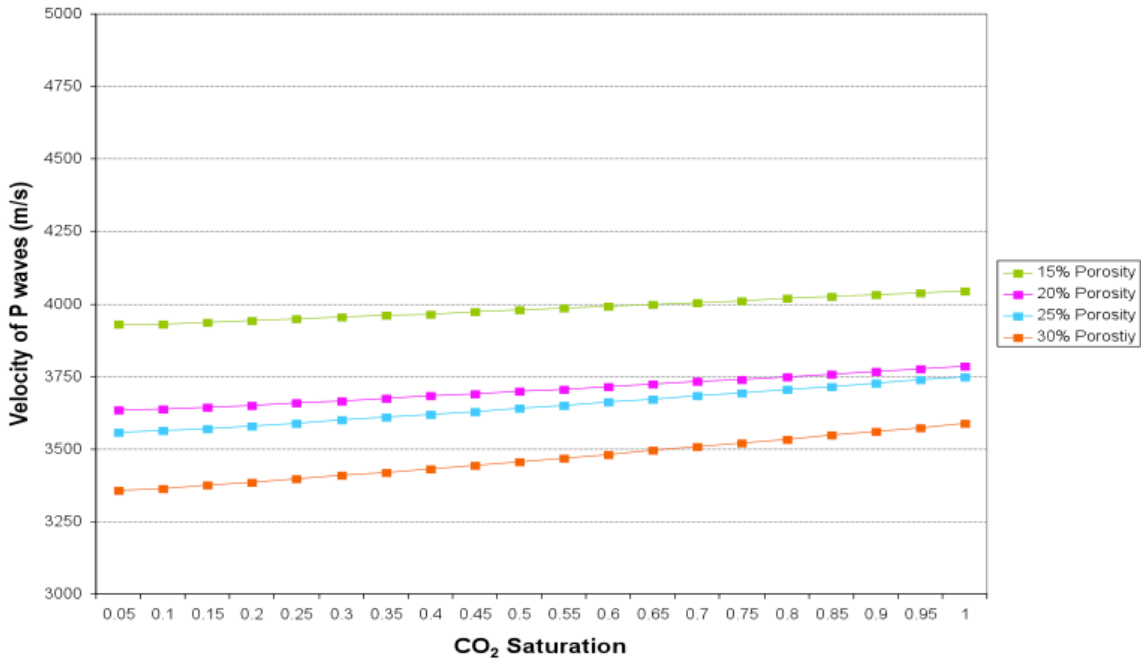


Figure 4.53 Graph of theoretical values of sub-critical CO₂ in sandstone, comparing velocity of P-waves (m/s) to increasing saturation levels CO₂. Data used to create graph is found in Appendix C.

Super-Critical CO₂ in a Sandstone

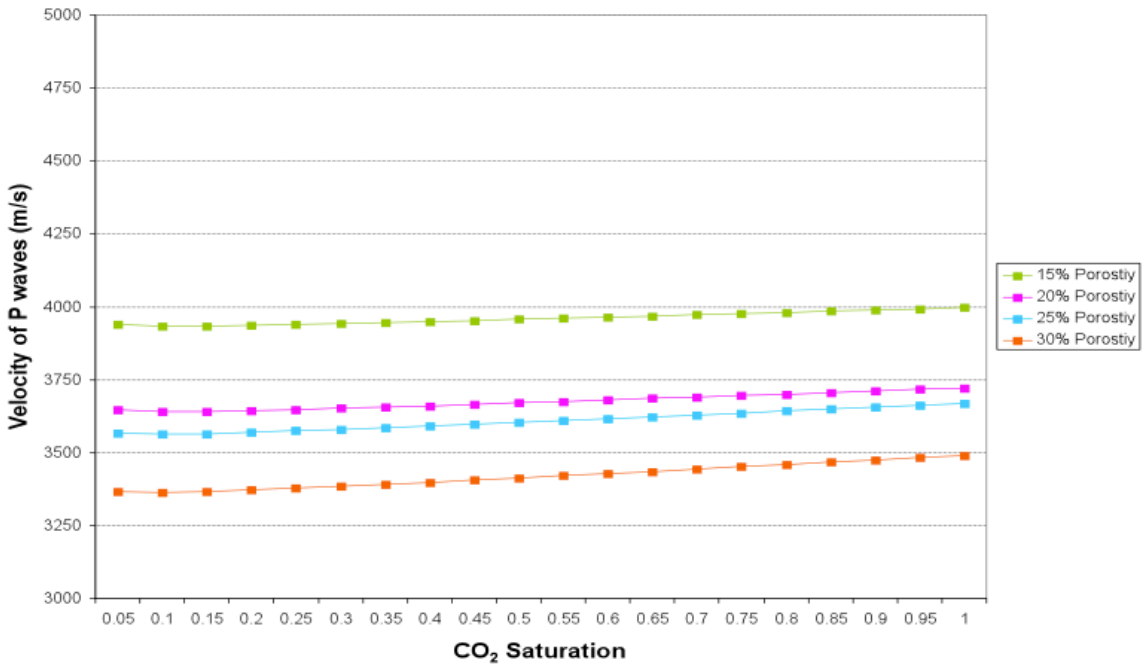


Figure 4.54 Graph of theoretical values of super-critical CO₂ in sandstone, comparing velocity of P-waves (m/s) to increasing saturation levels CO₂. Data used to create graph is found in Appendix C.

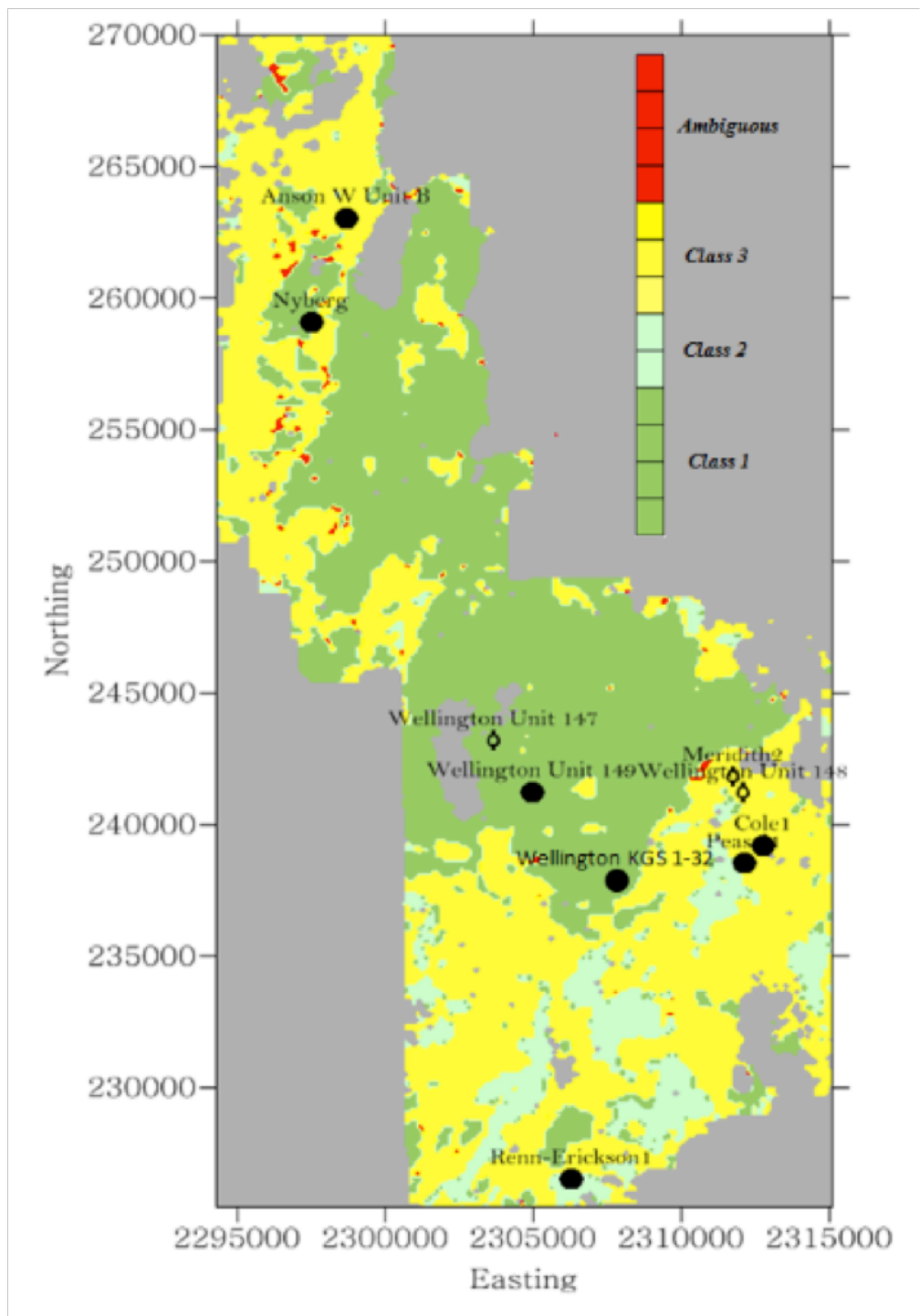


Figure 4.55 Map showing three different porosity classes for the top of the Mississippian in the Wellington field. Class 1, indicated in dark green, is porosity values greater than 12%. Class 2, indicated in sea foam green, is porosity values from 8 to 12%. Class 3, indicated in yellow, is porosity values less than 8%. The red areas on the map represent ambiguous areas. Well of interest is Wellington KGS 1-32. Image from Ohl, D. R., and Raef, A. B. (under review, 2012).

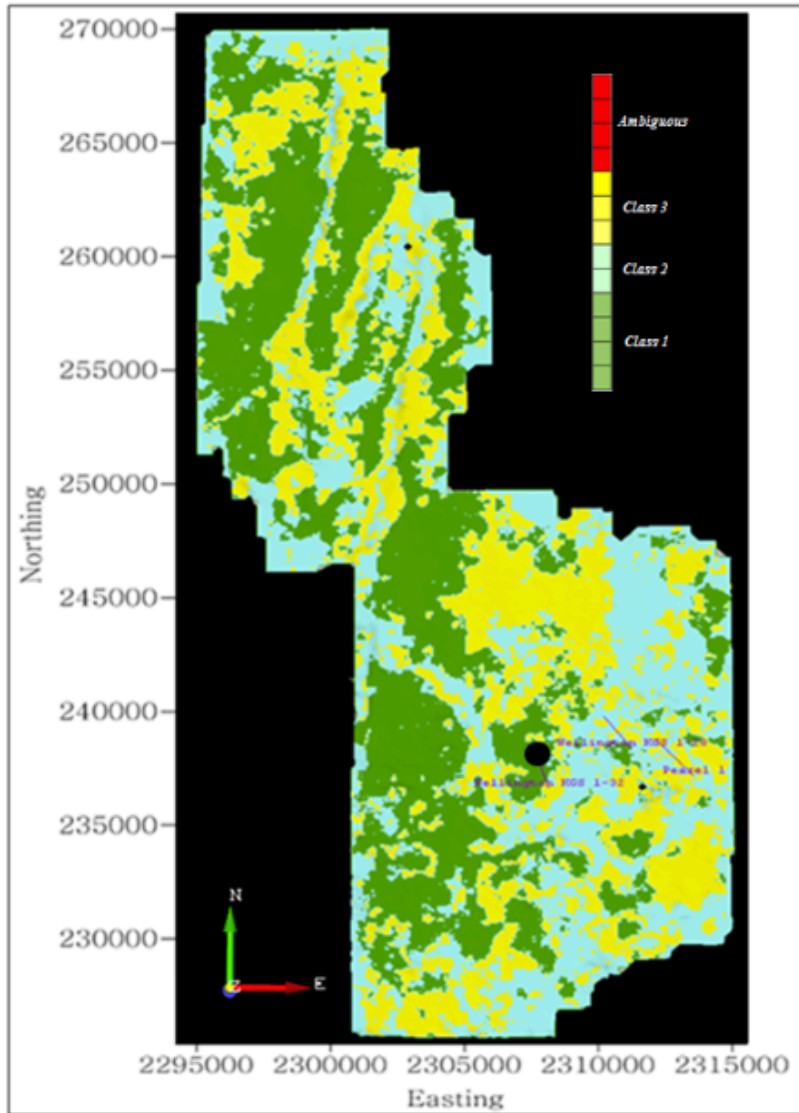


Figure 4.56 Map showing three different porosity classes for the top of the Arbuckle in the Wellington field. Class 1, indicated in dark green, is porosity values greater than 12%. Class 2, indicated in sea foam green, is porosity values from 8 to 12%. Class 3, indicated in yellow, is porosity values less than 8%. The red areas on the map represent ambiguous areas. Well of interest is Wellington KGS 1-32. Image from Ohl, D. R., and Raef, A. B. (under review, 2012).

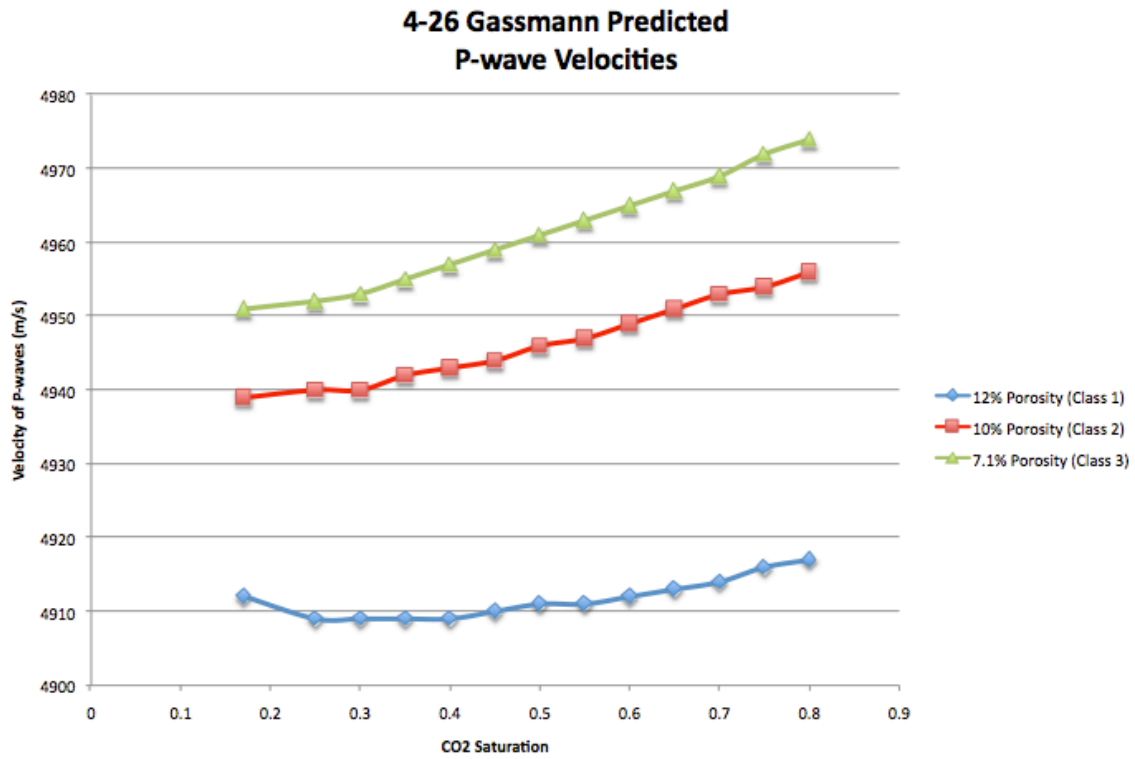


Figure 4.57 Graph showing the change in velocities of P-waves in relation to CO₂ saturations for sample 4-26. Classes correlated with Figure 4.55. Data used to create graph is found in Appendix C.

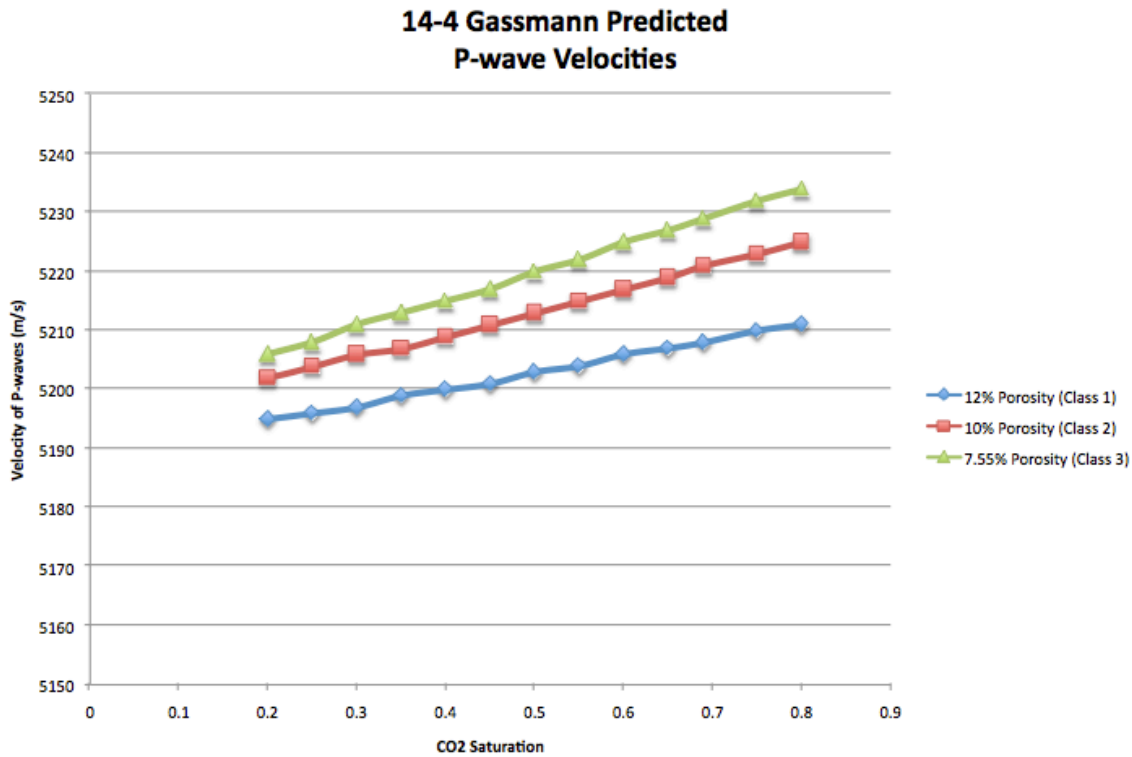


Figure 4.58 Graph showing the change in velocities of P-waves in relation to CO₂ saturations for sample 14-4. Classes correlated with Figure 4.56. Data used to create graph is found in Appendix C.

For the deep core Gassmann modeling for sample 4-26 and 14-4, we used the core porosity, determined by Weatherford Laboratories, for the lowest end of the porosity values. For the two other cases, in each model, we used the percentage values derived from Ohl, D. R., and Raef, A. B. (under review, 2012) for the various classes of porosities. Modeling for properties of the core 4-26, showed greater variability in regards to a change in porosity than seen for core 14-4. When looking at permeability data, 14-4 has much higher values than 4-26. So it could potentially model more similarly to sandstone, due to the interconnectivity of the pore space. However, they both displayed a general increasing trend with increasing levels of CO₂ saturation. The modeling completed for the porosity

classes in the Wellington field, as seen in Figure 4.57, could provide substance for the feasibility of time lapse seismic monitoring for geosequestration of carbon dioxide, in regards to variation in porosity across the field.

Chapter 5 - Conclusions

From the integration and analysis of laboratory ultrasonic measurements, well logs, thin sections, and Gassmann fluid replacement modeling, there are implications of feasibility for time lapse seismic monitoring for CO₂ sequestration. Ultrasonic velocity measurements can be used in a number of ways to better understand elastic properties of rocks. Elastic moduli and rock data, derived from the dry rock frame, allow applications of Gassmann modeling for fluid substitution for different petrophysical properties. This study has provided some baseline data for modeling fluid replacement effects, as well as noting change in amplitude and velocity response as a function of a change in effective stress. This response could be used for time-lapse monitoring of CO₂ injection in terms of saturation or potential leakage. During injection, if there were a leak, you would be able to note the change of amplitude and velocity in near surface formations being affected by the CO₂. The change would be caused by the increase of pore pressure, which would reduce the effective pressure. Modeling for two main petrophysical facies for the Wellington field has been conducted, and would enable study feasibility of time lapse seismic monitoring of future geosequestration in the Arbuckle. Also, wave attenuation variation could be linked to micro cracks. If attenuation is impacted on a micro scale, then there could be potential of viability for use in fracture monitoring.

References

- Adam, L., Batzle, M., Brevik, I. (2006). Gassmann's fluid substitution and shear modulus variability in carbonates at laboratory seismic and ultrasonic frequencies: *Geophysics*, 77(6), 173-183.
- Adler, F. J. (1971). Future petroleum provinces of the mid- continent, region 7; in, *Future Petroleum Provinces of the United States—Their Geology and Potential: American Association of Petroleum Geologists, Memoir 15*, 985- 1120.
- Artola, F. A. V., Alvarado, V. (2006). Sensitivity analysis of Gassmann's fluid substitution equations: Some implications in feasibility studies of time-lapse seismic reservoir monitoring: *Journal of Applied Geophysics*, 59, 47-62.
- Batzle, M., Wang, Z. (1992). Seismic properties of pore fluids: *Geophysics*, 57(11), 1396-1408.
- Besheli, S. A., Hendi, S. S., Vali, J. (1998). Reservoir Characterization by Seismic Attributes With Vp & Vs Measurement of core samples (a "Rock Physics" study): Geophysics Department, RIPI-NIOC.
- Bickle, M. J. (2009). Geological carbon storage: *Nature Geoscience*, 2, 815-818.
- Carr, T. R., Merriam, D. F., Bartley, J. D. (2005). Use of relational databases to evaluate regional petroleum accumulation, groundwater flow, and CO₂ sequestration in Kansas: *AAPG Bulletin*, 89(12), 1607-1627.
- Castagna, J. P., Batzle, M, Eastwood, R. L. (1985). Relationship between compressional-wave and shear-wave velocities in clastic silicate rocks: *Geophysics*, 50(4), 571-581.
- Clark, V. A., Tittman, B. R., Spencer, T. W. (1980). Effects of volatiles on attenuation and velocity in sedimentary rocks: *Geophysics*, 85, 5190-5198.
- Franseen, E. K., Byrnes, A. P., Cansler, J. R., Steinhauff, D. M., Carr, T. R., and Dubois, M. K. (2003). Geological Controls on Variable Character of Arbuckle Reservoirs in Kansas: *An Emerging Picture*, No. 59.
- Franseen, E. K., Byrnes, A. P., Cansler, J. R., Steinhauff, D. M., Carr, T. R. (2004). Current Research in Earth Sciences, *Bulletin 250*, part 2.
- Franseen, E. K., Byrnes, A. P., Cansler, J. R., Steinhauff, D. M., Carr, T. R., Dubois, M. K. (2003). Geological Controls on Variable Character of Arbuckle Reservoirs in Kansas: *An Emerging Picture*, No. 59.

- Grochau, M., Gurevich, B. (2009). Testing Gassmann Fluid Substitution: Sonic logs Versus Ultrasonic Core Measurements, 57, 75-79.
- Haldorsen, H. H., Damsleth, E. (1993). Challenges in Reservoir Characterization: Geohorizons, 77(4), 541-551.
- Han, D., Batzle, M. L. (2004). Gassmann's equation and fluid-saturation effects on seismic velocities: Geophysics, 69(2), 398-405.
- Herzog, H. J. (2001). What Future for Carbon Capture and Sequestration?: Environmental Science and Technology, 35 (7), 148-153.
- King, M. S. (2009). Recent Developments in Seismic rock physics. International Journal of Rock Mechanics and Mining Sciences, 46(8), 1341-1348.
- Lackner, K. S. (2003). Climate Change: A Guide to CO₂ Sequestration. Science, 300(5626), 1677-1678.
- Mavko, G., Mukerji, T., Dvorkin, J. (1998). The Rock Physics Handbook: Tools for Seismic Analysis in Porous Media (First ed.). United Kingdom: Cambridge University Press.
- Mavko, G., Mukerji, T., Dvorkin, J. (2009). The Rock Physics Handbook: Tools for Seismic Analysis in Porous Media (Second ed.). United Kingdom: Cambridge University Press.
- Merriam, D. F. (1963). The Geologic History of Kansas. Lawrence, Kansas: University of Kansas Publications.
- Moore, R. C., Jewett, J. M. (1942). Oil and gas fields of Kansas: Mines, 32(10), 481.
- Moore, R. C., Jewett, J. M., and O'Connor, H. G. (1951). Rock formations of Chase County, Kansas: Kansas Geol. Survey, 11, part 1, 1-16.
- Purcell, C., Harbert, W., Soong, Y., McLendon, T. R., Haljasmaa, I. V., McIntyre, D., JiKich, J. (2009). Velocity measurements in reservoir rock samples from the SACROC unit using various pore fluids, and integration into a seismic survey taken before and after CO₂ sequestration flood: ScienceDirect, 2323-2331.
- Sayers, C. M., Chopra, S. (2009). Rock physics: Leading Edge, 28(1), 15-16.
- Sbar, M. L. (2000). Exploration risk reduction: An AVO analysis in the offshore middle Miocene, central Gulf of Mexico: The Leading Edge, 19, 21-27.
- Simmon, G. (1965). Ultrasonics in Geology: IEEE, 53(10), 1337-1345.
- Singh, Y. Y. (2009). Reservoir Properties Prediction in the West Baram Delta Through Data Integration Constrained by Rock Physics: Leading Edge, 28(12), 1486-1497.

- Smith, T. M., Sondergeld, C. H., & Rai, C. S. (2003). Gassmann Fluid Substitutions: A Tutorial: *Geophysics*, 68(2), 430-440.
- Souder, W. W. (2002). Using Sonic Logs to Predict Fluid Type: *Petrophysics*, 43(5), 412-419.
- Tao, H., Chang-Chun, Z., Fa-Gen, P., Ke-Ying, R., Fan-Da, K., Ge, S. (2010). Laboratory study of fluid viscosity induced ultrasonic velocity dispersion in reservoir sandstones: *Applied Geophysics*, 7(2), 114-126.
- Vernik, L., Hickman, S., Lockner, D., Rusanov, M. (1994). Ultrasonic velocities in cores from the Kola superdeep well and the nature of subhorizontal seismic reflections: *Journal of Geophysical Research*, 99(B12), 24,209-24,219.
- Wang, Z. Z. (2001). Fundamentals of seismic rock physics: *Geophysics*. 66(2), 398-412.
- Wilson, J. L., Fritz, R. D., Medlock, P. L. (1991). The Arbuckle Group—Relationship of Core and Outcrop Analyses to Cyclic Stratigraphy and Correlation; in, *Arbuckle Core Workshop and Field Trip*, KS Johnson, ed: Oklahoma Geological Survey, Special Publication 91-3, 133-144.
- Zellner, D., 1968. "Stratigraphic Succession in Kansas." Bulletin 189. Lawrence, KS: University of Kansas Publications.
- Zeller, D. E. (1968) 2008. Classification of rocks in Kansas, revised by Kansas Geological Survey Stratigraphic Nomenclature Committee; in, *The Stratigraphic Succession in Kansas*: Kansas Geological Survey, Bulletin 189, 81 p., chart.

Appendix A - Core Samples

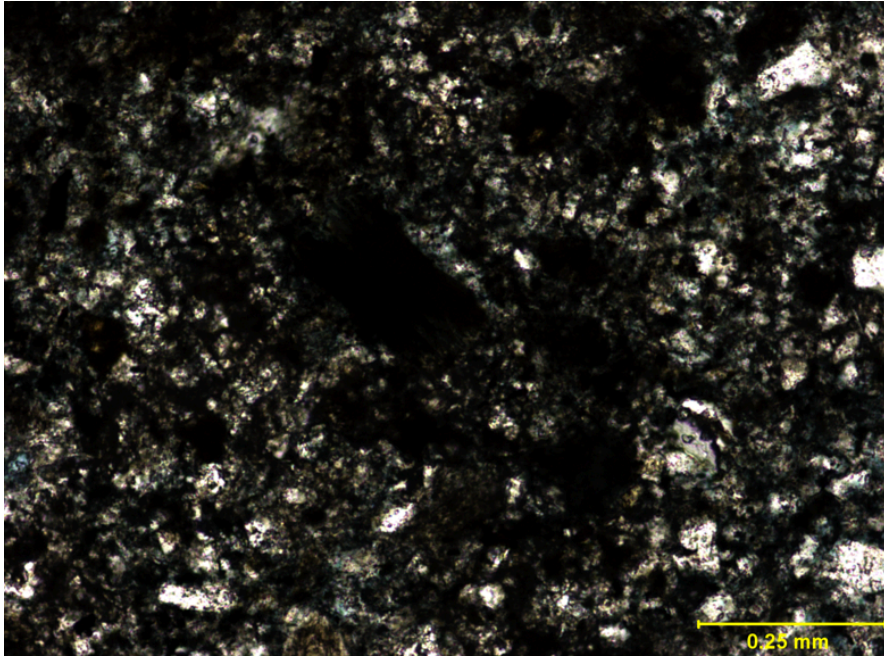
KDOT Cores

B5S2

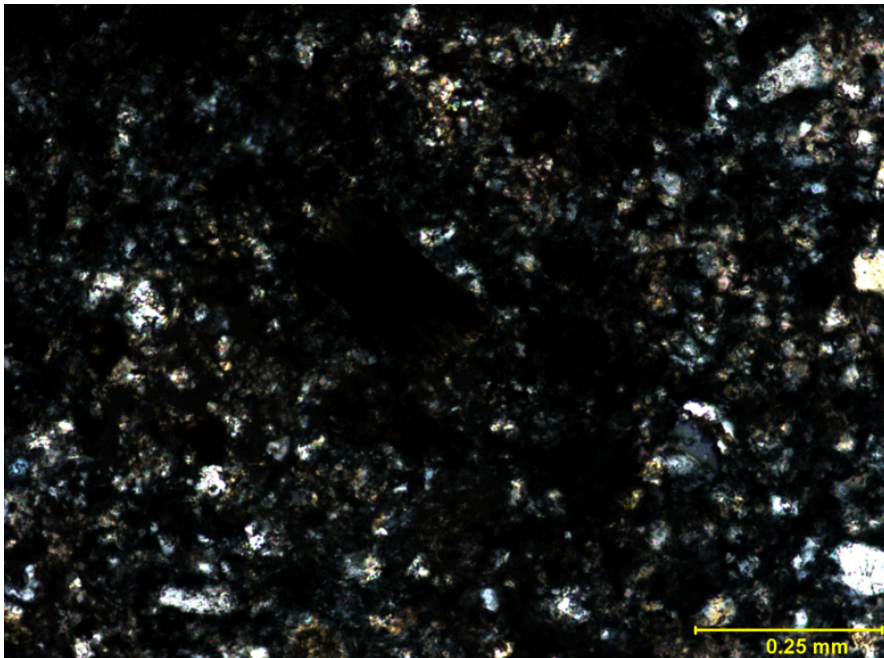


KDOT Core B5S2, view parallel to cored axis.

KDOT Core B5S2, view perpendicular to cored axis.



Thin section image of KDOT Core sample B5S2. Image is at 10X magnification and in plane polarized light.



Thin section image of KDOT Core sample B5S2. Image is at 10X magnification and in crossed polarized light.

Sample	Height (mm)	Diameter (mm)	Mass before dehydration (g)	Density before dehydration (g/mm ³)
B5 S2	92.5	49.5	418.3	2.47E-03

Physical properties of sample B5S2 prior to dehydration.

Sample	Height (mm)	Diameter (mm)	Mass after dehydration (g)	Density after dehydration (g/mm ³)
B5 S2	92.5	49.5	415.4	2.33E-03

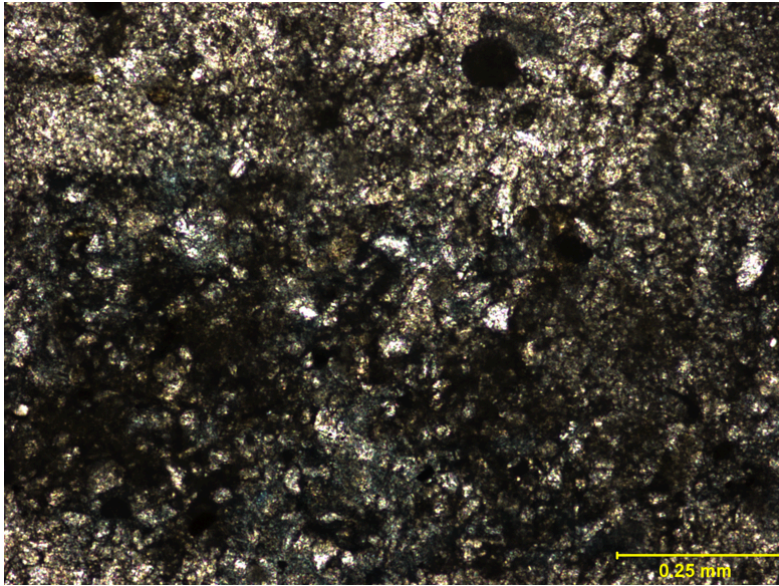
Physical properties of sample B5S2 after dehydration.

B6S1

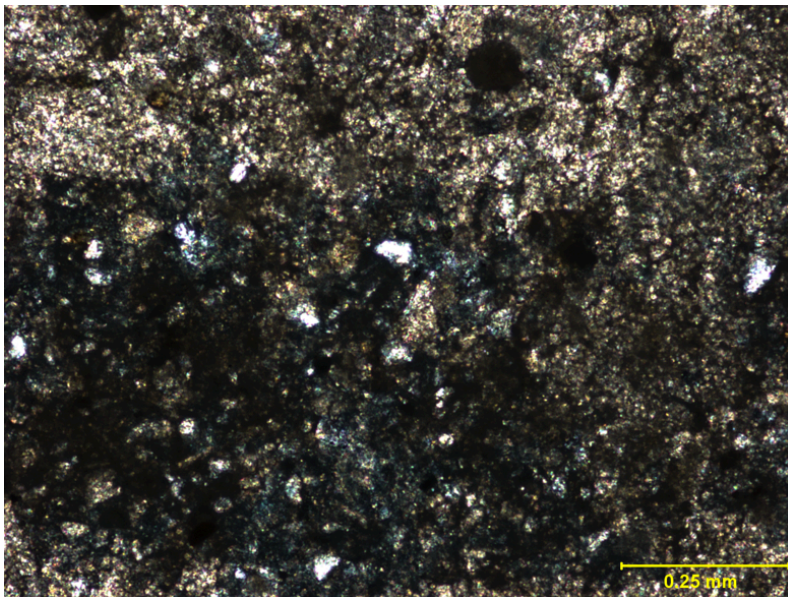


KDOT Core B6S1, view parallel to cored axis.

KDOT Core B6S1, view perpendicular to cored axis.



Thin section image of KDOT Core sample B6S1. Image is at 10X magnification and in plane polarized light.



Thin section image of KDOT Core sample B6S1. Image is at 10X magnification and in crossed polarized light.

Sample	Height (mm)	Diameter (mm)	Mass before dehydration (g)	Density before dehydration (g/mm ³)
B6 S1	100	49.75	481.1	2.23E-03

Physical properties of sample B6S1 prior to dehydration.

Sample	Height (mm)	Diameter (mm)	Mass after dehydration (g)	Density after dehydration (g/mm ³)
B6 S1	100	49.75	477.9	2.46E-03

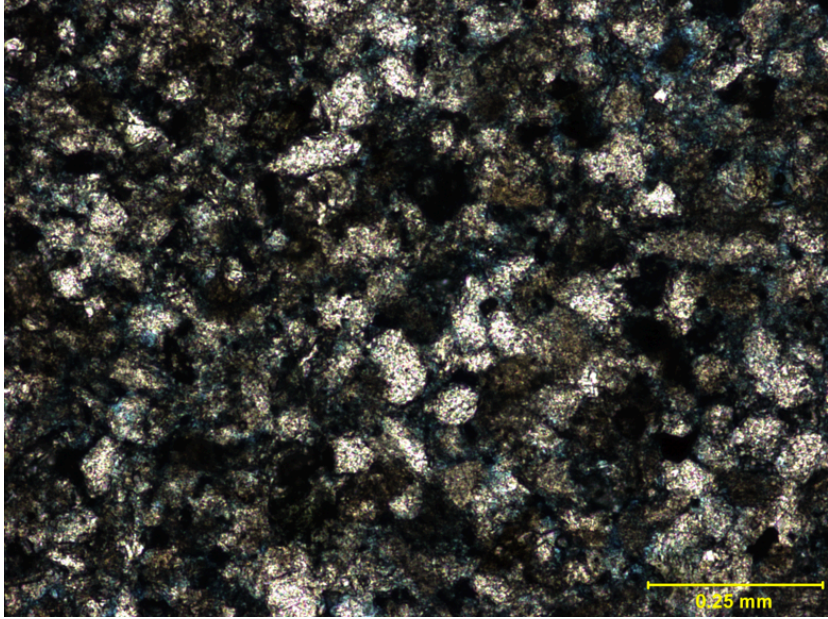
Physical properties of sample B6S1 after dehydration.

B6S2

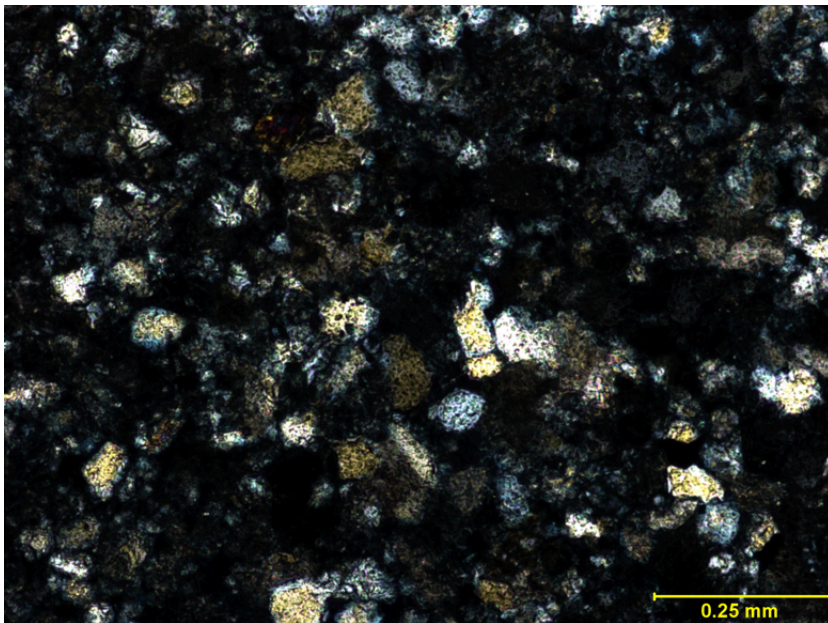


KDOT Core B6S2, view parallel to cored axis.

KDOT Core B6S2, view perpendicular to cored axis.



Thin section image of KDOT Core sample B6S2. Image is at 10X magnification and in plane polarized light.



Thin section image of KDOT Core sample B6S2. Image is at 10X magnification and in crossed polarized light.

Sample	Height (mm)	Diameter (mm)	Mass before dehydration (g)	Density before dehydration (g/mm ³)
B6 S2	94	49.5	403.8	2.44E-03

Physical properties of sample B6S2 prior to dehydration.

Sample	Height (mm)	Diameter (mm)	Mass after dehydration (g)	Density after dehydration (g/mm ³)
B6 S2	94	49.5	402.5	2.23E-03

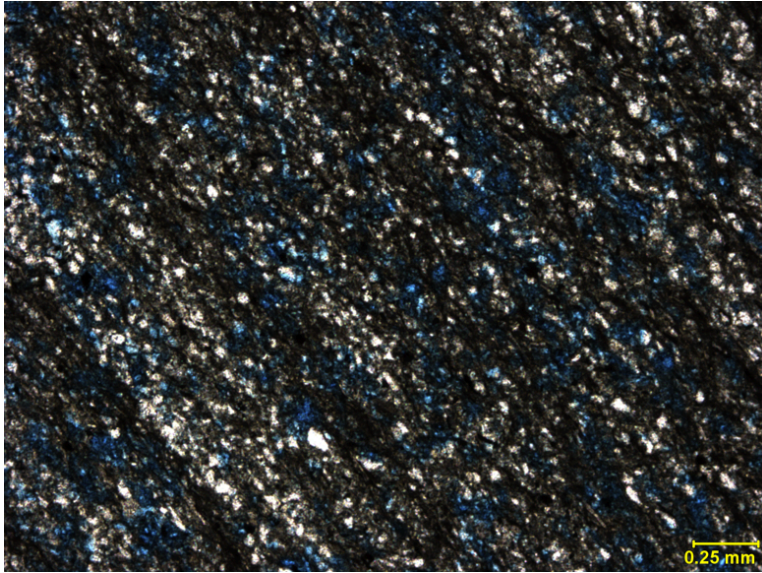
Physical properties of sample B6S2 after dehydration.

B8S1



KDOT Core B8S1, view parallel to cored axis.

KDOT Core B8S1, view perpendicular to cored axis.



Thin section image of KDOT Core sample B8S1. Image is at 4X magnification and in plane polarized light.



Thin section image of KDOT Core sample B8S1. Image is at 4X magnification and in crossed polarized light.

Sample	Height (mm)	Diameter (mm)	Mass before dehydration (g)	Density before dehydration (g/mm ³)
B8 S1	97.5	49.5	457.6	2.72E-03

Physical properties of sample B8S1 prior to dehydration.

Sample	Height (mm)	Diameter (mm)	Mass after dehydration (g)	Density after dehydration (g/mm ³)
B8 S1	97.5	49.5	455.8	2.43E-03

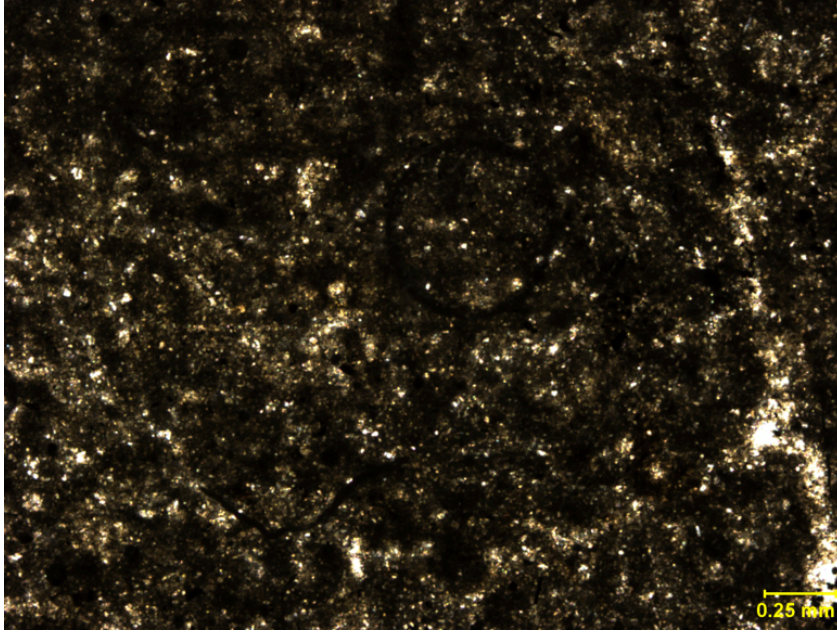
Physical properties of sample B8S1 after dehydration.

B9S3

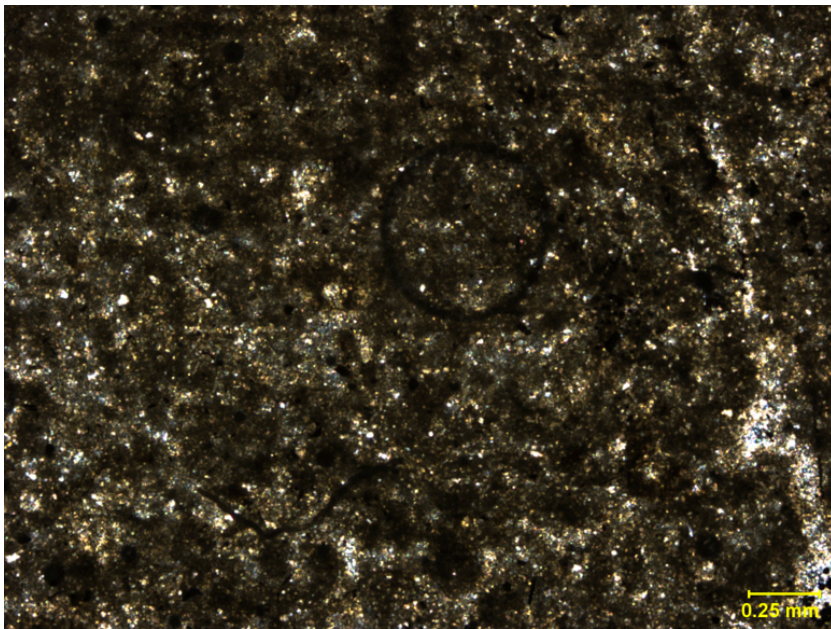


KDOT Core B9S3, view parallel to cored axis.

KDOT Core B9S3, view perpendicular to cored axis.



Thin section image of KDOT Core sample B9S3. Image is at 4X magnification and in plane polarized light.



Thin section image of KDOT Core sample B9S3. Image is at 4X magnification and in crossed polarized light.

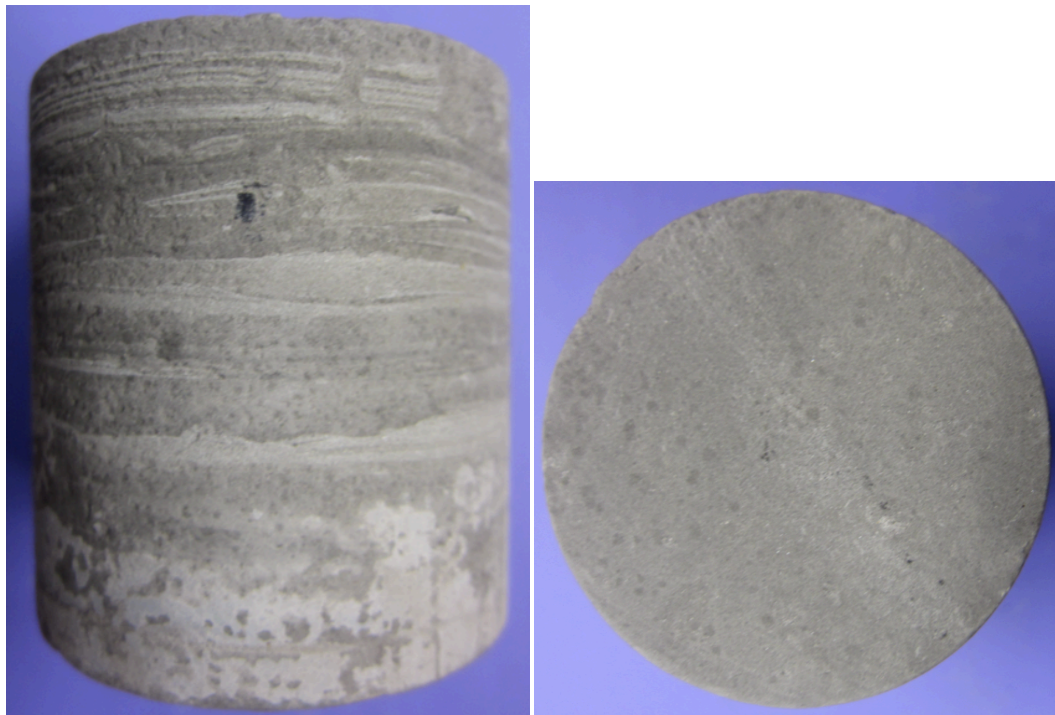
Sample	Height (mm)	Diameter (mm)	Mass before dehydration (g)	Density before dehydration (g/mm ³)
B9 S3	95	49.5	441.6	2.23E-03

Physical properties of sample B9S3 prior to dehydration.

Sample	Height (mm)	Diameter (mm)	Mass after dehydration (g)	Density after dehydration (g/mm ³)
B9 S3	95	49.5	432.6	2.37E-03

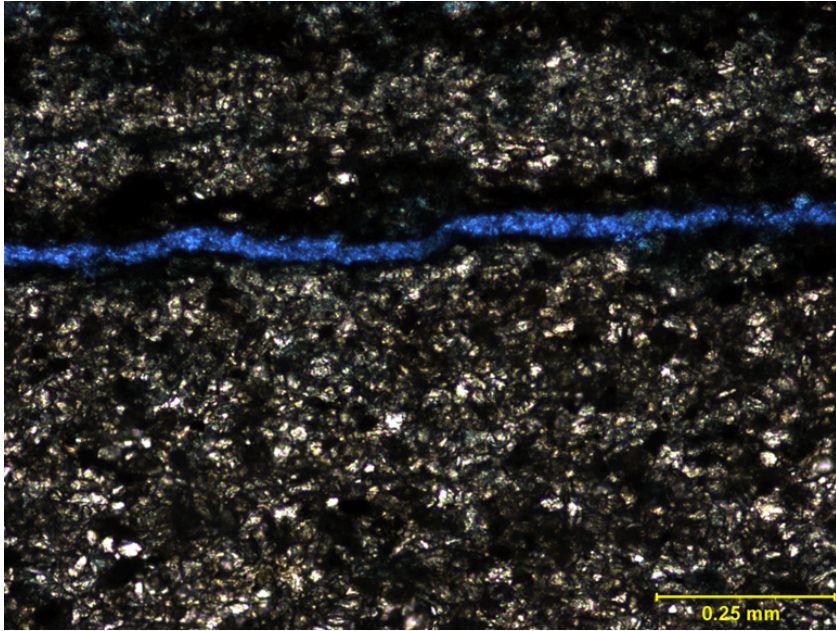
Physical properties of sample B9S3 after dehydration.

B10S2

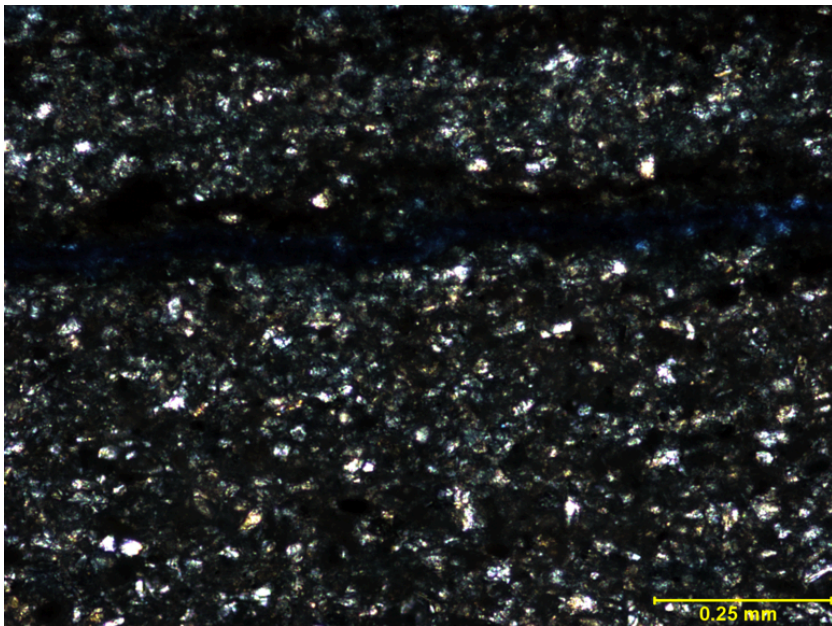


KDOT Core B10S2, view parallel to cored axis.

KDOT Core B10S2, view perpendicular to cored axis.



Thin section image of KDOT Core sample B10S2. Image is at 10X magnification and in plane polarized light.



Thin section image of KDOT Core sample B10S2. Image is at 10X magnification and in plane polarized light.

Sample	Height (mm)	Diameter (mm)	Mass before dehydration (g)	Density before dehydration (g/mm ³)
B10 S2	52.5	49.5	225.5	2.73E-03

Physical properties of sample B10S2 prior to dehydration.

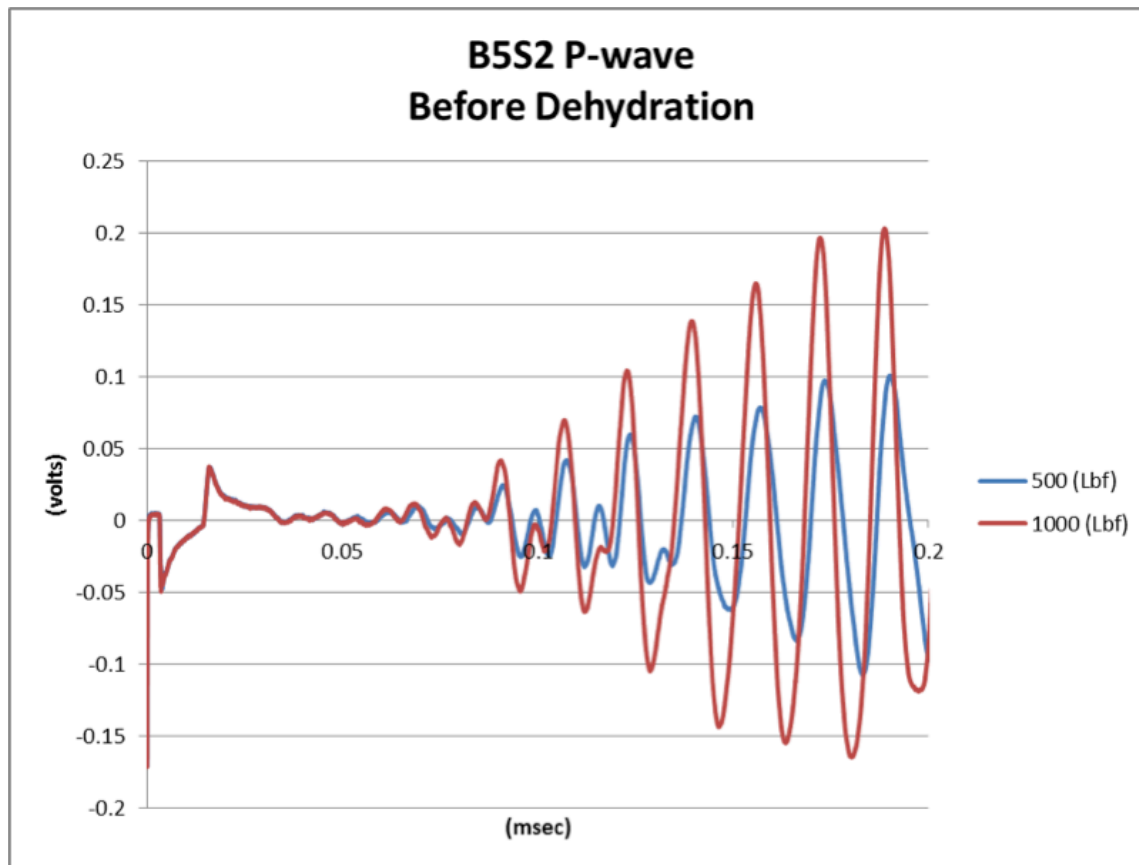
Sample	Height (mm)	Diameter (mm)	Mass after dehydration (g)	Density after dehydration (g/mm ³)
B10 S2	52.5	49.5	221.2	2.19E-03

Physical properties of sample B10S2 after dehydration.

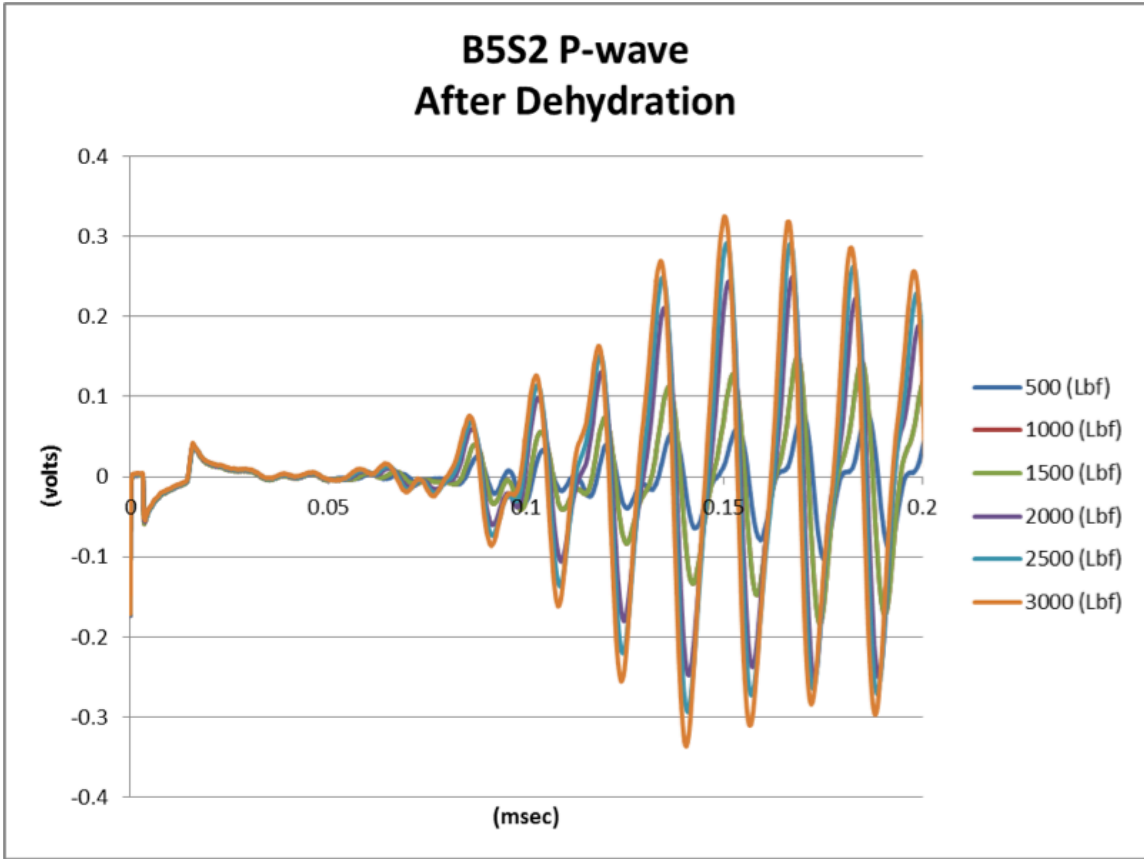
Appendix B - Waveform Graphs and Data

KDOT Cores

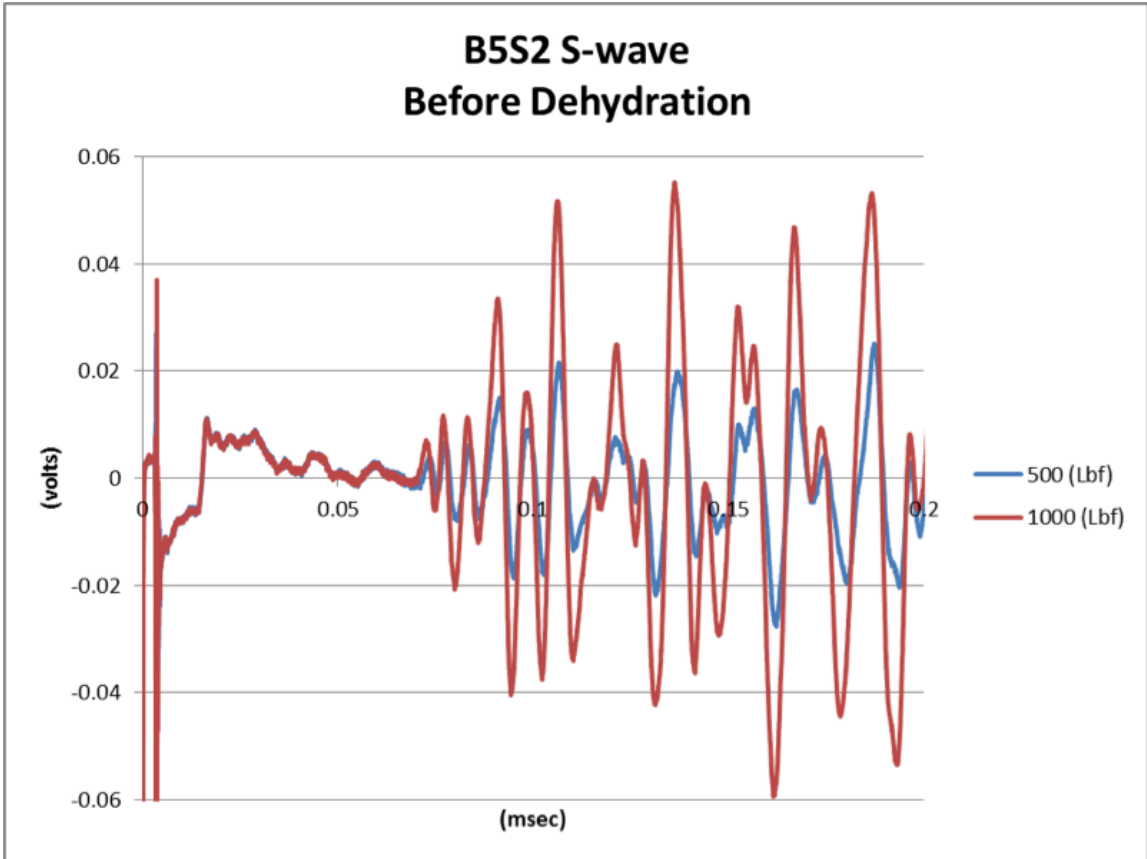
B5S2



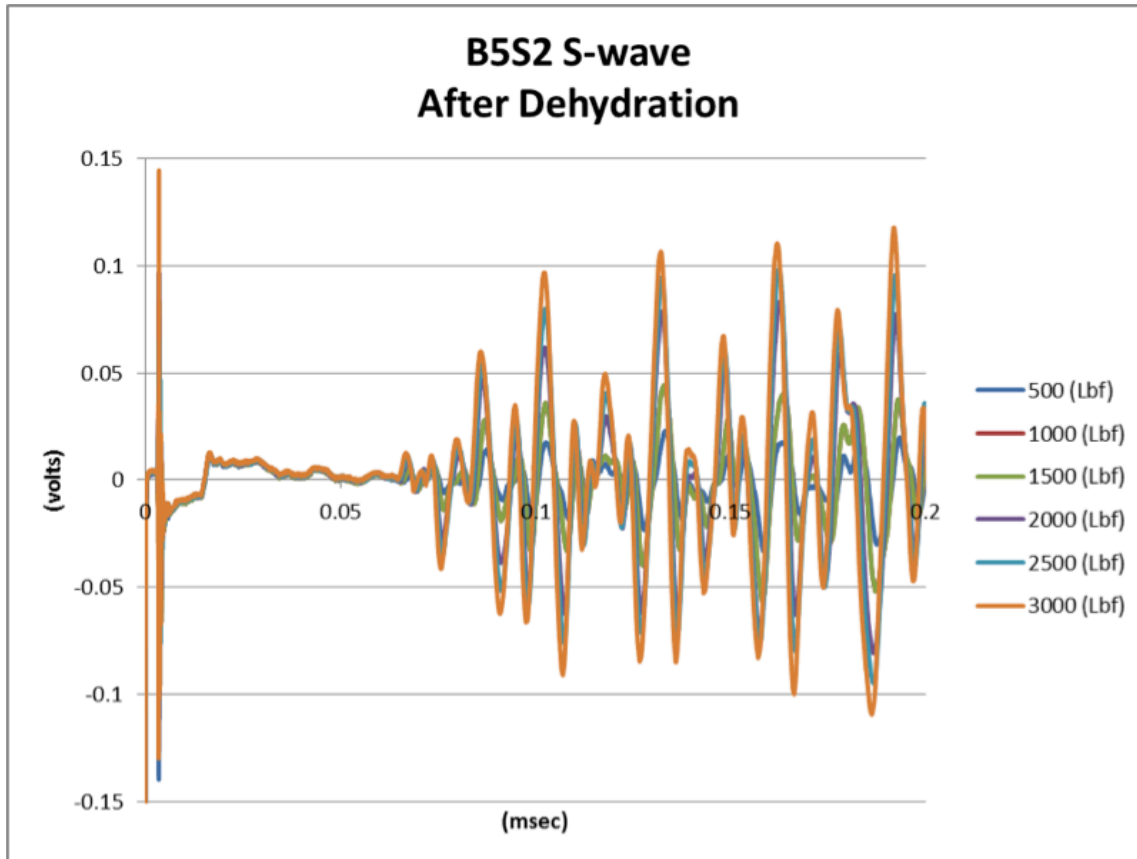
Graph of sample B5S2, P waveform from 500 Lbf to 1000 Lbf prior to sample dehydration.



Graph of sample B5S2, P waveform from 500 Lbf to 3000 Lbf after sample dehydration.



Graph of sample B5S2, S waveform from 500 Lbf to 1000 Lbf prior to sample dehydration.



Graph of sample B5S2, S waveform from 500 Lbf to 3000 Lbf after sample dehydration.

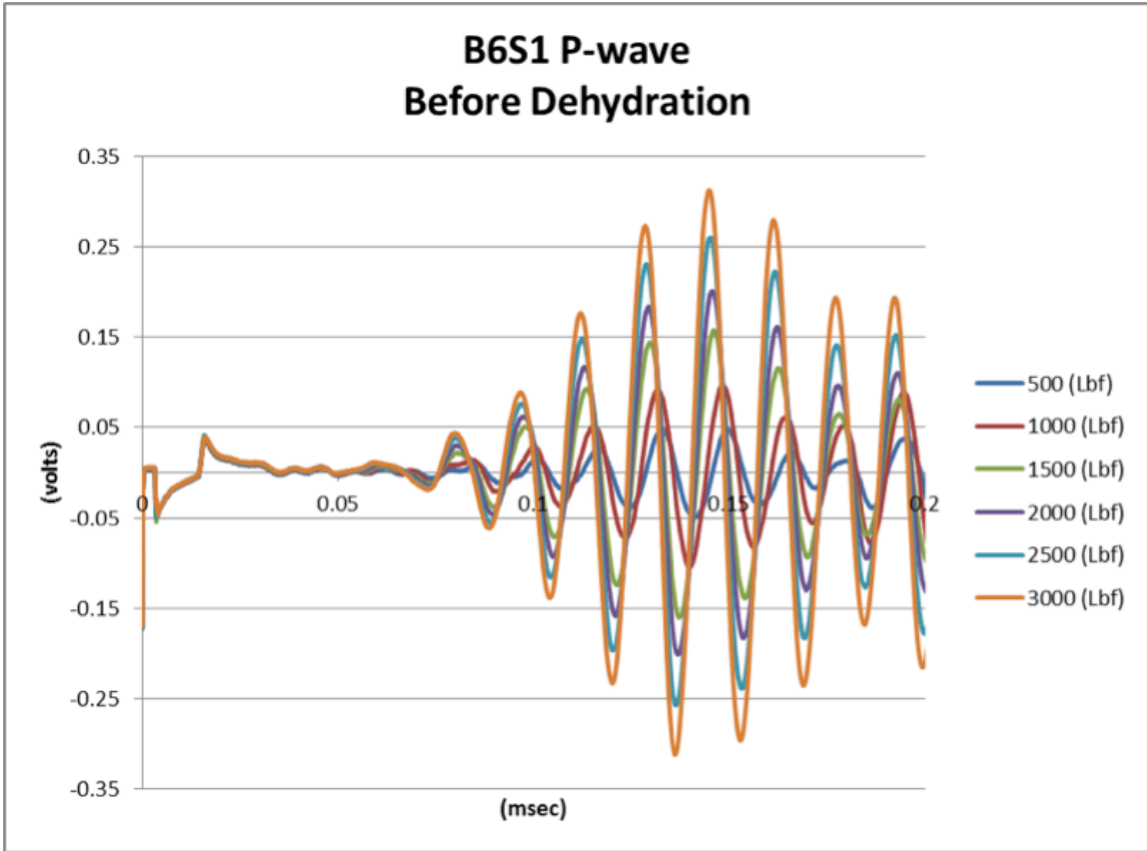
B5S2 Before Dehydration						
Lbf	P wave (m/s)	S wave (m/s)	Poisson's Ratio	Young's Modulus (kPa)	Bulk Modulus (kPa)	Shear Modulus (kPa)
500	5135	1644	0.44	18317308	53492452	6347267
1000	5224	1674	0.44	18926316	55873400	6555503

Velocity of P- and S-waves and elastic moduli of sample B5S2 before dehydration.

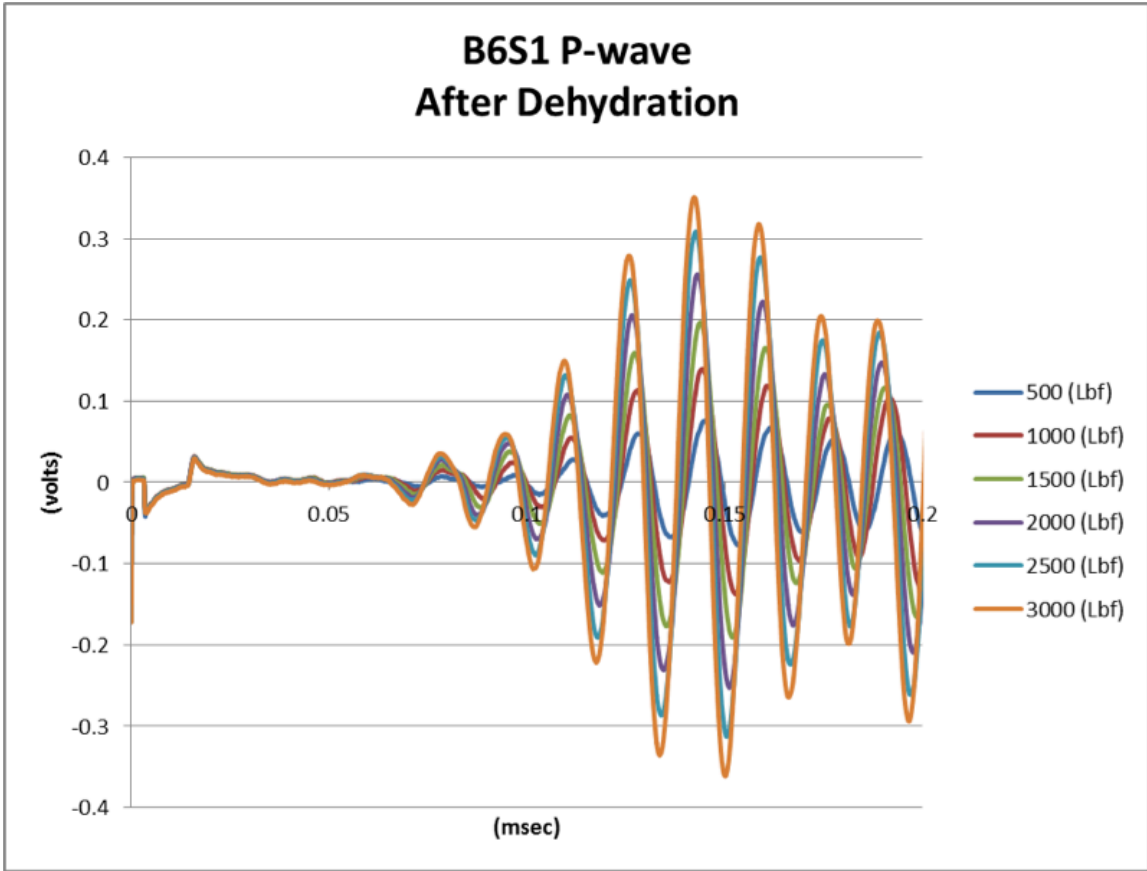
B5S2 After Dehydration						
Lbf	P wave (m/s)	S wave (m/s)	Poisson's Ratio	Young's Modulus (kPa)	Bulk Modulus (kPa)	Shear Modulus (kPa)
500	5102	1827	0.43	22062650	50427688	7729990
1000	5182	1835	0.43	22457446	52178252	7861782
1500	5209	1843	0.43	22636430	52758856	7923198
2000	5235	1850	0.43	22984488	53232576	8047579
2500	5256	1857	0.43	22994842	53736812	8047579
3000	5344	1863	0.43	23181218	55832260	8100784

Velocity of P- and S-waves and elastic moduli of sample B5S2 after dehydration.

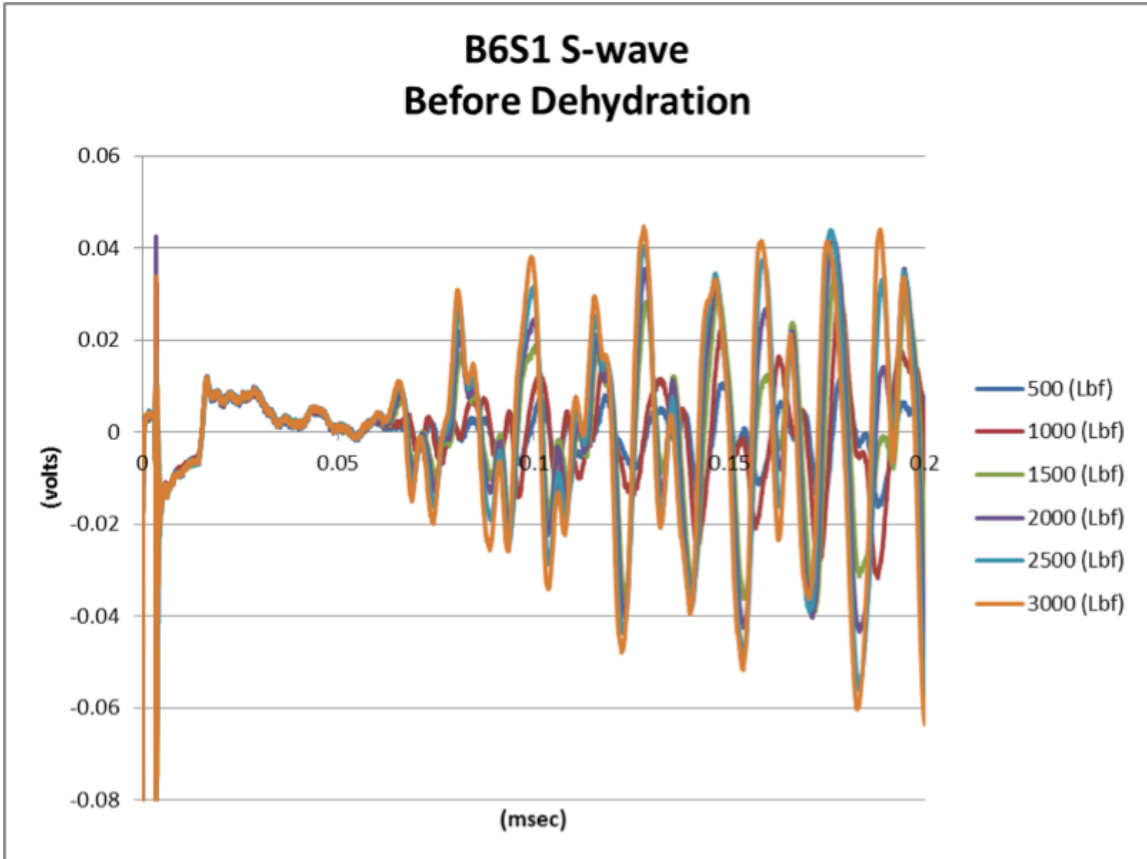
B6S1



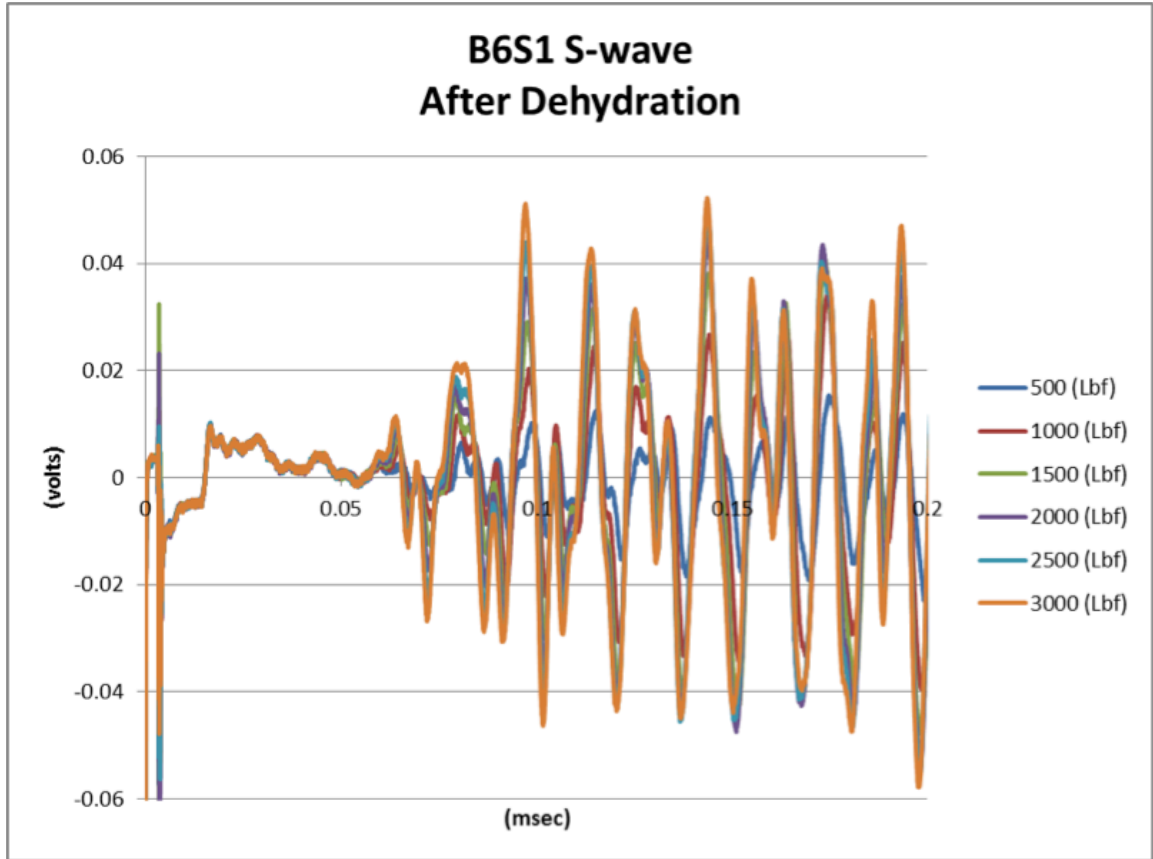
Graph of sample B6S1, P waveform from 500 Lbf to 3000 Lbf prior to sample dehydration.



Graph of sample B6S1, P waveform from 500 Lbf to 3000 Lbf after sample dehydration.



Graph of sample B6S1, S waveform from 500 Lbf to 3000 Lbf prior to sample dehydration.



Graph of sample B6S1, S waveform from 500 Lbf to 3000 Lbf after sample dehydration.

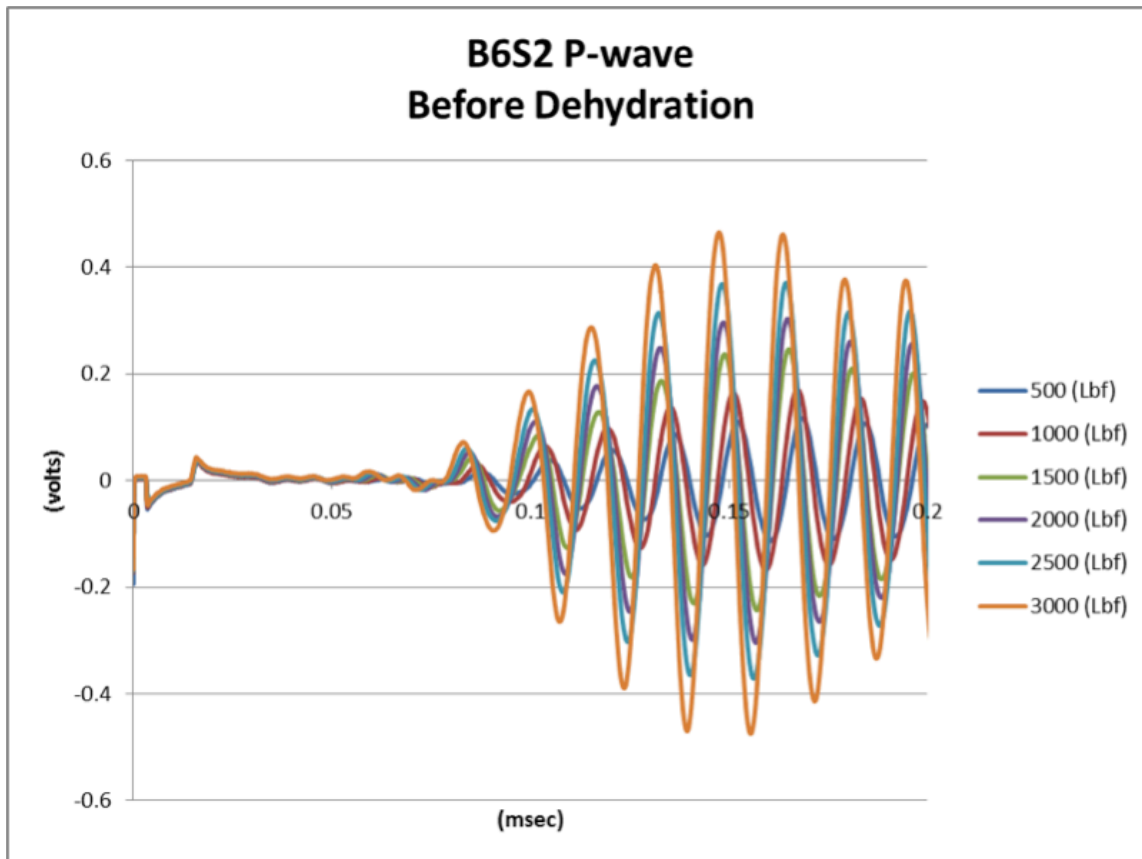
B6S1 Before Dehydration							
Lbf	P wave (m/s)	S wave (m/s)	Poisson's Ratio	Young's Modulus (kPa)	Bulk Modulus (kPa)	Shear Modulus (kPa)	
500	5294	1970	0.42	27262284	56569564	9601656	
1000	5333	1981	0.42	27572550	57438536	9708685	
1500	5473	2037	0.42	29151102	60438748	10267274	
2000	5501	2058	0.42	29730166	60922988	10478202	
2500	5526	2061	0.42	29836290	61570716	10511394	
3000	5478	2070	0.42	30043936	60135104	10603253	

Velocity of P- and S-waves and elastic moduli of sample B6S1 before dehydration.

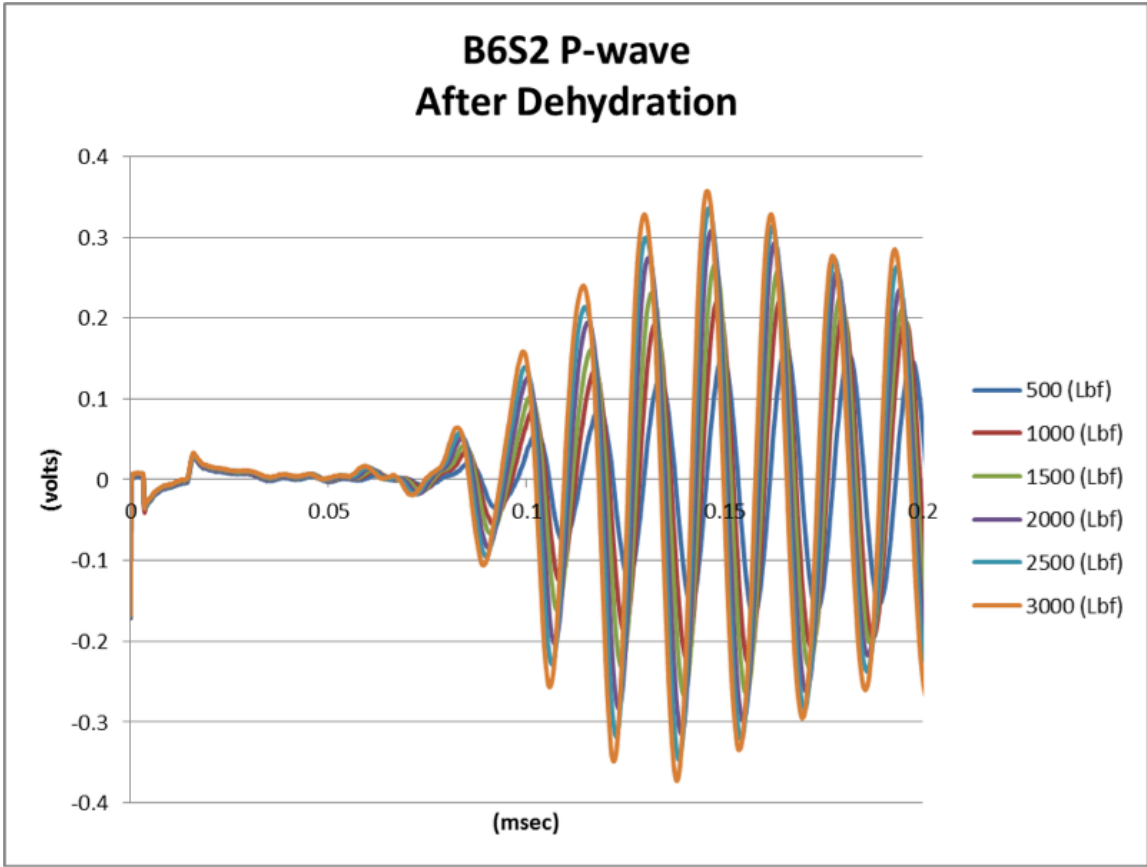
B6S1 After Dehydration							
Lbf	P wave (m/s)	S wave (m/s)	Poisson's Ratio	Young's Modulus (kPa)	Bulk Modulus (kPa)	Shear Modulus (kPa)	
500	5587	2207	0.41	33722060	60776828	11979206	
1000	5684	2214	0.41	33995240	63359908	12050124	
1500	5459	2236	0.4	34384104	56877188	12286669	
2000	5587	2241	0.4	34667620	60278048	12344740	
2500	5634	2257	0.4	35171284	61344956	12521427	
3000	5671	2271	0.4	35622384	62155816	12681690	

Velocity of P- and S-waves and elastic moduli of sample B6S1 after dehydration.

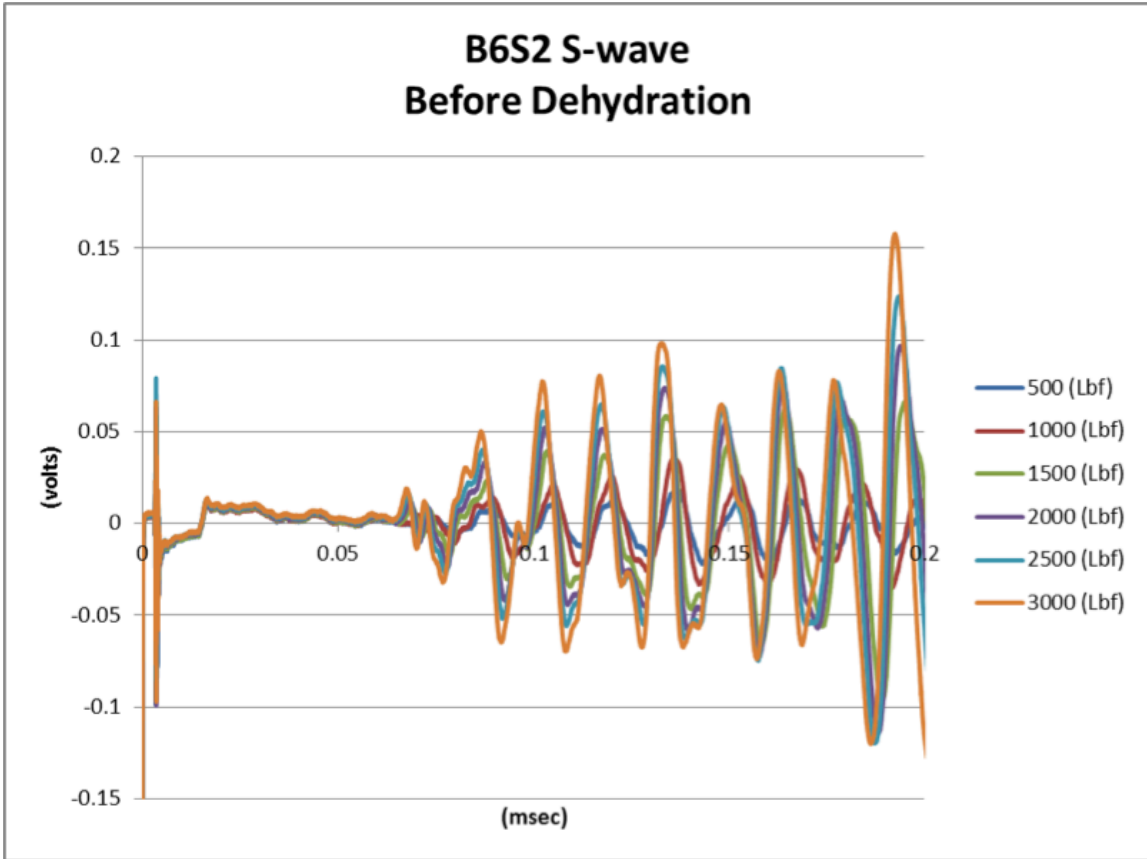
B6S2



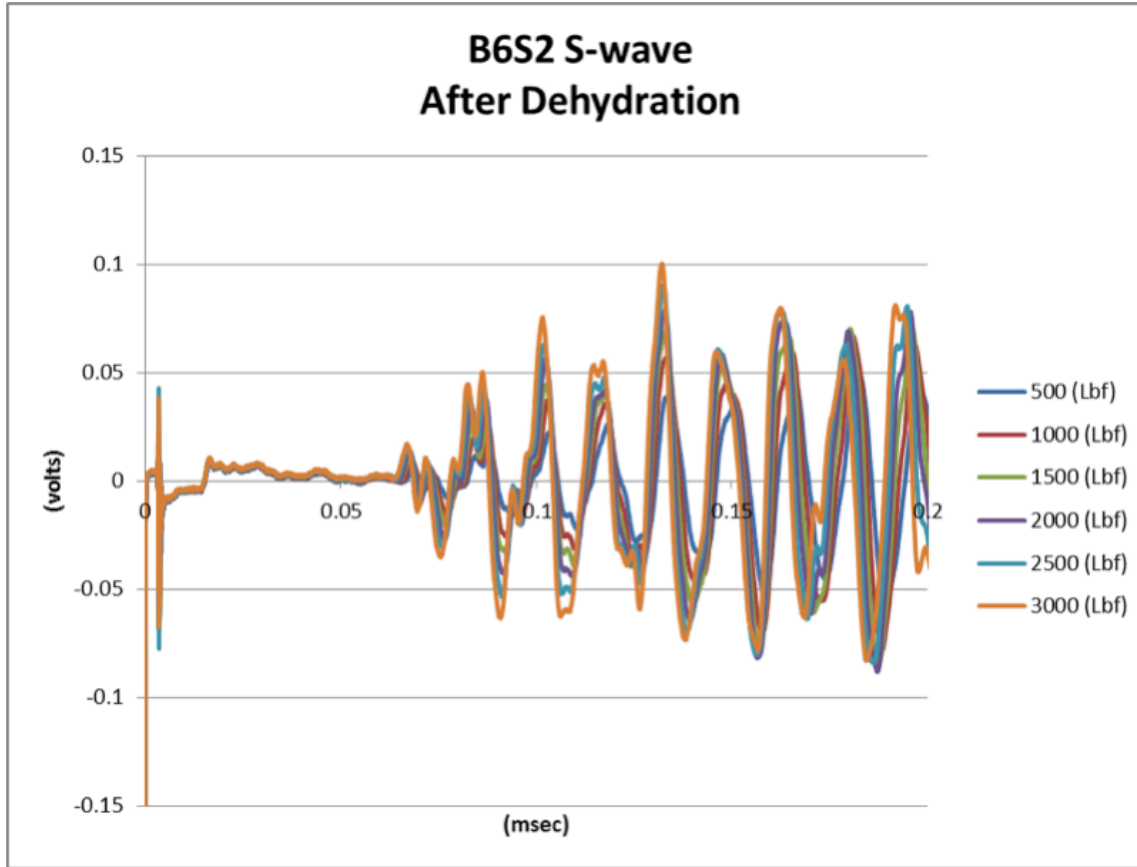
Graph of sample B6S2, P waveform from 500 Lbf to 3000 Lbf prior to sample dehydration.



Graph of sample B6S2, P waveform from 500 Lbf to 3000 Lbf after sample dehydration.



Graph of sample B6S2, S waveform from 500 Lbf to 3000 Lbf prior to sample dehydration.



Graph of sample B6S2, S wave from 500 Lbf to 3000 Lbf after sample dehydration.

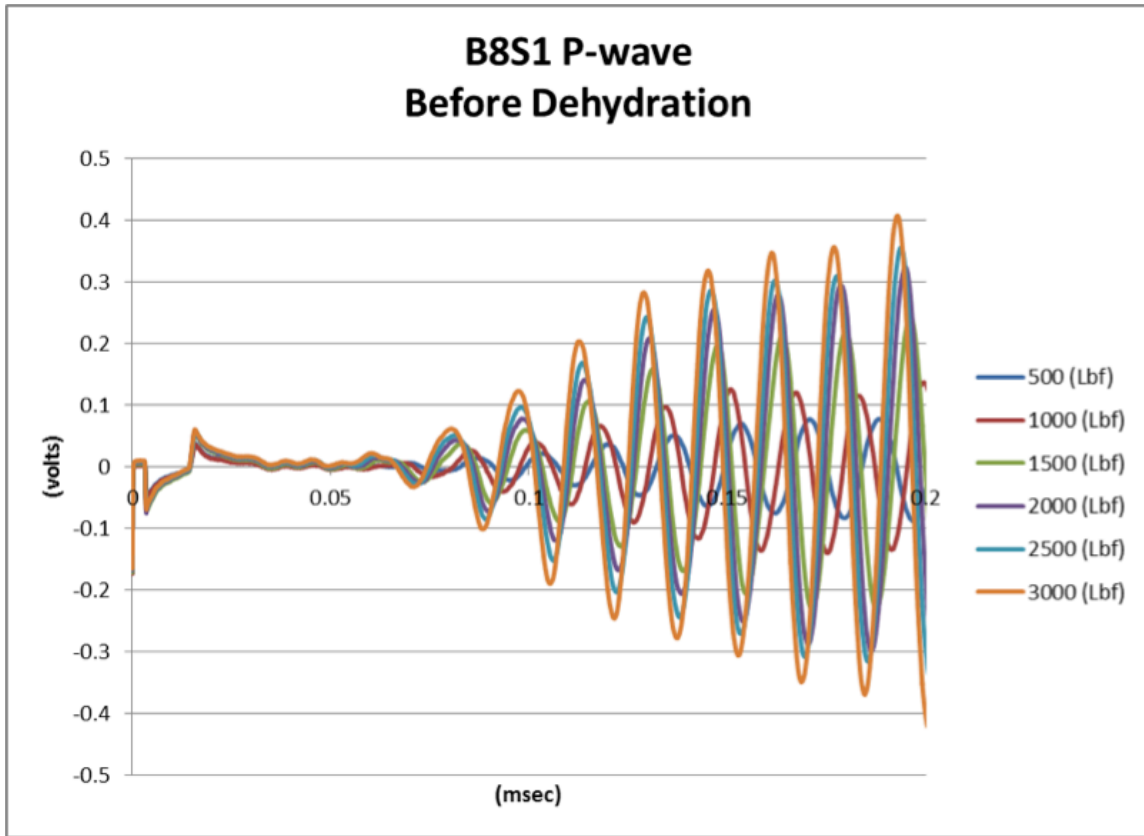
B6S2 Before Dehydration							
Lbf	P wave (m/s)	S wave (m/s)	Poisson's Ratio	Young's Modulus (kPa)	Bulk Modulus (kPa)	Shear Modulus (kPa)	
500	5125	1842	0.43	21601018	48525532	7575005	
1000	5225	1873	0.43	22329782	50498900	7827855	
1500	5350	1945	0.42	24052100	52631760	8446237	
2000	5165	1973	0.41	24592864	47962692	8692873	
2500	5123	1998	0.41	25132956	46702888	8910442	
3000	5129	2018	0.41	25590316	46461388	9086165	

Velocity of P- and S-waves and elastic moduli of sample B6S2 before dehydration.

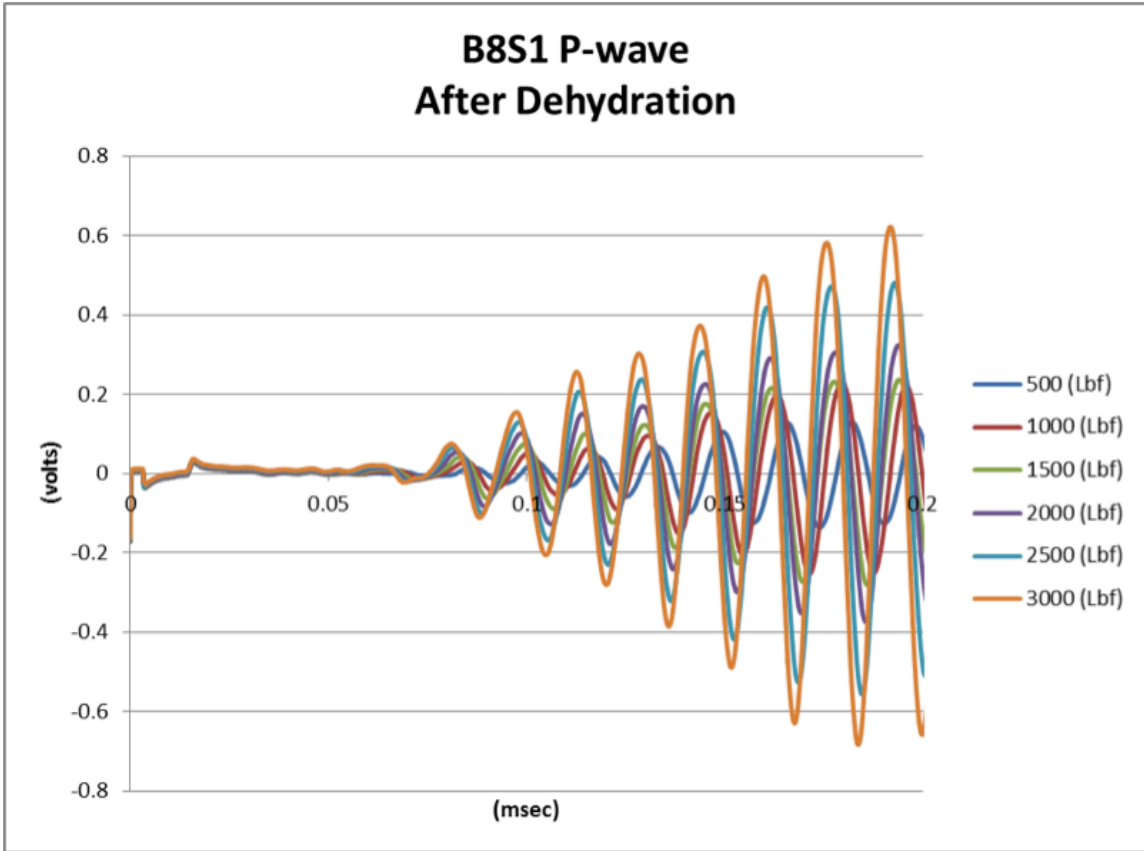
B6S2 After Dehydration							
Lbf	P wave (m/s)	S wave (m/s)	Poisson's Ratio	Young's Modulus (kPa)	Bulk Modulus (kPa)	Shear Modulus (kPa)	
500	5118	1930	0.42	23485096	47239928	8286075	
1000	5131	1950	0.42	23962914	47300812	8464078	
1500	5167	1964	0.42	24292630	47968644	8580357	
2000	5211	1971	0.42	24499208	48892212	8647885	
2500	5204	2003	0.41	25226388	48363648	8926112	
3000	5266	2034	0.41	26010644	49428088	9208647	

Velocity of P- and S-waves and elastic moduli of sample B6S2 after dehydration.

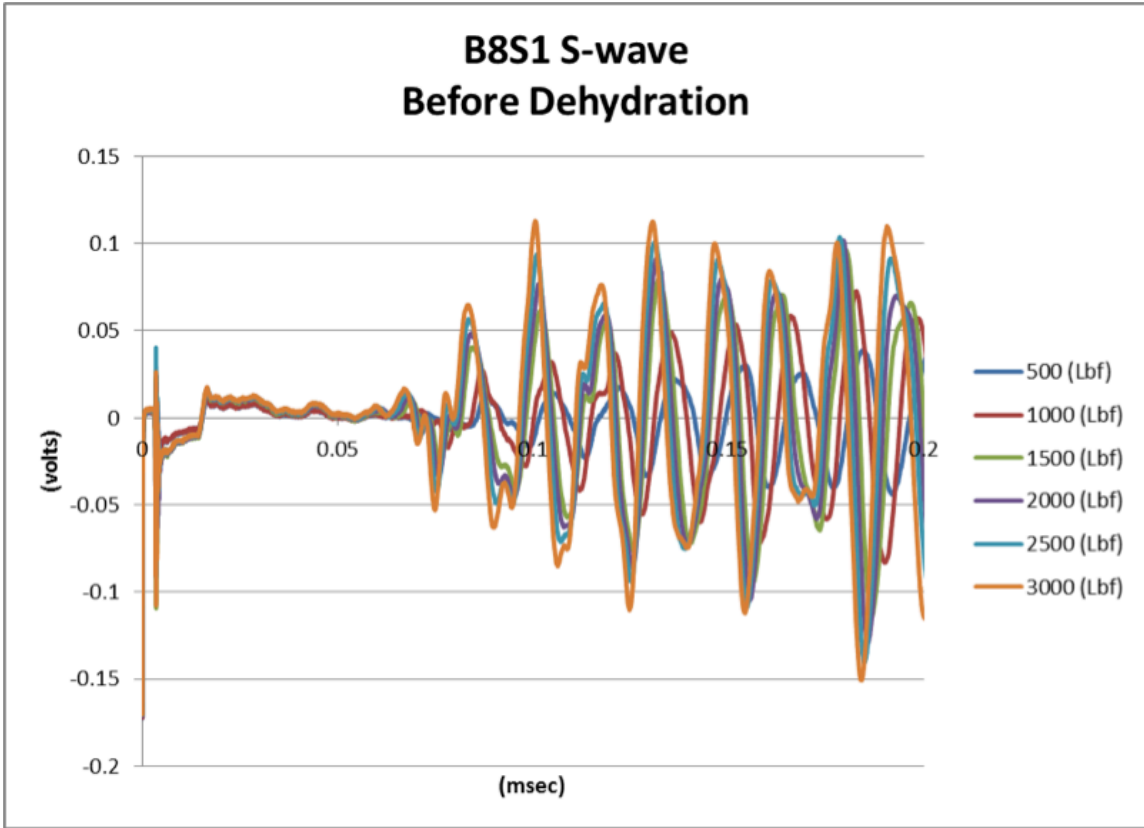
B8S1



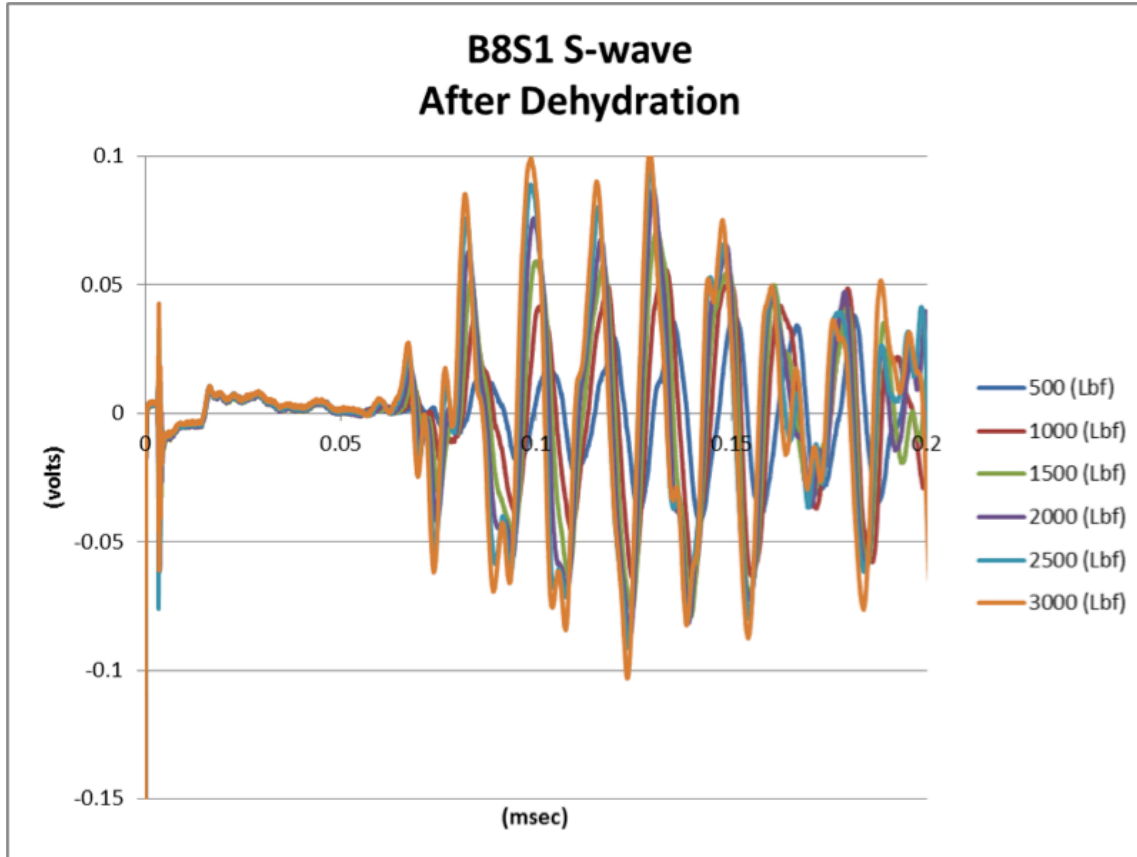
Graph of sample B8S1, P waveform from 500 Lbf to 3000 Lbf prior to sample dehydration.



Graph of sample B8S1, P waveform from 500 Lbf to 3000 Lbf after sample dehydration.



Graph of sample B8S1, S waveform from 500 Lbf to 3000 Lbf prior to sample dehydration.



Graph of sample B8S1, S waveform from 500 Lbf to 3000 Lbf after sample dehydration.

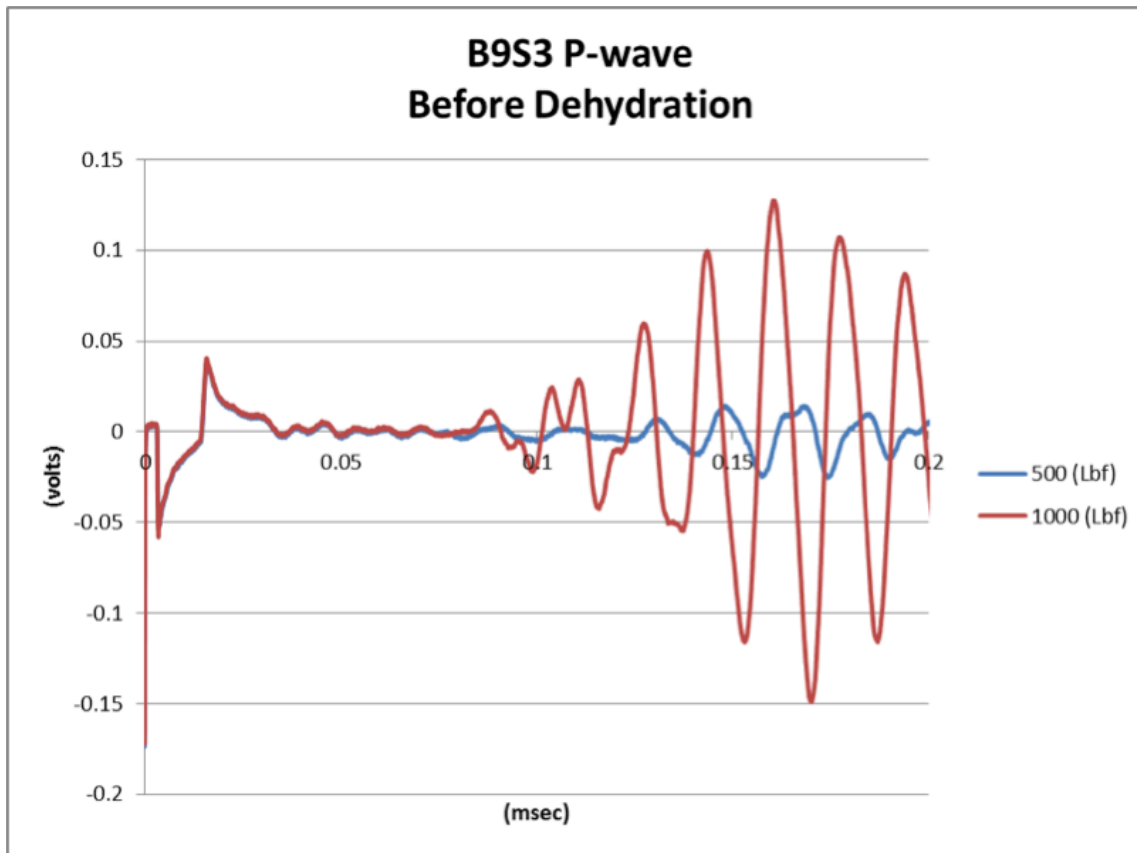
B8S1 Before Dehydration							
Lbf	P wave (m/s)	S wave (m/s)	Poisson's Ratio	Young's Modulus (kPa)	Bulk Modulus (kPa)	Shear Modulus (kPa)	
500	5359	1855	0.43	24043768	58839828	8395787	
1000	5391	1906	0.43	25322868	59062896	8863183	
1500	5395	2040	0.42	28763868	57436292	10152904	
2000	5337	2087	0.41	29794204	55387308	10562730	
2500	5398	2119	0.41	30863510	56453844	10953185	
3000	5398	2143	0.41	31511250	56129456	11202544	

Velocity of P- and S-waves and elastic moduli of sample B8S1 before dehydration.

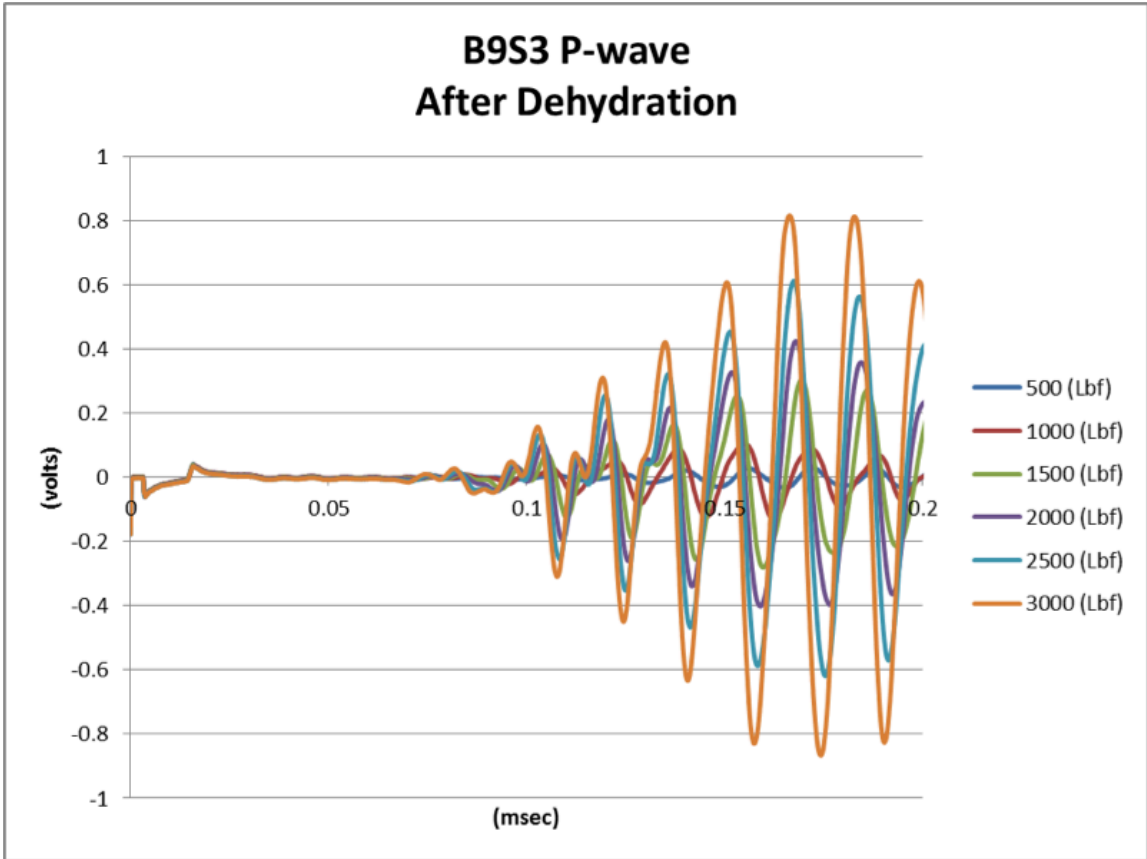
B8S1 After Dehydration							
Lbf	P wave (m/s)	S wave (m/s)	Poisson's Ratio	Young's Modulus (kPa)	Bulk Modulus (kPa)	Shear Modulus (kPa)	
500	5199	1978	0.42	26913214	52996648	9507539	
1000	5274	2033	0.41	28365524	54188820	10039067	
1500	5305	2081	0.41	29635898	54335276	10515928	
2000	5359	2109	0.41	30421484	55358844	10799929	
2500	5405	2143	0.41	31393570	56088276	11158478	
3000	5462	2162	0.41	31924594	56573848	11353389	

Velocity of P- and S-waves and elastic moduli of sample B8S1 after dehydration.

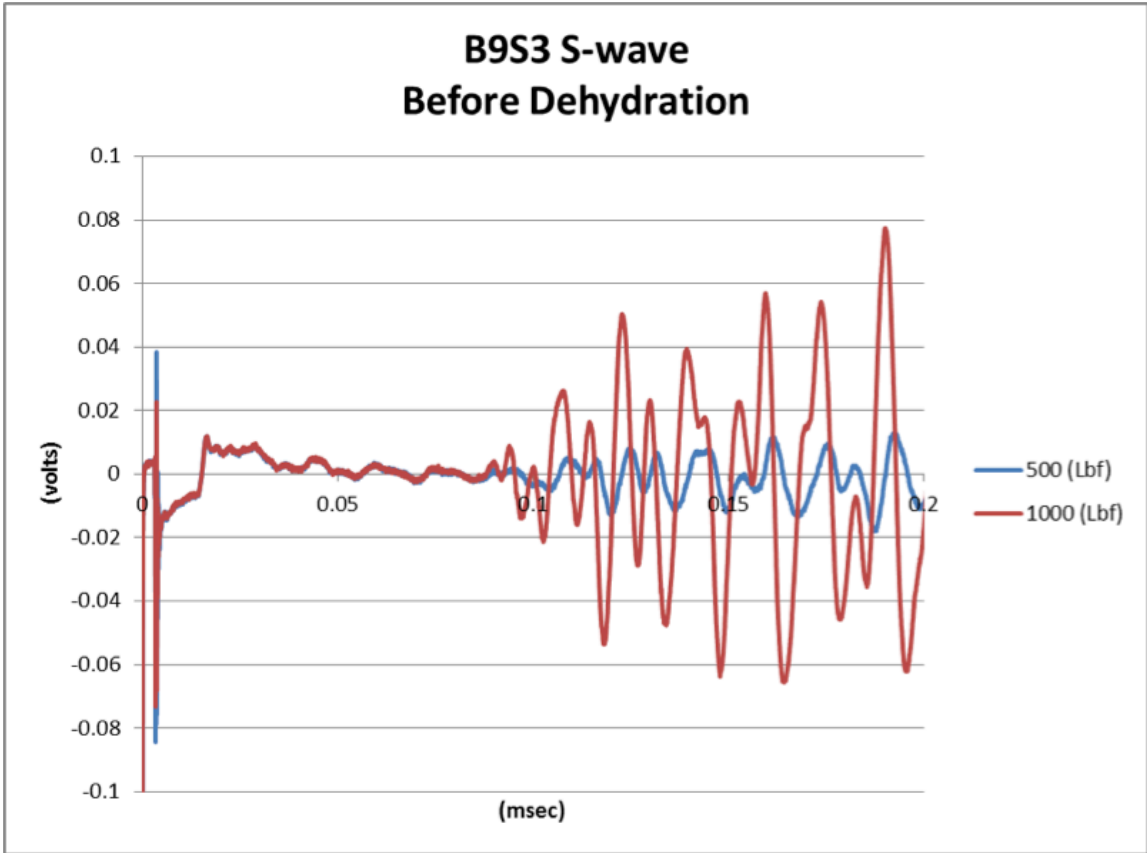
B9S3



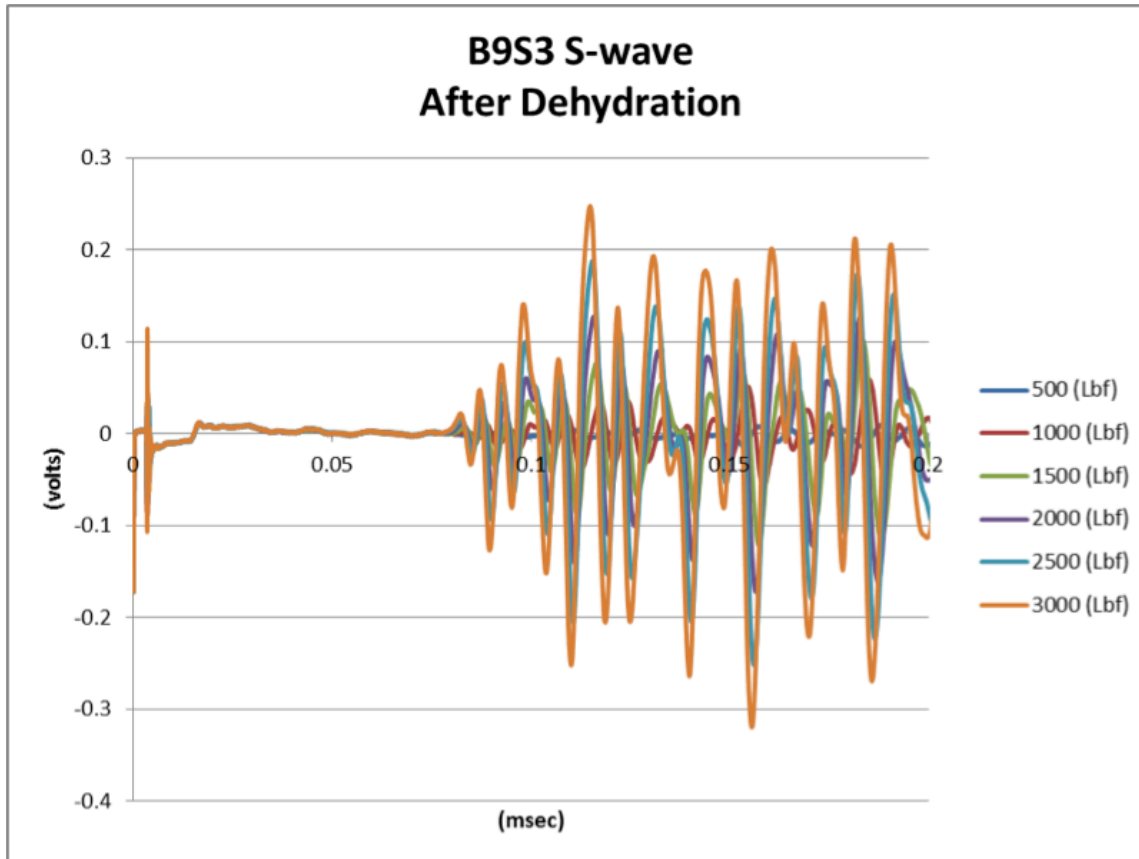
Graph of sample B9S3, P waveform from 500 Lbf to 1000 Lbf prior to sample dehydration.



Graph of sample B9S3, P waveform from 500 Lbf to 3000 Lbf after sample dehydration.



Graph of sample B9S3, S waveform from 500 Lbf to 1000 Lbf prior to sample dehydration.



Graph of sample B9S3, S waveform from 500 Lbf to 3000 Lbf after sample dehydration.

B9S3 Before Dehydration						
Lbf	P wave (m/s)	S wave (m/s)	Poisson's Ratio	Young's Modulus (kPa)	Bulk Modulus (kPa)	Shear Modulus (kPa)
500	5229	1298	0.47	11948077	60624760	4071858
1000	5305	1306	0.47	12091725	62474620	4119158

Velocity of P- and S-waves and elastic moduli of sample B9S3 before dehydration.

B9S3 After Dehydration						
Lbf	P wave (m/s)	S wave (m/s)	Poisson's Ratio	Young's Modulus (kPa)	Bulk Modulus (kPa)	Shear Modulus (kPa)
500	5280	1362	0.46	12859237	60122272	4390759
1000	5322	1423	0.46	14002470	60631668	4790414
1500	5356	1442	0.46	14372362	61320024	4918888
2000	5370	1451	0.46	14562924	61586056	4985290
2500	5405	1457	0.46	14672100	62436036	5021822
3000	5538	1461	0.46	14766237	65840488	5047868

Velocity of P- and S-waves and elastic moduli of sample B9S3 after dehydration.

Appendix C - Gassmann Modeling Data

Theoretical Modeling

Sub-critical CO₂ in Sandstone

Sandstone with Subcritical CO ₂				
15% Porosity				
CO ₂ Saturation	Vp	Density	I	K
0.05	843	1986	1674198	-5.39E+09
0.1	705	1979	1395195	-5.82E+09
0.15	650	1971	1281150	-5.97E+09
0.2	621	1964	1219644	-6.04E+09
0.25	604	1956	1181424	-6.09E+09
0.3	592	1949	1153808	-6.12E+09
0.35	583	1941	1131603	-6.14E+09
0.4	577	1934	1115918	-6.16E+09
0.45	572	1926	1101672	-6.17E+09
0.5	569	1918	1091342	-6.18E+09
0.55	566	1911	1081626	-6.19E+09
0.6	564	1903	1073292	-6.20E+09
0.65	562	1896	1065552	-6.20E+09
0.7	561	1888	1059168	-6.21E+09
0.75	560	1881	1053360	-6.21E+09
0.8	559	1873	1047007	-6.22E+09
0.85	559	1865	1042535	-6.22E+09
0.9	558	1858	1036764	-6.22E+09
0.95	558	1850	1032300	-6.22E+09
1	558	1843	1028394	-6.23E+09

Modeled P-wave velocity, density, impedance, and bulk modulus for various levels of sub-critical CO₂ saturations in sandstone at 15 percent porosity.

Sandstone with Subcritical CO2				
20% Porosity				
CO2 Saturation	Vp	Density	I	K
0.05	1763	1984	3497792	-6.40E+08
0.1	1731	1974		-8.92E+08
0.15	1722	1964		-9.80E+08
0.2	1720	1954		-1.02E+09
0.25	1721	1944		-1.05E+09
0.3	1723	1934		-1.06E+09
0.35	1725	1923		-1.08E+09
0.4	1779	1986		-1.09E+09
0.45	1732	1903		-1.09E+09
0.5	1735	1893		-1.10E+09
0.55	1739	1883		-1.10E+09
0.6	1743	1873		-1.11E+09
0.65	1748	1863		-1.11E+09
0.7	1752	1853		-1.12E+09
0.75	1756	1843		-1.12E+09
0.8	1761	1833		-1.12E+09
0.85	1765	1823		-1.12E+09
0.9	1770	1813		-1.12E+09
0.95	1775	1802		-1.13E+09
1	1779	1792		-1.13E+09

Modeled P-wave velocity, density, impedance, and bulk modulus for various levels of sub-critical CO₂ saturations in sandstone at 20 percent porosity.

Sandstone with Subcritical CO2				
25% Porosity				
CO2 Saturation	Vp	Density	I	K
0.05	2076	1981	4112556	1.73E+09
0.1	2061	1969	4058109	1.55E+09
0.15	2060	1956	4029360	1.49E+09
0.2	2063	1944	4010472	1.46E+09
0.25	2067	1931	3991377	1.44E+09
0.3	2072	1918	3974096	1.43E+09
0.35	2078	1906	3960668	1.42E+09
0.4	2084	1893	3945012	1.41E+09
0.45	2090	1881	3931290	1.41E+09
0.5	2097	1868	3917196	1.40E+09
0.55	2103	1855	3901065	1.40E+09
0.6	2110	1843	3888730	1.40E+09
0.65	2117	1830	3874110	1.39E+09
0.7	2124	1818	3861432	1.39E+09
0.75	2131	1805	3846455	1.39E+09
0.8	2139	1792	3833088	1.39E+09
0.85	2146	1780	3819880	1.39E+09
0.9	2154	1767	3806118	1.39E+09
0.95	2161	1755	3792555	1.38E+09
1	2169	1742	3778398	1.38E+09

Modeled P-wave velocity, density, impedance, and bulk modulus for various levels of sub-critical CO₂ saturations in sandstone at 25 percent porosity.

Sandstone with Subcritical CO2				
30% Porosity				
CO2 Saturation	Vp	Density	I	K
0.05	2243	1979	4438897	3.15E+09
0.1	2237	1964	4393468	3.01E+09
0.15	2240	1949	4365760	2.97E+09
0.2	2246	1934	4343764	2.94E+09
0.25	2253	1918	4321254	2.93E+09
0.3	2261	1903	4302683	2.92E+09
0.35	2269	1888	4283872	2.91E+09
0.4	2278	1873	4266694	2.91E+09
0.45	2287	1858	4249246	2.90E+09
0.5	2296	1843	4231528	2.90E+09
0.55	2305	1828	4213540	2.90E+09
0.6	2314	1813	4195282	2.89E+09
0.65	2324	1797	4176228	2.89E+09
0.7	2333	1782	4157406	2.89E+09
0.75	2343	1767	4140081	2.89E+09
0.8	2353	1752	4122456	2.89E+09
0.85	2363	1737	4104531	2.89E+09
0.9	2373	1722	4086306	2.89E+09
0.95	2384	1707	4069488	2.89E+09
1	2394	1692	4050648	2.89E+09

Modeled P-wave velocity, density, impedance, and bulk modulus for various levels of sub-critical CO₂ saturations in sandstone at 30 percent porosity.

Supercritical CO₂ in Sandstone

Sandstone with Supercritical CO ₂				
15% Porosity				
CO ₂ Saturation	Vp	Density	I	K
0.05	1135	1989	2.26E+06	-4.24E+09
0.1	903	1984	1.79E+06	-2.18E+09
0.15	802	1980	1.59E+06	-5.53E+09
0.2	744	1975	1.47E+06	-5.71E+09
0.25	707	1970	1.39E+06	-5.80E+09
0.3	680	1965	1.34E+06	-5.89E+09
0.35	661	1960	1.30E+06	-5.95E+09
0.4	646	1956	1.26E+06	-5.99E+09
0.45	634	1951	1.24E+06	-6.02E+09
0.5	625	1946	1.22E+06	-6.04E+09
0.55	617	1941	1.20E+06	-6.06E+09
0.6	610	1936	1.18E+06	-6.08E+09
0.65	605	1932	1.17E+06	-6.10E+09
0.7	600	1927	1.16E+06	-6.11E+09
0.75	596	1922	1.15E+06	-6.12E+09
0.8	592	1917	1.13E+06	-6.13E+00
0.85	589	1912	1.13E+06	-6.14E+09
0.9	587	1908	1.12E+06	-6.14E+09
0.95	585	1903	1.11E+06	-6.15E+09
1	583	1898	1.11E+06	-6.16E+09

Modeled P-wave velocity, density, impedance, and bulk modulus for various levels of supercritical CO₂ saturations in sandstone at 15 percent porosity.

Sandstone with Supercritical CO ₂					
20% Porosity					
CO ₂ Saturation	Vp	Density	I	K	
0.05	1857	1988	3.69E+06	-1.02E+07	
0.1	1782	1981	3.53E+06	-5.17E+08	
0.15	1755	1975	3.47E+06	-7.22E+08	
0.2	1743	1968	3.43E+06	-8.27E+08	
0.25	1736	1962	3.41E+06	-8.92E+08	
0.3	1733	1956	3.39E+06	-9.35E+08	
0.35	1731	1949	3.37E+06	-9.67E+08	
0.4	1730	1943	3.36E+06	-9.90E+08	
0.45	1730	1936	3.35E+06	-1.00E+09	
0.5	1731	1930	3.34E+06	-1.02E+09	
0.55	1732	1924	3.33E+06	-1.03E+09	
0.6	1733	1917	3.32E+06	-1.05E+09	
0.65	1735	1911	3.32E+06	-1.05E+09	
0.7	1737	1904	3.31E+06	-1.06E+09	
0.75	1739	1898	3.30E+06	-1.07E+09	
0.8	1741	1892	3.29E+06	-1.07E+09	
0.85	1743	1885	3.29E+06	-1.07E+09	
0.9	1745	1879	3.28E+06	-1.08E+09	
0.95	1748	1872	3.27E+06	-1.08E+09	
1	1750	1866	3.27E+06	-1.09E+09	

Modeled P-wave velocity, density, impedance, and bulk modulus for various levels of supercritical CO₂ saturations in sandstone at 20 percent porosity.

Sandstone with Supercritical CO ₂				
25% Porosity				
CO ₂ Saturation	Vp	Density	I	K
0.05	2131	1986	4.23E+06	2.21E+09
0.1	2088	1978	4.13E+06	1.81E+09
0.15	2075	1970	4.09E+06	1.67E+09
0.2	2070	1962	4.06E+06	1.60E+09
0.25	2069	1954	4.04E+06	1.55E+09
0.3	2069	1946	4.03E+06	1.52E+09
0.35	2071	1938	4.01E+06	1.50E+09
0.4	2073	1930	4.00E+06	1.48E+09
0.45	2076	1922	3.99E+06	1.47E+09
0.5	2079	1914	3.98E+06	1.46E+09
0.55	2082	1906	3.97E+06	1.45E+09
0.6	2085	1898	3.96E+06	1.44E+09
0.65	2089	1890	3.95E+06	1.44E+09
0.7	2093	1882	3.94E+06	1.43E+09
0.75	2097	1874	3.93E+06	1.43E+09
0.8	2101	1866	3.92E+06	1.42E+09
0.85	2105	1858	3.91E+06	1.42E+09
0.9	2109	1850	3.90E+06	1.42E+09
0.95	2113	1842	3.89E+06	1.41E+09
1	2117	1834	3.88E+06	1.41E+09

Modeled P-wave velocity, density, impedance, and bulk modulus for various levels of supercritical CO₂ saturations in sandstone at 25 percent porosity.

Sandstone with Supercritical CO ₂				
30% Porosity				
CO ₂ Saturation	Vp	Density	I	K
0.05	2282	1984	4.53E+06	3.52E+09
0.1	2253	1975	4.45E+06	3.21E+09
0.15	2246	1965	4.41E+06	3.10E+09
0.2	2245	1956	4.39E+06	3.05E+09
0.25	2247	1946	4.37E+06	3.01E+09
0.3	2250	1936	4.36E+06	2.99E+09
0.35	2253	1927	4.34E+06	2.97E+09
0.4	2258	1917	4.33E+06	2.96E+09
0.45	2262	1908	4.32E+06	2.95E+09
0.5	2267	1898	4.30E+06	2.94E+09
0.55	2272	1888	4.29E+06	2.94E+09
0.6	2277	1879	4.28E+06	2.93E+09
0.65	2282	1869	4.27E+06	2.93E+09
0.7	2288	1860	4.26E+06	2.92E+09
0.75	2293	1850	4.24E+06	2.92E+09
0.8	2299	1840	4.23E+06	2.92E+09
0.85	2305	1831	4.22E+06	2.91E+09
0.9	2310	1821	4.21E+06	2.91E+09
0.95	2316	1812	4.20E+06	2.91E+09
1	2322	1802	4.18E+06	2.91E+09

Modeled P-wave velocity, density, impedance, and bulk modulus for various levels of supercritical CO₂ saturations in sandstone at 30 percent porosity.

Sub-critical CO₂ in Limestone

Limestone with Sub-Critical CO ₂				
15% Porosity				
CO ₂ Saturation	V _p	Density	I	K
0.05	639	1986	1269054	-5.99E+09
0.1	456	1979	902424	-6.39E+09
0.15	372	1971	733212	-6.53E+09
0.2	321	1964	630444	-6.60E+09
0.25	286	1956	559416	-6.64E+09
0.3	260	1949	506740	-6.67E+09
0.35	240	1941	465840	-6.69E+09
0.4	223	1934	431282	-6.71E+09
0.45	209	1926	402534	-6.72E+09
0.5	197	1918	377846	-6.73E+09
0.55	187	1911	357357	-6.73E+09
0.6	178	1903	338734	-6.74E+09
0.65	170	1896	322320	-6.75E+09
0.7	163	1888	307744	-6.75E+09
0.75	156	1881	293436	-6.76E+09
0.8	151	1873	282823	-6.76E+09
0.85	145	1865	270425	-6.76E+09
0.9	140	1858	260120	-6.77E+09
0.95	135	1850	249750	-6.77E+09
1	131	1843	241433	-6.77E+09

Modeled P-wave velocity, density, impedance, and bulk modulus for various levels of sub-critical CO₂ saturations in limestone at 15 percent porosity.

Limestone with Sub-Critical CO ₂				
20% Porosity				
CO ₂ Saturation	Vp	Density	I	K
0.05	1644	1984	3261696	-1.44E+09
0.1	1608	1974	3174192	-1.70E+09
0.15	1598	1964	3138472	-1.79E+09
0.2	1595	1954	3116630	-1.83E+09
0.25	1595	1944	3100680	-1.86E+09
0.3	1596	1934	3086664	-1.88E+09
0.35	1598	1923	3072954	-1.89E+09
0.4	1601	1913	3062713	-1.90E+09
0.45	1604	1903	3052412	-1.91E+09
0.5	1607	1893	3042051	-1.91E+09
0.55	1611	1883	3033513	-1.92E+09
0.6	1614	1873	3023022	-1.92E+09
0.65	1618	1863	3014334	-1.92E+09
0.7	1622	1853	3005566	-1.93E+09
0.75	1626	1843	2996718	-1.93E+09
0.8	1630	1833	2987790	-1.94E+09
0.85	1634	1823	2978782	-1.93E+09
0.9	1638	1813	2969694	-1.94E+09
0.95	1643	1802	2960686	-1.94E+09
1	1647	1792	2951424	-1.94E+09

Modeled P-wave velocity, density, impedance, and bulk modulus for various levels of sub-critical CO₂ saturations in limestone at 20 percent porosity.

Limestone with Sub-Critical CO2				
25% Porosity				
CO2 Saturation	Vp	Density	I	K
0.05	1981	1981	3924361	9.66E+08
0.1	1963	1969	3865147	7.78E+08
0.15	1961	1956	3835716	7.14E+08
0.2	1963	1944	3816072	6.81E+08
0.25	1967	1931	3798277	6.61E+08
0.3	1971	1918	3780378	6.48E+08
0.35	1977	1906	3768162	6.39E+08
0.4	1982	1893	3751926	6.32E+08
0.45	1988	1881	3739428	6.26E+08
0.5	1994	1868	3724792	6.22E+08
0.55	2000	1855	3710000	6.18E+08
0.6	2007	1843	3698901	6.15E+08
0.65	2013	1830	3683790	6.13E+08
0.7	2020	1818	3672360	6.10E+08
0.75	2027	1805	3658735	6.08E+10
0.8	2034	1792	3644928	6.07E+08
0.85	2041	1780	3632980	6.05E+08
0.9	2048	1767	3618816	6.04E+08
0.95	2055	1755	3606525	6.03E+08
1	2062	1742	3592004	6.02E+08

Modeled P-wave velocity, density, impedance, and bulk modulus for various levels of sub-critical CO₂ saturations in limestone at 25 percent porosity.

Limestone with Sub-Critical CO ₂				
30% Porosity				
CO ₂ Saturation	Vp	Density	I	K
0.05	2164	1979	4282556	2.46E+09
0.1	2155	1964	4232420	2.31E+09
0.15	2157	1949	4203993	2.26E+09
0.2	2163	1934	4183242	2.23E+09
0.25	2169	1918	4160142	2.22E+09
0.3	2177	1903	4142831	2.21E+09
0.35	2184	1888	4123392	2.20E+09
0.4	2193	1873	4107489	2.19E+09
0.45	2201	1858	4089458	2.19E+09
0.5	2210	1843	4073030	2.19E+09
0.55	2218	1828	4054504	2.18E+09
0.6	2227	1813	4037551	2.18E+09
0.65	2236	1797	4018092	2.18E+09
0.7	2246	1782	4002372	2.18E+09
0.75	2255	1767	3984585	2.18E+09
0.8	2265	1752	3968280	2.17E+09
0.85	2274	1737	3949938	2.17E+09
0.9	2284	1722	3933048	2.17E+09
0.95	2294	1707	3915858	2.17E+09
1	2304	1692	3898368	2.17E+09

Modeled P-wave velocity, density, impedance, and bulk modulus for various levels of sub-critical CO₂ saturations in limestone at 30 percent porosity.

Supercritical CO₂ in Limestone

Limestone with Supercritical CO ₂			
15% Porosity			
CO ₂ Saturation	V _p	Density	K
0.05	978	1989	-4.90E+09
0.1	712	1984	-5.79E+09
0.15	587	1980	-6.12E+09
0.2	511	1975	-6.29E+09
0.25	458	1970	-6.39E+09
0.3	418	1965	-6.46E+09
0.35	387	1960	-6.51E+09
0.4	362	1956	-6.55E+09
0.45	341	1951	-6.57E+09
0.5	323	1946	-6.60E+09
0.55	308	1941	-6.62E+09
0.6	294	1936	-6.63E+09
0.65	283	1932	-6.65E+09
0.7	272	1927	-6.66E+09
0.75	262	1922	-6.67E+09
0.8	254	1917	-6.68E+09
0.85	246	1912	-6.69E+09
0.9	238	1908	-6.69E+09
0.95	232	1903	-6.70E+09
1	226	1898	-6.71E+09

Modeled P-wave velocity, density, and bulk modulus for various levels of supercritical CO₂ saturations in limestone at 15 percent porosity.

Limestone with Supercritical CO ₂			
20% Porosity			
CO ₂ Saturation	Vp	Density	K
0.05	1746	1988	-7.44E+08
0.1	1664	1981	-1.32E+09
0.15	1635	1975	-1.52E+09
0.2	1621	1968	-1.63E+09
0.25	1613	1962	-1.70E+09
0.3	1609	1956	-1.74E+09
0.35	1606	1949	-1.77E+09
0.4	1605	1943	-1.80E+09
0.45	1605	1936	-1.82E+09
0.5	1605	1930	-1.83E+09
0.55	1606	1924	-1.84E+09
0.6	1607	1917	-1.85E+09
0.65	1608	1911	-1.96E+09
0.7	1609	1904	-1.87E+09
0.75	1611	1898	-1.88E+09
0.8	1613	1892	-1.88E+09
0.85	1615	1885	-1.89E+09
0.9	1617	1879	-1.89E+09
0.95	1619	1872	-1.89E+09
1	1621	1866	-1.90E+09

Modeled P-wave velocity, density, and bulk modulus for various levels of supercritical CO₂ saturations in limestone at 20 percent porosity.

Limestone with Supercritical CO ₂			
25% Porosity			
CO ₂ Saturation	Vp	Density	K
0.05	2043	1986	1.48E+09
0.1	1994	1978	1.05E+09
0.15	1979	1970	9.05E+08
0.2	1972	1962	8.27E+08
0.25	1970	1954	7.79E+08
0.3	1970	1946	7.47E+08
0.35	1970	1938	7.23E+08
0.4	1973	1930	7.06E+08
0.45	1975	1922	6.92E+08
0.5	1978	1914	6.81E+08
0.55	1981	1906	6.72E+08
0.6	1984	1898	6.65E+08
0.65	1987	1890	6.59E+08
0.7	1991	1882	6.53E+08
0.75	1995	1874	6.48E+08
0.8	1998	1866	6.44E+08
0.85	2002	1858	6.41E+08
0.9	2006	1850	6.37E+08
0.95	2010	1842	6.35E+08
1	2014	1834	6.32E+08

Modeled P-wave velocity, density, and bulk modulus for various levels of supercritical CO₂ saturations in limestone at 25 percent porosity.

Limestone with Supercritical CO ₂			
30% Porosity			
CO ₂ Saturation	Vp	Density	K
0.05	2208	1984	2.86E+09
0.1	2175	1975	2.53E+09
0.15	2166	1965	2.41E+09
0.2	2164	1956	2.35E+09
0.25	2165	1946	2.31E+09
0.3	2167	1936	2.28E+09
0.35	2170	1927	2.27E+09
0.4	2174	1917	2.25E+09
0.45	2178	1908	2.24E+09
0.5	2183	1898	2.23E+09
0.55	2188	1888	2.23E+09
0.6	2192	1879	2.22E+09
0.65	2197	1869	2.21E+09
0.7	2203	1860	2.21E+09
0.75	2208	1850	2.21E+09
0.8	2213	1840	2.20E+09
0.85	2219	1831	2.20E+09
0.9	2224	1821	2.20E+09
0.95	2230	1812	2.20E+09
1	2235	1802	2.19E+09

Modeled P-wave velocity, density, and bulk modulus for various levels of supercritical CO₂ saturations in limestone at 30 percent porosity.

KGS Modeling

4-26

Shc (w)	Shc (CO2)	Vp (Sw2)	Vs (Sw2)	Rho (Sw2)	K (Sw2)	Poisson (Sw2)
0.83	0.17	4912	2914	2735	3.50E+10	0.228
0.75	0.25	4909	2915	2732	3.49E+10	0.228
0.7	0.3	4909	2916	2731	3.49E+10	0.227
0.65	0.35	4909	2917	2729	3.48E+10	0.227
0.6	0.4	4909	2918	2728	3.48E+10	0.227
0.55	0.45	4910	2918	2726	3.48E+10	0.227
0.5	0.5	4911	2919	2725	3.48E+10	0.227
0.45	0.55	4911	2920	2723	3.47E+10	0.227
0.4	0.6	4912	2921	2722	3.47E+10	0.227
0.35	0.65	4913	2922	2710	3.47E+10	0.227
0.3	0.7	4914	2922	2719	3.47E+10	0.226
0.25	0.75	4916	2923	2717	3.47E+10	0.226
0.2	0.8	4917	2924	2716	3.47E+10	0.226

Modeled P-wave velocity, S-wave velocity, density, bulk modulus, and Poisson's Ratio for various levels of CO₂ saturations for sample 4-26 at 7.1 percent porosity.

Shc (w)	Shc (CO2)	Vp (Sw2)	Vs (Sw2)	Rho (Sw2)	K (Sw2)	Poisson (Sw2)
0.83	0.17	4939	2915	2733	3.57E+10	0.233
0.75	0.25	4940	2917	2729	3.56E+10	0.232
0.7	0.3	4940	2918	2727	3.56E+10	0.232
0.65	0.35	4942	2919	2725	3.56E+10	0.232
0.6	0.4	4943	2920	2723	3.56E+10	0.232
0.55	0.45	4944	2921	2721	3.56E+10	0.232
0.5	0.5	4946	2922	2719	3.55E+10	0.232
0.45	0.55	4947	2924	2716	3.55E+10	0.232
0.4	0.6	4949	2925	2714	3.55E+10	0.232
0.35	0.65	4951	2926	2712	3.55E+10	0.232
0.3	0.7	4953	2927	2710	3.55E+10	0.232
0.25	0.75	4954	2928	2708	3.55E+10	0.232
0.2	0.8	4956	2929	2706	3.55E+10	0.232

Modeled P-wave velocity, S-wave velocity, density, bulk modulus, and Poisson's Ratio for various levels of CO₂ saturations for sample 4-26 at 10 percent porosity.

Shc	Shc (CO2)	Vp (Sw2)	Vs (Sw2)	Rho (Sw2)	K (Sw2)	Poisson (Sw2)
0.83	0.17	4951	2916	2731	3.60E+10	0.234
0.75	0.25	4952	2918	2727	3.59E+10	0.234
0.7	0.3	4953	2919	2725	3.59E+10	0.234
0.65	0.35	4955	2921	2722	3.59E+10	0.234
0.6	0.4	4957	2922	2719	3.59E+10	0.234
0.55	0.45	4959	2923	2717	3.59E+10	0.234
0.5	0.5	4961	2925	2714	3.58E+10	0.234
0.45	0.55	4963	2926	2712	3.58E+10	0.234
0.4	0.6	4965	2928	2709	3.58E+10	0.234
0.35	0.65	4967	2929	2706	3.58E+10	0.233
0.3	0.7	4969	2930	2704	3.58E+10	0.233
0.25	0.75	4972	2932	2701	3.58E+10	0.233
0.2	0.8	4974	2933	2699	3.58E+10	0.233

Modeled P-wave velocity, S-wave velocity, density, bulk modulus, and Poisson's Ratio for various levels of CO₂ saturations for sample 4-26 at 12 percent porosity.

14-4

Shc (w)	Shc (CO2)	Vp (Sw2)	Vs (Sw2)	Rho (Sw2)	K (Sw2)	Poisson (Sw2)
0.8	0.2	5195	2992	2774	4.17E+10	0.252
0.75	0.25	5196	2993	2772	4.17E+10	0.252
0.7	0.3	5197	2994	2770	4.17E+10	0.252
0.65	0.35	5199	2995	2769	4.17E+10	0.252
0.6	0.4	5200	2996	2767	4.17E+10	0.252
0.55	0.45	5201	2997	2765	4.17E+10	0.252
0.5	0.5	5203	2998	2764	4.17E+10	0.252
0.45	0.55	5204	2999	2762	4.17E+10	0.251
0.4	0.6	5206	3000	2761	4.17E+10	0.251
0.35	0.65	5207	3000	2759	4.16E+10	0.251
0.31	0.69	5208	3001	2758	4.17E+10	0.251
0.25	0.75	5210	3002	2756	4.17E+10	0.251
0.2	0.8	5211	3003	2754	4.17E+10	0.251

Modeled P-wave velocity, S-wave velocity, density, bulk modulus, and Poisson's Ratio for various levels of CO₂ saturations for sample 14-4 at 7.55 percent porosity.

Shc (w)	Shc (CO2)	Vp (Sw2)	Vs (Sw2)	Rho (Sw2)	K (Sw2)	Poisson (Sw2)
0.8	0.2	5202	2994	2771	4.19E+10	0.252
0.75	0.25	5204	2995	2769	4.19E+10	0.252
0.7	0.3	5206	2996	2767	4.19E+10	0.252
0.65	0.35	5207	2997	2765	4.19E+10	0.252
0.6	0.4	5209	2998	2763	4.19E+10	0.252
0.55	0.45	5211	2999	2761	4.19E+10	0.252
0.5	0.5	5213	3001	2759	4.19E+10	0.252
0.45	0.55	5215	3002	2756	4.19E+10	0.252
0.4	0.6	5217	3003	2754	4.19E+10	0.252
0.35	0.65	5219	3004	2752	4.18E+10	0.252
0.31	0.69	5221	3005	2750	4.18E+10	0.252
0.25	0.75	5223	3006	2748	4.18E+10	0.252
0.2	0.8	5225	3008	2746	4.18E+10	0.252

Modeled P-wave velocity, S-wave velocity, density, bulk modulus, and Poisson's Ratio for various levels of CO₂ saturations for sample 14-4 at 10 percent porosity.

Shc (w)	Shc (CO2)	Vp (Sw2)	Vs (Sw2)	Rho (Sw2)	K (Sw2)	Poisson (Sw2)
0.8	0.2	5206	2995	2770	4.20E+10	0.253
0.75	0.25	5208	2996	2767	4.20E+10	0.253
0.7	0.3	5211	2997	2765	4.19E+10	0.253
0.65	0.35	5213	2999	2762	4.19E+10	0.253
0.6	0.4	5215	3000	2759	4.19E+10	0.253
0.55	0.45	5217	3002	2757	4.19E+10	0.253
0.5	0.5	5220	3003	2754	4.19E+10	0.253
0.45	0.55	5222	3004	2752	4.19E+10	0.253
0.4	0.6	5225	3006	2749	4.19E+10	0.253
0.35	0.65	5227	3007	2746	4.19E+10	0.253
0.31	0.69	5229	3008	2744	4.19E+10	0.253
0.25	0.75	5232	3010	2741	4.19E+10	0.253
0.2	0.8	5234	3011	2739	4.19E+10	0.253

Modeled P-wave velocity, S-wave velocity, density, bulk modulus, and Poisson's Ratio for various levels of CO₂ saturations for sample 14-4 at 12 percent porosity.